DTU Space
Department of Astrophysics and Atmospheric Physics

Tracing the Interstellar Medium of Quiescent Galaxies across Cosmic Time with ALMA

Master Thesis

Tracing the Interstellar Medium of Quiescent Galaxies across Cosmic Time with ALMA

Master Thesis
June, 2021

By
David Blánquez Sesé

Cover photo: ESO, José Francisco Salgado
Published by: DTU, Department of Astrophysics and Atmospheric Physics, Elektrovej, Building 328, 2800 Kgs. Lyngby Denmark
https://www.space.dtu.dk/english

Approval

This thesis has been prepared over six months under the supervision of Georgios Magdis at the division for Astrophysics and Atmospheric Physics, DTU Space, at the Technical University of Denmark, DTU, in partial fulfilment for the degree Master of Science in Earth and Space Physics and Engineering.

It is assumed that the reader has a basic knowledge in the areas of astronomy and astrophysics.

David Blánquez Sesé - s195558

.....

Signature

.....

Date

Abstract

Gas plays a paramount role in the galactic life cycle and is one of the main drivers of galaxy evolution. While gas mass reservoirs (M_{gas}) of star forming galaxies (SFGs) are routinely measured out to the highest redshifts, this is a very challenging feat for high redshift quiescent galaxies (QGs). The limited existing attempts so far yield contradictory or inconclusive results regarding the gas fraction ($f_{gas} = M_{gas}/M_{star}$) of these systems and its evolution with time, primarily due to technical limitations or biased sample selections. To address this issue in this project we attempt to measure the f_{gas} for representative samples of massive ($M_{star} > 10^{10} M_{\odot}$), 1< z < 3 QGs. Our samples are selected in the GOODS-South field taking advantage of the existing ZFOURGE UV to mid-IR multi-wavelength catalogues and are complemented by the new GOODS-S ALMA 1.1 mm map that covers 72.42 arcmin^2 of the field. By selecting QGs based on their UVJ colours or their distance to the main sequence (MS), we measure the rest frame dust emission (or estimate the corresponding upper limits) in the the R-J tail of the populations through ALMA stacking and infer their f_{gas} using a range of techniques. We find that galaxies residing in the envelope below the MS ($1/5 < \delta\mathrm{MS} < 1/2$) have an average f_{gas} that ranges from 67.5% down to 30.9% (depending on the adopted method), while UVJ selected QGs have $f_{gas} < 18.8\%$. The inferred estimates comply with previously estimated f_{gas} and support the current understanding that quiescent galaxies have lower gas fractions than main sequence galaxies at their correspondent redshifts while at the same time suggesting higher f_{gas} in high-z QGs compared to those in the local universe. A more sophisticated stacking approach in the UV-plane is the next step forward aiming to boost the stacked signal and fully characterise the f_{gas} of high-z QGs and get a better insight into the quenching mechanisms in the early universe.

Acknowledgements

First and foremost I want to thank Georgios Magdis for his invaluable help and guidance throughout the entire project, for placing his trust in me as a student and opening a path for me to follow. I must also thank Iary Davidzon, who also was one of my first mentors and gave me the basic knowledge and tools without which I could not have done this project. Thanks to Luis Fontán, for supporting my academic career all these years.

I want to thank DTU and all the friends and companions I have found here, who, even if they might not know, have saved my life in different ways. Specially, thanks to those who stood by my side when I needed it the most.

Finally, I want to show my most sincere appreciation to my family, who have always been there to support me and help me through the most challenging endeavours. Thanks to Cris, Jorge, Miriam, my Mom and my Dad.

It matters not how strait the gate,
How charged with punishments the scroll,
I am the master of my fate:
I am the captain of my soul

(*Invictus* 13-16) by William Ernest Henley

Abbreviations

AGNi = Active Galactic Nuclei
CDFS = Chandra Deep Field South
CMB = Cosmic Microwave Background
DM = Dark Matter
GOODS = Great Observatories Origins Deep Survey
IR = Infrared
ISM = Interstellar Medium
ΛCDM = *Lambda*- Cold Dark Matter Model
MS = Main sequence
QG = Quiescent galaxy
SB = Starburst Galaxy
SED = Spectral Energy Distribution
SFE = Star Formation Efficiency
SFG = Star forming galaxy
SFH = Star Formation History
SFR = Star Formation Rate

Contents

Chapter 1

Introduction

Astronomical observations have always provoked awe and genuine curiosity to understand our surroundings and the properties of nature. One of the most transcendent picture that needs needs to be understood is the evolution of the universe as a whole as a way of learning our place in it. Our comprehension of the cosmos is built on the study and research performed by many past civilizations. Most of our time this knowledge has been limited to the visible part of the celestial vault, i.e stars, planets, satellites and their motion. It was not until the telescope was developed, that the window to a further and hidden universe was opened. From the XVIIIth century on, the concept of galaxy was spread and research over the last centuries has proven that the evolution of the entire universe is closely linked to the formation and evolution of galaxies.

Our knowledge of galaxies has evolved from a mere description such as a flat disk full of stars, similar to nebulae, to the profound and deep classification that currently is held. Not only that, but how different components and parameters interplay to command their evolution. In order to picture the evolution of galaxies across cosmic time one has to study galaxies at different distances. The fact that light travels at a definite speed allows to study our universe's past the further away we gaze into. Therefore, to study galaxies at an early epoque one must look out to further distances. Observing galaxies at different lookback times gives the opportunity to draw a timeline of their evolution and using them as tracers of the evolution of the universe, helps placing constraints on the current universe and galaxy evolution model, known as the Λ Cold Dark Matter Model ($\Lambda-$CDM). This model set ups the scenario under which different structure formation models have been developed.

Structures are formed from small density perturbations, given that these are larger than the Jeans length, λ_J. This parameter expresses the minimum length a massive structure can have if it must collapse under its own weight. Overdense regions smaller than λ_J, merely oscillate in density. The observed anisotropy in the Cosmic Microwave Background (CMB), which is a result of the initial Big Bang conditions and is identified as temperature gradients, which can trace these initial gravitational perturbations. These can be studied from two different models. The *adiabatic model* assumes a top down formation process in which galaxies form from the fragmentation and collapse of the initial gravitational perturbations. On the other hand, the *isothermal model* considers that galaxies are formed from hierarchical clustering of small perturbations, i.e. a bottom up formation that ends up with the birth of galaxies as they are currently known. Both models take into account cold dark matter. As of today, dark matter (DM) is an unidentified component that has only been observed by the gravitational effects it exerts on the baryonic part of the

universe. For instance, it provides the necessary mass density for large scale structures to behave the way the do and to predict the measured velocities of certain stars according to the radius to the galactic center [Ryden, 2006].

Some theories interpret that the formation of one or other class of galaxy depends on the rapidity of star formation during its initial collapse. Other propose that the largest elliptical galaxies can only be the result of galaxy mergers. The fact that galaxies with stellar masses above $10^{12} M_{\odot}$ are very rare is not covered by any known theory though. Radiative cooling suggests that an upper limit on the mass of galaxies must exist, thus implying that galaxy formation and evolution is not the result of gravitational physics alone. The current understanding of all these phenomena have led to the conclusion that galaxies evolve within DM halos, much bigger and massive than the galaxies themselves. DM halos exert a gravitational pull on the visible, baryonic matter of galaxies which is clustered once it becomes cool enough to condense.

To model and compute simulations that hypothesize theories like the one above, a large number of galaxies must be observed and studied. In order to do so, galaxies are mostly classified into groups, that ease their understanding.

1.1 Galaxy types & components

The baryonic matter of galaxies is composed mostly by stars and the interstellar medium (ISM). The most visible component are the stars, which are mostly unresolved. It is possible, though, to analyse their luminosities, their colour and spectra. Joining their spectrum to the one from the ISM results in the total emission spectrum of the galaxy. Galaxy classification has been based on the morphology and light profiles. According to morphological features, galaxies are classified as:

1. **Spiral galaxies**:
   They usually have thin disks with spiral arm structures. Within this category barred or non barred spirals can be found, depending on whether there is a bar shaped structure in its central part. Finally, they can be further classified depending on the light fraction of the central bulge, the degree at which the arms are resolved into stars and how close the arms are to the main body of the galaxy.

2. **Elliptical galaxies**:
   These objects have a large number of subtypes (E1, E2,..., E7) depending on the ratio between its semimajor and semiminor axes. As their name states, they have an elliptical shape and are often filled with old populations of stars.

3. **Lenticular galaxies**:
   This type has properties of both ellipticals and spirals. They have thin discs and a central bulge but do not show any spiral arms.

4. **Irregular galaxies**:
   This kind of galaxies lack any symmetry or feature that makes them identifiable under any of the other classes. They do not show any rotationally symmetric disc and their shapes can vary greatly.

The classification above is known as the Hubble sequence, and is schematically depicted in fig. 1.1 below.

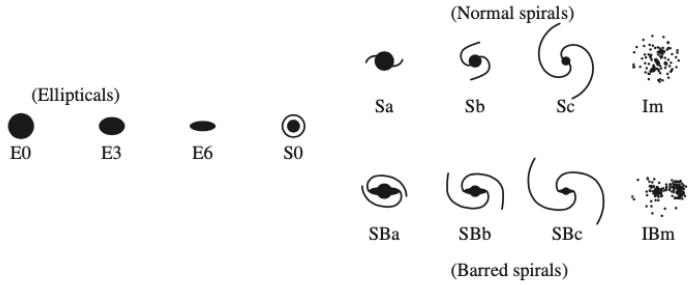

Figure 1.1: Schematic representation of different galaxy morphologies [Abraham, 1998].

Spiral galaxies

They are also identified as disk galaxies, containing a larger range of features than ellipticals, such as size and number of arms or central bulges. They usually consist on a thin gas disk with a barred or non barred central bulge, from which spiral arms grow outwards. It is in this arms where the younger population of stars, H_{II} regions and high concentrations of dust and molecular gas are found. Evidence exists that most disk galaxies are embedded in stellar halos that extend out to large radii [Mo et al., 2010]. Spiral galaxies often show an exponential brightness profile, which depends on the luminosity of the disk and the central bulge. Observations show that there is a trend in that bigger galaxies tend to be more luminous.

Figure 1.2: On the left is the spiral galaxy NGC5457. On the right is the barred spiral galaxy NGC7773 (Credits to NASA & ESA).

Their spectrum is typically prominent in the blue colors when comparing with similar luminosity elliptical galaxies. The reason behind this is that in the arms highly star forming regions are found, which emit as a blue continuum. At first sight, the central bulges were thought to be redder due to the inclination of the observed galaxies, which extinguished the light coming from the core. However, future observations proved that the color of the bulges actually matches the color of the inner part of the disk. Finally, the vertical structure of the disk has also been studied and it has been concluded that the luminosity distribution in that direction is independent to the distance to the galactic center.

Regarding their shape and form, half of the spirals have visible bars in their central bulges, as can be seen in fig. 1.2. More than half spiral galaxies show bar-like structures in their inner regions. Most spiral arms (usually there are 2) can be traced out to a wide range

of radii, and are closely linked to a bar structure in the inner part of the galaxy. Outside the arms the before mentioned stellar halos can be found. So far they have been observed in a small number of galaxies since their surface brightness is very low (our own and M31 f.e.). They are observed as stellar streams, which are composed of material stripped from other galaxies as a result of gravitational tidal forces [Helmi et al., 1999].

The gas content of spirals can be characterized with neutral and molecular hydrogen. Their gas mass fraction varies from 5 % in very massive galaxies up to 80 % in less massive ones. As it is expected, the metallicity content of the gas decreases as the studied radius increases. This is because the older population of stars is located in the central regions, whereas on the outer parts the younger stars are found. Most of the gas and stars within the galaxy move in circular orbit around the central bulge. Most interestingly, the Tully-Fischer relation [Tully et al., 1992] relies on the found correlation between the velocity at which a galaxy rotates (measured as far away as possible from the center) with its luminosity.

Elliptical galaxies
Elliptical galaxies are characterized by smooth, elliptical surface brightness distributions $I(R)$.They contain small quantities of gas and have redder colors, which usually come from old stellar populations. Their $I(R)$ is usually described as a function of the isophotal semimajor axis R [Mo et al., 2010], in turn this parameter is often characterized with average surface brightness within an effective radius I_e:

$$\langle I \rangle_e = \frac{L}{2\pi {R_e}^2}\,, \tag{1.1}$$

where L is the luminosity and R_e is the effective radius. The curves of equal brightness, i.e the isophotals, are shaped in ellipses, all of them sharing the same semimajor to semiminor axis ratio. Elliptical galaxies tend to have low angular velocities. These are calculated by comparing the maximum line-of-sight streaming motion v_m and $\bar{\Sigma}$ which is the average value of the line-of-sight velocity dispersion inside $R_e/2$. This method compares the total observed streaming velocity with the random motions happening within the galaxy, which gives a measure of the general rotational and travelling velocity of the source. At the center of most ellipticals the dispersion velocity drastically increases, maybe due to the effect of a super massive black hole on its nearby stellar populations. On the regions outside the center, contrarily, the dispersion velocity is observed to be constant or have very weak relation to position.

Figure 1.3: Image of Abell S0740 galaxy cluster with an elliptical galaxy in its center (Credits to: NASA & ESA)

As stated before, the characteristic red color of elliptical galaxies comes from old, metal-rich stellar populations. A correlation exists between the luminosity of the galaxy and its color, such that more luminous galaxies have redder colours [Peletier et al., 1990]. Their gas and dust content was thought to be low, however, it has been shown that they contain a considerable amount of both components. Not only that but the composition of the dust and gas also differs greatly from the one found in spiral galaxies. The ISM in elliptical galaxies can contribute up to $10^{10} M_{\odot}$ of the total system's mass [Mo et al., 2010], and emit strongly in the X-ray spectrum. It either is accreted from external sources or produced by the stellar populations within the galaxy. The total amount of dust and gas, does not affect the total luminosity of the galaxy, though.

1.1.1 Interstellar medium

The ISM can be considered the component that fills the space between stars in all galaxies. It consists on gas and dust particles that absorb the light from its surrounding stars and scatter it. The major distinction between the two is that their absorption properties have different wavelength dependencies.

Interstellar gas

Gas is an opaque medium principally in the extreme UV spectrum. It reprocesses the light it absorbs in the UV, optical and IR. Cool gas constitutes a crucial component in the formation of young stellar populations, and therefore it is abundant in star forming regions [Young and Scoville, 1991].

Interstellar dust

Dust is composed of graphitic carbon, silicate and hydrocarbon grains [Mathis et al., 1977; Leger and Puget, 1984]. The average interacting cross section is dominated by small size grains, whereas the largest contribution to the mass comes from the larger grains. Their size can be compared to that of the wavelength of blue light. which is why the reprocess that part of the spectrum more than the red one. Its opacity increases with wavelength and the following attenuation law can be used in order to model its light extinction:

$$\frac{I_{obs}}{I_{star}} = e^{a_\lambda - \Delta\tau} \tag{1.2}$$

Where a_λ is a wavelength-dependent reddening law and $\Delta\tau$ is the thickness of the ISM screen.

Technical limitations prevent from being able to observe the morphological characteristics of a galaxy, therefore using them as a classification method loses its meaning when

studying galaxies at great distances. The current methodology to study galaxies involves recording their spectral energy distribution (SED), which represents the galaxy emitted fluxes at different parts of the electromagnetic spectrum. The shape and magnitude of the SED shine light on most of the compelling properties: redshift, stellar mass (M_{star}), star formation rate (SFR), dust mass (M_{dust}), gas mass (M_{gas}), AGN activity and so on. Following this type of analysis, astronomers have found that galaxies can be divided in two types: star forming galaxies (SFGs) and quiescent galaxies (QGs) depending on the amount of star formation activity they hold. They are also generally known as late type galaxies and early type galaxies respectively.

These passively evolving quiescent galaxies have been observed at many cosmic epochs, both in photometric (Cimatti, 2003; Toft et al., 2005) and spectroscopic surveys (Gobat et al., 2012; Whitaker et al., 2013; Valentino et al., 2020). They are characterized by very low or nearly non-existent amounts of star formation activity and small amounts of dust. For this reason, their stellar populations are old and evolved with a redder spectrum. On the other side we have SFGs which have younger stellar populations, bright in the UV and bluer part of the spectrum.

1.2 Galaxy evolution

It has been observed that the SFR density peaked at z $\geq$ 1 . This means that star formation rates were on average higher in the past. Progressively, as we approach to the peak of the SFR density, so does the relative contribution of dust obscured SFG to the total measured SFR.

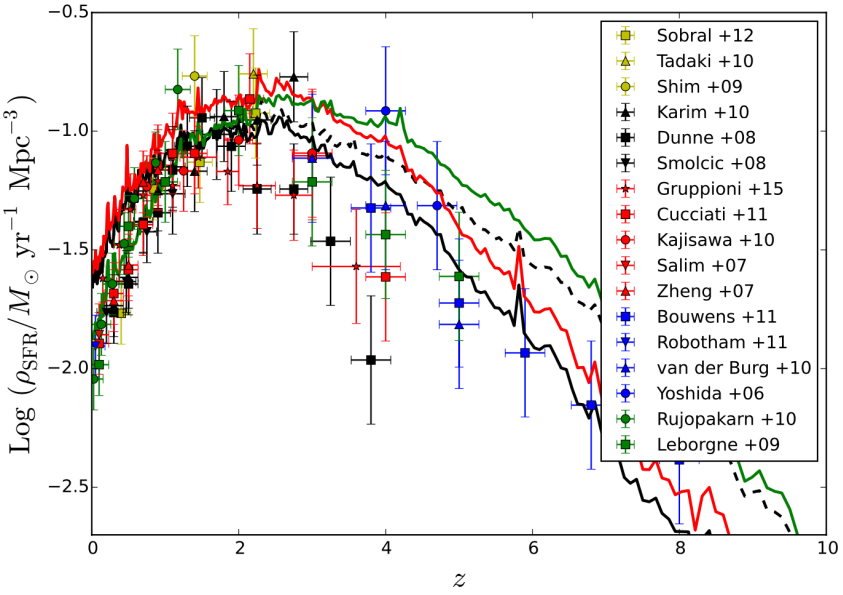

Figure 1.4: Evolution of the cosmic SFR density (ρ_{SFR}) across the Hubble time in GalICS 2.0 simulation code (curves) and a compilation of measured data points. More information at [Cattaneo et al., 2017].

The cosmic evolution of star formation and its subsequent stellar mass growth has been constrained up to z $\sim$ 5 [Liu et al., 2019]. The period at which ρ_{SFR} peaked is known as *cosmic noon*. Since then, it seems that the universe is slowly shutting down, with the average SFR density decreasing towards present times. This period of decreasing SFR is known as *cosmic dusk*. Finally the epoque beyond redshift z >2-3 is known as *cosmic dawn* and comprises the time when the first galaxies where formed and thus

galactic evolution started. Figure 1.4 poses a large number of unanswered questions. The most straightforward is why there is a maximum in ρ_{SFR} and why is it located at that specific redshift. There are arguments in favour of black holes depleting galaxies from the necessary gas to form stars, since their activity also peaked at a similar redshift [D.M., 2005]. Another observational challenge is the fact that galaxies are apparently not very efficient in forming stars. If they were, most of the mass of the universe would be observed in a baryonic form, when in fact it is not [Fukugita and Peebles, 2004].

1.2.1 Main sequence of star forming galaxies

The tight relation between a galaxy's stellar mass and its SFR has led to the definition of a main sequence (MS) of star forming galaxies. It has been observed that the SFR is partially governed by the amount of stellar mass, and their correlation has been proved from z $\sim$ 0 to z $\sim$ 4 (Elbaz et al., 2007; Schreiber et al., 2015). The spread of this narrow locus in the M_{star}-SFR plane has also been studied, being today accepted a 0.3 *dex* spread at all redshifts. The finding of this correlation was accompanied by the definition of an specific star formation rate (sSFR = SFR/M_{star}) at each redshift. It was observed that the MS was not consistent with random star formation bursts which are thought to be triggered by major galaxy mergers. These galaxies that lie above the MS locus are known as starburst galaxies or starbursts (SB). Following the discovery of the MS, other ways of identifying the main sequence have appeared. Another set of parameters used to identify it are the total L_{IR} ($L_{IR} = L_{8-1000\mu m}$) and L_8 which is the luminosity at rest frame 8μm. The ratio between them, $IR8 \equiv L_8/L_{IR}$ defines a second main sequence consistent with the one found in the M_{star}-SFR plane, where SB galaxies are also outliers. The fact that these parameters are correlated for galaxies at most redshifts means that a common IR SED must be shared and that its shape has not evolved greatly with cosmic time. Finally the last set of parameters with which the MS has been constrained are the molecular gas mass (M_{H2}) and SFR. The star formation efficiency of a galaxy (SFE $\equiv$ SFR/M_{H2}) is a parameter that measures ability of a galaxy to transform its gas reservoirs to stars. It was also found that SB systems have larger SFE than MS galaxies (Genzel et al., 2010).

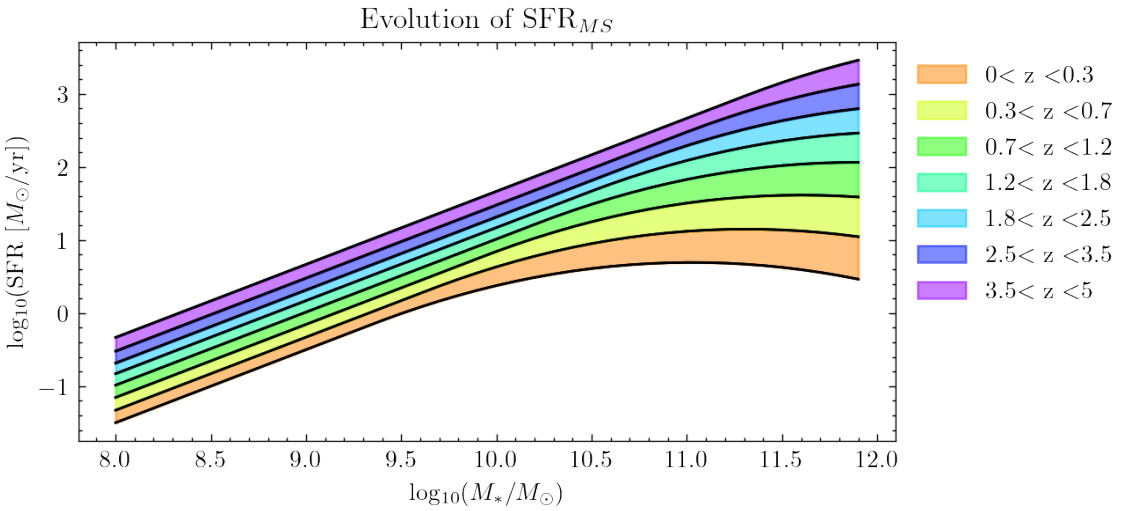

Figure 1.5: Evolution of (SFR$_{MS}$) with M_{star} at different redshift bins using [Schreiber et al., 2015] parametrization formula (eq. (1.5)).

Below the MS of galaxies another population of galaxies is found, quiescent galaxies (QGs). This means that for a determined stellar mass and redshift their SFR is lower than usual, leading to the hypothesis that they must have had their star formation stopped or diminished. The picture of galaxy evolution has been drawn starting from this initial dicotomy

of SFG vs QGs. The underlying reason for this is that so far the task of understanding galaxy evolution has been a matter of studying its star formation history and the parameters that affect it. Therefore, it is adamant to recognize that SFGs and QGs are not two completely different species, but different phases of the same entity. Understanding how galaxies form, grow and what different phases they go through is the puzzle that needs to be solved.

1.2.2 Quenching

The fact that star formation efficiency peaks at a determined halo mass, the observations that more massive galaxies have older stars and the misalignment between theoretical halo and observed stellar masses [Man and Belli, 2018] creates the need to introduce a mechanism that diminishes or turns off star formation, quenching. It is also a necessary phenomenon for the observable universe to be reproduced by the ΛCDM model. Quenching is understood either as:

- A process that completely stops star formation activity
- A process that is able to maintain a galaxy's quiescence for the rest of its lifetime.

The most important difference between these two is that they inherently must have different timescales. The physical phenomena responsible for them is still one of the most important voids in the story of galaxy formation. In order to present the different quenching models considered today, it must be considered how stars are formed in first place. Basically, stars form from cool gas at T $< 10^2$K, which has cooled down after being accreted as hot gas from cosmological filaments by the graviational pull of a galaxy's dark matter and baryonic mass.

Taking that into account, a quenching mechanism can act in different ways into that process to either halt it or terminate it. As compiled by [Man and Belli, 2018], a possible explanation for quenching could be "cosmological starvation" [Feldmann and Mayer, 2014], i.e. that the gas accretion on to the dark matter halo of the galaxy is diminished. However, this process alone may not terminate star formation completely, since the gas formed in stellar evolution could still produce young stellar populations. We also find arguments that are supported on the premise that if gas is not allowed to cool down, it will not be able to form stars. It is already known that virial shocks heat up the gas infalling to the galaxy [Rees and Ostriker, 1977]. It has also been simulated that this shocks appear above a certain halo mass, this being $M_{halo} > 10^{12} M_{\odot}$. The fact that galaxies seem to have an M_{star} limit of $10^{12} M_{\odot}$ supports the prevention of gas cooling as a quenching mechanism and the existence of virial shocks should be proved by the traces that it should leave circumgalactic medium. Long term quenching would still require an additional heating process though, for when the gas has already settled within the galaxy's halo, it should cool down and start forming stars. Some proposed heat sources are type Ia supernovae or the feedback of super massive black holes, being the latter the most commonly accepted.

It is also theorized that quenched galaxies are those which are not efficiently forming stars. It has already been learnt that galaxies do have different SFE, such as MS and SB galaxies. It is argued that a quenching mechanism could forestall the cool gas from losing kinetic energy and therefore make it unable to form stars. The sources responsible for this injection of kinetic energy range from stellar bulge produced turbulence to stellar bar formation, low power AGN feedback and magnetic fields. This phenomena is known as "morphological quenching" [Cornuault et al., 2018]. It was also found that this type of quenching is more effective at galaxies with low gas fractions ($f_{gas} = M_{gas}/M_{star} < 10\%$). Using the SFE as a starting point again, it could be argued that galaxies become quenched

because they consume their gas too rapidly. This is possible if the star formation activity occurs in a burst which can be triggered by compressive gas motions or angular momentum losses which facilitate aggregation of cool gas that form stars. These two phenomena are thought to be the after effects of galaxy mergers [Tabatabaei et al., 2018] or disk instabilities [Zolotov et al., 2015]. Finally along these lines the final possibility is that gas is dispelled from the galaxy. This removal could be powered by the accretion of matter towards a super massive black hole, which is able to liberate enough energy or momentum to displace the gas from a galaxy [Di Matteo et al., 2005]. The most common parameter that we observe in all quenching mechanism is gas, the fuel of star formation. Therefore a further study on the physical properties of the ISM, the physical conditions of gas at different phases and the intricacies of different feedback processes will shine light on what processes are behind the quiescence of galaxies and whether they have remained the same with cosmic time.

Identifying quiescent galaxies can be done either by photometric fluxes estimates (and subsequent colours), or by obtaining stellar populations parameters from SED fitting. Rest frame Colour-colour diagrams are used because they require less data processing and therefore introduce a smaller uncertainty in the final result. Among them we find the UVJ colour-colour diagram (eq. 1.3) [Labbé et al., 2005; Williams et al., 2009] and the $NUVrJ$ diagram (eq. 1.4) [Ilbert, O. et al., 2013]. Both of them rely on the delimitation of an area in the colour-colour space that encloses the quiescent population of galaxies. The UVJ has been widely used at different photometric surveys [Straatman et al., 2016; Skelton et al., 2014], for its biggest advantage is that it gets rid of the dust-age degeneracy. It is known that SFG are heavily obscured by dust, and that the most extremely star forming galaxies are those who are also greatly obscured by dust [Schreiber et al., 2015], such as luminous and ultraluminous IR galaxies. Dust obscuration affects the total emission and the SED of galaxies (see eq. (1.2)). It has been noted that age and dust obscuration affect the observed colours of a galaxy in a very similar way, therefore it is hard to discern whether a galaxy is very old and not dusty or heavily obscured and young. The UVJ selection method, circumvents this problem and is formulated as follows, applied at all redshifts:

$$QG = \begin{cases} U_{rest} - V_{rest} > 1.3 \\ V_{rest} - J_{rest} < 1.6 \\ U_{rest} - V_{rest} > 0.88 \times (V_{rest} - J_{rest}) + 0.49 \end{cases} \tag{1.3}$$

$$\begin{cases} M_{NUV} - M_r > 3(M_r - M_J) + 1, \\ M_{NUV} - M_r > 3. \end{cases} \tag{1.4}$$

The second method is based on comparing the SFR of a determined galaxy to the measured SFR of the MS (SFR_{MS}) at the redshift of the observed galaxy. To do so, models have been created to calculate the evolution of SFR_{MS} with cosmic time [Schreiber et al., 2015]:

$$log_{10}(SFR_{MS}\,[M_\odot/yr]) = m - m_0 + a_0 \cdot r - a_1[max(0, m - m_1 - a_2 \cdot r)]^2 \tag{1.5}$$

Where $m \equiv log_{10}(M_{star})/10^9 M_\odot$, $r \equiv log_{10}(1+z)$ and $m_0 = 0.5 \pm 0.07$, $m_1 = 0.36 \pm 0.3$, $a_0 = 1.5 \pm 0.15$, $a_1 = 0.3 \pm 0.08$, $a_2 = 2.5 \pm 0.06$. The SFR_{MS} thus depends on the redshift and M_{star}.

Using the SFR_{MS} allows identify the galaxy type (quiescent, star forming or starburst) according to its distance to the main sequence which is defined as $\Delta SFR = \mathrm{SFR}/\mathrm{SFR}_{MS}$. This approach though, can become vague depending on the selection criteria, since the journey from star forming to quiescence is not immediate. When a galaxy is being

quenched it will traverse from the SFR_{MS} locus to the lower SFR values. Therefore a selection that comprises SFR values close to the MS might englobe star forming sources with inherently low SFR, and transient galaxies that are becoming quenched.

Studies have been carried out in order to understand the effects of quenching on the observable properties of galaxies (colours and stellar population parameters). Some of them studying the star formation history (SFH) of galaxies [Belli et al., 2019], which is done by fitting galaxy models to the observed SED. Doing this for QGs has two main drawbacks: first is that old stellar populations do not evolve greatly, therefore time differences among them are hard to observe. The second is the degeneracy between mass formation history and mass assembly history. It represents how it is difficult to know whether the total stellar mass of a system has been formed within it or if a galaxy merger brought all the observed mass together. Studying the SFH, the relative contribution of stellar populations of different age to the total emission is found. This approach has shone light on two different quenching "paths" that galaxies follow. Thanks to the correlation between median age and rest frame colors found in the UVJ diagram. In Figure 1.6, we can observe the diagonal line with which the quiescent galaxies are differentiated, such that all sources above the diagonal are considered quiescent. This is a modified UVJ quiescent selection from the one showed before (eq. (1.3)), this is due to the fact that the original constraints (which can be seen as dashed lines in Figure 1.6), leave out dusty QGs misinterpreted as SFGs. It is then found that the median age of galaxies increases as one travels upward to the right in the direction marked by the diagonal. This trend, together with ability of the diagram to locate quiescent galaxies has allowed to differentiate between young and old quiescent populations, and led to two different quenching types: fast and slow quenching.

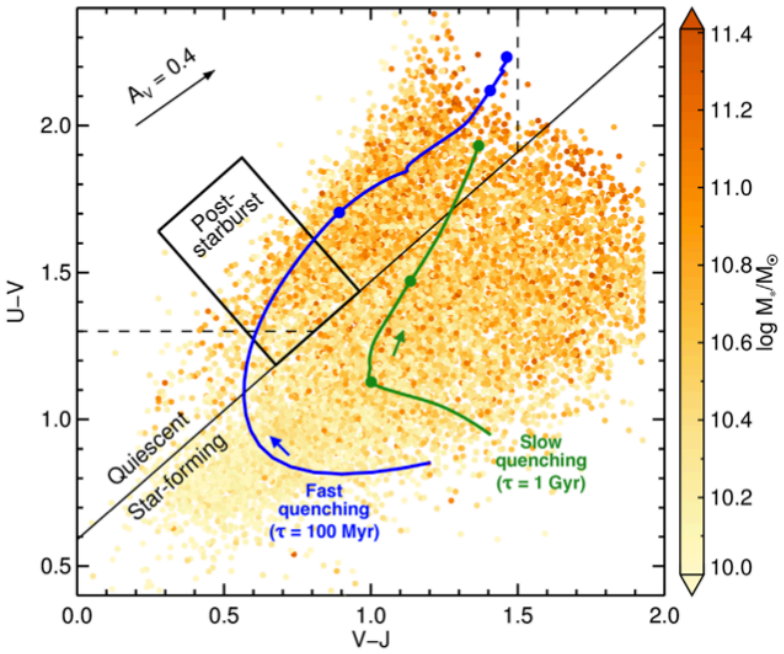

Figure 1.6: UVJ diagram showing the different quenching paths described by Belli et al., 2019. We find all galaxies in the UltraVISTA catalog with 1.5 < z < 2 and $M_{star} > 10^{10} M_\odot$ color coded according to their $log_{10}(M_{star}/M_\odot)$. The black diagonal line represents the modified UVJ quiescent selection criterion used by [Belli et al., 2019]. The original criterion [Williams et al., 2009] corresponds to the dashed lines. Finally the blue and green curves show a representative example of fast and slow quenching paths, with the post-starburst region limited by the black rectangle.

Young quiescent sources are considered *post-starburst galaxies* for they are observed shortly after their main star forming epoque. They are found at a constant number at all cosmic times. Their relevance to the total quiescent population, though, decreases at lower redshifts. At z $\sim$ 2.5 they conform 34 % of all quiescent galaxies, value that decreases to a mere 4% at z $\sim$ 1. It is estimated that crossing the post starburst region (depicted with a black box in Figure 1.6) takes 500 Myr. However, the fact that the number density of post-starburst galaxies decreases with redshift means that there must be another quenching path for galaxies, that takes at least more than 1 Gyr, this is, that they cross to the quiescent area of the UVJ diagram without crossing the post-starburst region. Galaxies that are considered post-starburst must have suffered a sudden termination of their star formation, whereas most massive galaxies are a product of slow quenching, which allowed to build up old stellar populations without being fully quenched.

The nominal paths that each of these two different quenching types follow are also shown in Figure 1.6. In those, each circular dot represents a time difference of 1 Gyr. The position at which a galaxy crosses the quiescent limiting diagonal will depend on the dust attenuation and quenching timescale [Belli et al., 2019]. The physical mechanisms proposed for fast quenching a compaction phenomenon that is able to trigger a starburst phase that ultimately leads to gas exhaustion. Concerning slow quenching, the proposed mechanism is a different one. SFGs have typical depletion timescales of 1 Gyr, therefore in order to maintain a continuous formation of stars a steady replenishment of gas is required. Should this replenishment be stopped, then the galaxy will consume its resting gas mass and quench over a larger time than the post starburst galaxies. The halting of gas inflow into a galaxy, which is a main gas replenishment process is known as mass starvation. Which can happen either if gas is not able to gas not being able to cool down due to large halo masses or if AGNi heat the existing cool gas. A signature of these processes is that the stellar metallicities of QGs are higher than those of SFG [Belli et al., 2019], since the available cool gas is that which has been injected by stellar evolution.

1.2.3 Gas study methods

A very popular technique to study the ISM of QGs is that of stacking [Schreiber et al., 2015; Tomczak et al., 2016; Gobat et al., 2018; Magdis et al., 2021], which extends the reach of a telescope by allowing the statistical acquisition of new data. Far IR and radio images rarely reach the near IR attained imaging depths, therefore the use of stack data has increased in order to account for that imbalance. The procedure is based on creating, for a determined image, individual cutouts or image tiles of a number of galaxies. Then by calculating the mean/median of the sum of all stacked images the rms decays proportionally as $\sigma_{img} \propto \sqrt{N}$, where N is the number of stacked cutouts, i.e galaxies. Median stacking represents the bulk of stacked sources with more fidelity, however it decreases the possibility of outliers detection. In addition to that, the handling of median statistic data is more challenging than that of mean stacking. The use of stacking for the study of a particular group of galaxies can be a double edged tool though. The decreasing of the rms of the stacked image comes at the cost of combining the fluxes of multiple galaxies, it is therefore critical that the stacked sources are similar or belong to the same class. This can be of extreme importance when studying the ISM of QGs for instance, whose emission is intrinsically dim, and therefore the flux of a few SFG can bias the final image. The study of individual sources also poses a number of inconveniences, such as the introducing of selection effects, i.e. the fact that the study of an individual source cannot be representative of the entire population. Some of the results in Figure 1.7 and 1.8 were obtained by stacking FIR images, for example. The deepest images in the FIR regimes have so far been taken by the Spitzer Space Telescope and the Herschel Space

Observatory which cover measurements at 24, 100 and 160 μm. This range can accurately probe the peak of the FIR SED. However, precise M_{dust} estimations require of a second data point in order to constrain the R-J tail. The importance of rest frame submillimiter data ($\lambda_{rest} \geq 250\mu$m) then arises, since its addition can greatly reduce the uncertainties on the diffuse ISM emission.

The importance of a reliable estimation of the dust mass comes from the selected method of calculating the gas fraction, which is through a gas to dust mass relation. In order to derive gas masses a variety of techniques have been discovered. Due to the fact that cool gas has a very faint emission, its estimation usually depends on correlating its abundance with another measurable component, i.e. gas tracers. The most popular are carbon monoxide CO [Carilli and Walter, 2013], CI [Puglisi et al., 2019; Bourne et al., 2019], and dust continuum emissions [Magdis et al., 2012; Gobat et al., 2018; Magdis et al., 2021]. The CI method is based on observing the neutral atomic carbon lines. It offers a number of advantages compared to the dust continuum and CO methods. First is that its emission lines, [CI](1-0) and [CI](2-1) emit a higher energy than CO(1-0) [Jiao et al., 2017]. That makes them a better tracer of gas at higher redshifts, since CO is only able to trace warm dense sections of H_2. It has also been observed that cosmic rays are able to break down CO molecules leaving a rich C phase. This, together with the fact that CI is an optically thin medium makes CI a powerful tracer of cool gas. This method has yet to be calibrated and more tightly constrained at lower redshifts before implementing it in higher redshift surveys. Unluckily, the observation of CI in the local universe has proven a difficult task, due to the weak atmospheric transmissions at the frequencies of the CI emission lines.

The CO conversion has been more extensively calibrated and used at both low and high redshift surveys. It is based on the following relation:

$$M_{gas} = \alpha_{CO} \cdot L'_{CO} \tag{1.6}$$

Where α_{CO} is the CO-H_2 conversion factor and L'$_{CO}$ is the luminosity of the observed CO emission line. Gas studies of quiescent galaxies have relied on the gas to dust relation method which uses another conversion factor, δ_{GDR}, which is again dependant on the gas-phase metallicity:

$$M_{gas} = M_{dust} \times \delta_{GDR} \tag{1.7}$$

Metallicity is usually obtained through the fundamental metallicity relation, which allows to infer it from the SFR and M_{star} of a galaxy. However this relation has only been constrained up to z $\sim$ 2 and it is not confirmed whether the relation holds above it or if a broken relation is needed. In addition to that another caveat is that at higher redshifts the contrast between the CMB and the dust continuum emission lines diminishes, which makes their observation more challenging as the lookback time increases. The majority of high redshift gas studies have used the δ_{GDR} conversion, because the observation of CO lines require accurate spectroscopic redshifts, making it a more expensive method concerning observation time and therefore impractical to obtain measurements of large populations. It must be noted that gas estimations performed with CO lines and dust continuum emissions have been compared, and both methods give similar results [Magdis et al., 2017; Magdis et al., 2012]. The challenge of using the dust gas technique resides in that it requires a detailed far IR SED, including the R-J tail. As it has already been mentioned, constraining the FIR SED at high redshifts poses many difficulties. Many of them come from the limited angular resolution that Herschel offers in the 100 and 160 μm bands, which goes down to 5 arcseconds. When adventuring into the high redshift universe, such resolutions usually lead to blending of sources and create the need to introduce further corrections in order to differentiate between target galaxy and possible satellites. If the

FIR SED is known, the M_{dust} can be derived by assuming that the SED is represented by a single temperature modified black body (MBB):

$$M_{dust} = \frac{S_\nu \, {D^2}_L}{(1+z)\kappa_{rest} \, B_\nu(\lambda_{rest}, T_d)} \quad \text{with} \quad \kappa_{rest} = \kappa_0 \left(\frac{\lambda_0}{\lambda_{rest}} \right)^\beta \tag{1.8}$$

where S_ν is the flux density, D_L the luminosity distance, κ_{rest} is the rest frame dust mass absorption coefficient at the observed wavelength and β is the dust emissivity. This approach does not take into account the size of the dust grains and that the actual FIR SED of galaxies is actually composed of dust components with different temperatures. Most of the dust emission at short wavelengths comes from the warmer component, however, it only accounts for 10% of its mass. The R-J tail is the SED part that if constrained, allows for a better estimation of the dust's temperature T_d and therefore more accurate M_{dust}. Another assumption that this method makes is that in high redshifts galaxies, gas is mostly found in a molecular state ($M_{H_2} \gg M_{H_I}$), and therefore the measured gas represents the actual cool gas that galaxies use to form stars. The dust-mass weighted luminosity L_{IR}/M_{dust}, dust temperature T_d and mean radiation field $\langle U \rangle$ are closely related parameters and their relation can be described with:

$$\langle U \rangle \propto \frac{L_{IR}}{M_{dust}} \propto T_d^{4+\beta} \tag{1.9}$$

The derivation of this parameters require a precise SED FIR peak and R-J tail estimation, which imply deep, FIR data highly difficult to obtain for quiescent high redshift galaxies.

1.3 Gas history

The ISM has been well documented and studied in SFG across cosmic times [Dekel et al., 2009; Magdis et al., 2012; Popping et al., 2014; Narayanan et al., 2015]. It has, together with the M_{star}-SFR relation and the $IR8$ ratio, been able to describe the MS of galaxies. It has also been found, concerning gas, that there must be two regimes for star formation, a long lasting mode (which is represented by the locus of MS galaxies) and a limited starburst mode. These two rely on the amount of gas (H_2), which was poorly determined before the number of gas studies increased not so long ago. The ISM has been studied by exploring the far IR (FIR) properties of galaxies SED, which hold information on the dust continuum emission, and other gas tracers. It has been observed that the dust and gas mass fraction have greatly declined since z $\approx$ 2. SFGs at that redshift had 10 times more ISM mass, and therefore fuel for star formation than local SFGs [Liu et al., 2019]. The population of SFGs at higher redshifts is characterized by higher SFR, shorter depletion times (τ_{dep}) and a higher SFE. Finally it was also observed that the temperature of dust in galaxies increases with redshift, following the increase observed in star formation and the intensity of the radiation field [Magdis et al., 2012]. The conclusions reached by many studies were that the variation in the gas fraction might be a consequence of the observed spread in the MS. In addition to that, the shape of the IR SED of MS galaxies seemed to be uniform, thus opening a window to place constraints on their gas content through dust and metallicity estimates. There has not been a similar study of gas in quiescent galaxies though, their gas mass is poorly constrained across cosmic time and its uncertainties as of today are large.

A question that must be answered is whether QGs have considerable amounts of unused gas. If it is so, it means that galaxy are not quenched because they run out of it. Quiescent galaxies have been observed up to redshifts z $\sim$ 3,4 [Gobat et al., 2018]. This means that at a time as early as 2 Gyr after the Big Bang, the processes that quenched galaxies

were already leaving its footprint. There have also been observations that the number of low mass galaxies ($M_{star} < 10^{10} M_{\odot}$) has increased enormously from z $\approx$ 2 to z $\approx$ 0.1, comparing it to the growth of SFGs. At $M_{star} > 10^{10} M_{\odot}$, the number of QGs grows by a factor of 6 (from z = 2 to z = 0.1) and this factor becomes $\approx$ 15-30 at masses lower than $M_{star} = 10^{10} M_{\odot}$. The small growth observed in the star forming populations, which only grow by a factor of 2 [Tomczak et al., 2014], linger in comparison. Observing quiescent galaxies at high redshift is a very powerful tool when constraining the physical processes that quench galaxies, since they place an age limit on the possible scenarios. The fact that we find quiescent massive galaxies at high redshifts requires of a quenching mechanism that is rapid, in order to have halted the star formation activity in such early times; and efficient, since higher M_{star} galaxies have been observed to inherently have higher SFR.

It becomes clear then that the study of the ISM across cosmic time, and more specifically of gas in high redshift quiescent galaxies is a crucial piece of the puzzle. It means to find the unused or remaining gas reservoirs. To study them at high redshifts, poses a challenging task, not only because of the technical limitations of the data acquisition but for its subsequent processing and interpretation. Contrarily to the study of the ISM in SFG, this is a new and evolving study field. Considering the current methods, studying gas means to constrain the FIR properties of galaxies, these being: $M_{gas}, f_{gas}, M_{dust}, T_{dust}, \tau_{dep} and L_{IR}$. The shape of the FIR SED of high z QGs remains still unexplored, due to the photometric data required to probe its most important features, these being the peak of the FIR SED and the Rayleigh-Jeans tail (R-J tail). Understanding these features helps to build models and evolution tracks that can be used to understand the properties implied in the SED, mentioned above.

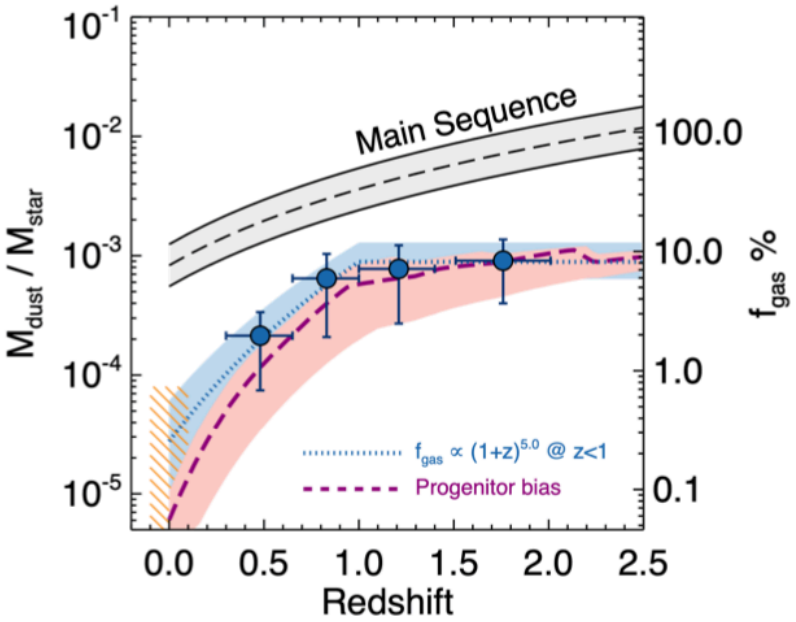

Figure 1.7: M_{dust}/M_{star} measurements in the 0.3 < z < 2.5 range [Magdis et al., 2021]. The grey shaded region is the expected values for the MS [Kokorev et al. 2020]. The blue dashed line represents the best fit to the measurements and the purple one does the same taking into account the progenitor bias analysis of [Gobat et al., 2020]. The conversion of M_{dust} to f_{gas} is done with a gas to dust ratio assuming solar metallicity (δ_{GDR}=92).

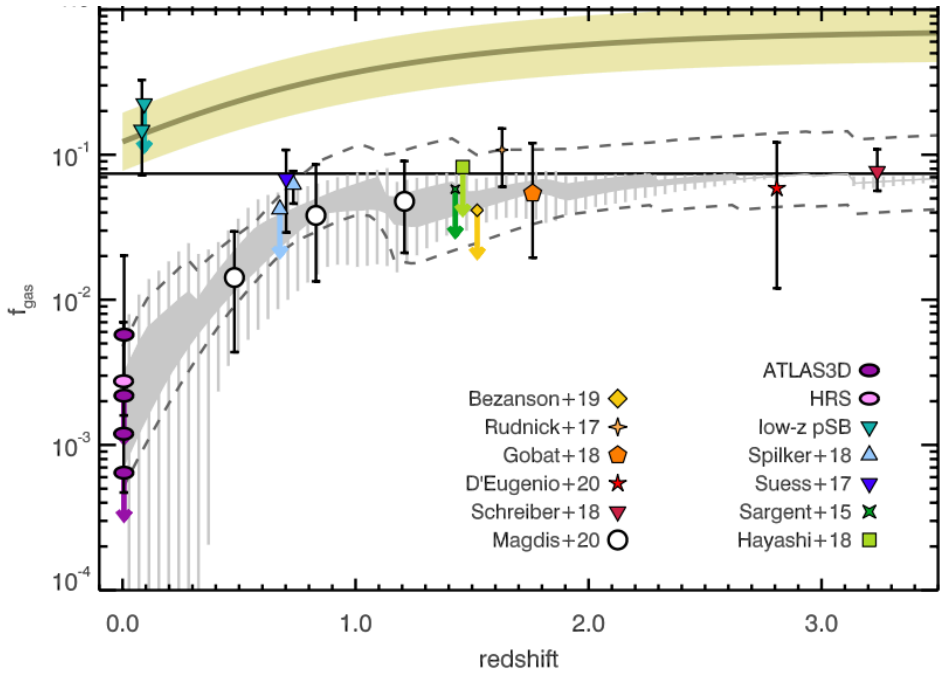

Figure 1.8: Evolution of f_{gas} of QGs with redshift. Smaller symbols represent individual galaxy observations and the bigger ones represent measurements obtained from stacked ensembles. Further information at [Gobat et al., 2020].

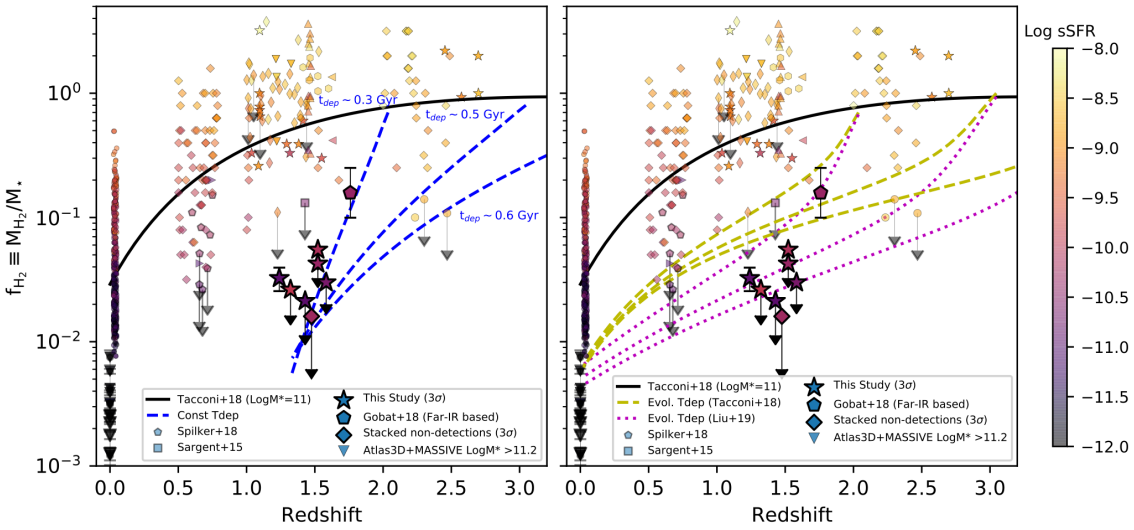

Figure 1.9: f_{gas} measurements presented by [Williams et al., 2021]. The star symbols represent their obtained measurements of individual sources using CO line emission. All galaxies are color coded according to their log(sSFR).The black line represents the f_{gas} of the main sequence for an stellar mass of $10^{11} M_{\odot}$. The dashed and dotted lines correspond to different depletion time models: in blue models with constant depletion times, in yellow models with a varying τ_{dep} according to scaling relations and in purple the depletion time models calculated by [Liu et al., 2019]. More information at [Williams et al., 2021]

In the above figures the most recent results for gas fraction measurements can be seen. Figure 1.8 shows that indeed quiescent galaxies seem to have lower gas fractions that main sequence galaxies, represented by the green shaded area. The high gas fraction observed in the higher redshift measurements is attributed to the progenitor bias. This effect refers to the observational trend that arises when studying quiescent galaxies. It can not be known if a galaxy has left the MS at an early redshift and has evolved passively since

then or if it has lately become an early type galaxy. Therefore, if only high redshift QGs are selected, one excludes the late type galaxies that will eventually become quiescent at lower redshifts. The effect of this bias is usually an underestimation of the evolution of the quiescent population. Recent studies of the evolution of gas across cosmic times [Gobat et al., 2020; Magdis et al., 2021] reveal that the decrease in M_{gas} is sharply followed by a decrease of in SFR. There also seems to be a decrease of M_{dust} from z $\sim$ 1 to z $\sim$ 0, representative of consumption of gas without replenishment. At 1 < z < 2, the evolution of M_{dust} flattens. The ISM conditions of quiescent galaxies does not seem to evolve with redshift, which shows that possible different quenching mechanisms at different redshifts result similar ISM properties. The final conclusions are that the evolution of f_{gas} is a combination of the non evolution of ISM conditions, the observed progenitor bias at z < 1 and the passive evolution of QGs. However, results obtained from individually observed galaxies, see Figure 1.9, reveal a 3σ upper limit lying well below the measurements shown in Figure 1.8. Such low measurements imply that quenching mechanisms are much more efficient than previously thought and that quiescent galaxies do not have considerable amounts of gas left after they become quenched. The difference could be due to the fact that measurements in Figure 1.9 were obtained from more massive galaxies ($M_{star} > 10^{11.2} M_{\odot}$) and that their gas masses were calculated from CO conversion coefficients (α_{CO}) instead of converting the FIR emission into an M_{gas} measurement.

1.4 Motivation

The different kinds of methods and techniques used for the study of the ISM at high redshifts and the novelty of the field have resulted so far in contradictory and inconclusive results. Further constraints must be ascertained in order to make robust predictions on the evolution in f_{gas} and quenching mechanisms. It is agreed that the f_{gas} of QGs is smaller than that of the MS at their correspondent redshift, the question that needs to be answered is: by how much? Studies that obtain f_{gas} estimates from individual galaxy observations may suffer from selection biases, i.e the fact that the estimates of a small number of galaxies might not be representative of the entire quiescent population. Estimates obtained from stack ensembles have been carried out on surveys with large beam sizes, and therefore are subject to blending biases. The aim of this project is to investigate the viability of selection a representative sample of high redshift QGs, large enough to get rid of selection biases and study it with a high angular resolution map, through which blending biases are greatly reduced. This way the weaknesses of the two different approaches can be circumvented and promising results can be obtained.

The highest resolution FIR observations are obtained through ALMA, whose power has already been directed to the Great Observatories Origins Deep Survey (GOODS) field, which is the most deeply documented field in the sky. A large range of surveys have been performed in it (e.g. ZFOURGE [Straatman et al., 2016], 3D-HST [Skelton et al., 2014], CANDELS [Grogin et al., 2011]). Their recollected deep photometric data makes it available to identify a considerable population of high redshift quiescent galaxies which combined with the deepest ALMA observations of the GOODS-S field, i.e. the ALMA-GOODS 1.1 mm map [Franco et al., 2018; Franco et al., 2020a; Franco et al., 2020b; Gómez-Guijarro et al.,in prep], can obtain measurements of their R-J tail emission, which will help draw a more precise picture of the evolution of the average high redshift quiescent population ISM and study their gas and dust masses.

Chapter 2

Data

The choice of a reliable data set is of extreme importance. Moreover, it must cover a deep enough field so that a considerable number of high redshift galaxies are available. GOODS-S . This chapter will clarify our chosen sky field and catalog, explaining their properties and characteristics, together with why they are appropriate for this project.

As explained in section 1.4, this project is supported on the opportunity brought by the deep high resolution map that has been created with ALMA in the GOODS-S field [Gómez-Guijarro et al.,in prep]. In it, we find the deepest and most extensive photometric studies of the entire sky, comprising deep observations of Spitzer, Herschel, Hubble, Chandra etc. which allow to obtain a large enough amount of high redshift quiescent galaxies to make a compelling stacking of their FIR emission and analyse their properties. Due to the nature of the stacking procedure, it is critical to ensure the quiescence of the selected galaxies. Either directly or indirectly, photometric data points and the redshift derived from them are the base to select quiescent galaxies. A catalog with quality photometric redshifts and enough photometric fluxes to make reliable SED fittings is necessary. Not only that, but it must be large enough to be able to collect a minimum number of quiescent galaxies that fall within the footprint of the GOODS-ALMA survey.

2.1 ZFOURGE catalog

Among the latest, most complete catalogs we find the *FourStar galaxy evolution survey*, ZFOURGE. Covering a total of 400 arcmin^2 in three different fields : COSMOS, CDFS (Chandra Deep Field South) and UDS. Containing approximately 70000 sources extracted using the K_s band. The use of the K band is convenient for two major reasons. First, as the optical rest frame and near-IR trace galaxies according to their stellar mass, the K band selects galaxies according to this stellar mass up until z $\sim$2 [Gavazzi et al., 1996], thus it tends to be more mass complete than other detection filters. The second reason is that since spectral shapes in the before mentioned range of the spectrum are very similar, it makes the K band free of biases in favour of a particular class of galaxy. Selection criteria with other filters are more sensitive to the SFR of galaxies, and therefore become biased to detect active galaxies opposed to passive quiescent ones [Cimatti, 2003]. Using the *FourStar* NIR camera on the Magellan Baade telescope, and its available bands: J_1, J_2, J_3, H_s, H_l and K_s; the survey covers the same range as the classical J, H and K filters. This represents an extreme advantage when probing high redshift galaxies. The Balmer break, which at rest frames occurs at 4000 Å, moves into the near IR spectra at redshifts $z > 1.5$. It is therefore useful to have narrower bands in order to measure the break in a more precise way. This catalog is able to then obtain, with the use of EAZY [Brammer

et al., 2008], reliable photometric redshifts for its sources, together with stellar population parameters and other characteristics achieved with FAST [Kriek et al., 2009]. Through the entire analysis ZFOURGE assumes an standard ΛCDM cosmology with Ω_M=0.3, Ω_Λ=0.7 and H_0=70 km s^{-1} Mpc^{-1}.

The image processing and preparation first requires, after processing the raw data, to make a photometric calibration of the filters. To do so, a standard star is selected, with a K_s magnitude ≈15.5, the star is then observed photometrically after making an observation with a determined filter. The obtained measurements are then calibrated with the primary observations of the standard star. Then, the actual depth of the *FourStar* pictures was calculated with the rms error of the background pixels. After randomly placing 5000 apertures all over the image where the background had already been subtracted, their flux is calculated giving as a result the variation in the background noise, of which the standard deviation σ is calculated. After making a flux correction for possible missing light outside the 0.6" aperture, the limiting depth of the image is set at 5σ. Which in AB magnitude is calculated as following:

$$depth(5\sigma) = zp - 2.5log_{10}[5\sigma \cdot appcor] \tag{2.1}$$

Where *zp* and *appcor* are the magnitude zeropoint and the aperture correction factor respectively, the latter ranging between 1.7-2.6. This process shows that the individual *FourStar* images have a limit depth of 24.8 AB for CDFS. Combining the *FourStar/*K_s images with preexisting deep K-band imaging, taken from *HST* imaging from the Cosmic Assembly Near-IR Deep Ex- tragalactic Legacy Survey (CANDELS,[Grogin et al., 2011]), super-deep detection images are created with a depth of detection (5σ) in CDFS ranging between 26.2 and 26.5 in AB magnitude [Straatman et al., 2016].

The catalog is afterwards enlarged by adding another 39 filters from other public surveys (see Table 2.1). In order to complement the archive with far-IR information, deep *Spitzer/MIPS* observations at 24 μm and public observations of *Herschel/PACS* at 100 and 160 μm are added, though they are only available for CDFS. However this does not pose a problem for the current project since it is this latter field the one we are interested in. All of the filter information is given in the main ZFOURGE file, which mainly consists of the *id*, pixel coordinates ("x, y"), "*RA*" and "*DEC*", followed by the fluxes "f[]" and error "e[]" in μJy and weight corresponding to median normalized "w[]" of each filter. Finally a "*use*" column is used to flag extremely reliable sources: S/N>5, not catastrophic EAZY or FAST fit etc.

Together with this main file, other catalogs are given containing compelling information. First the EAZY photometric redshift catalog shows information concerning the EAZY fit parameters, such as derived photometric redshift with/without a K luminosity prior "*z_a*"/"*z_m*1" , minimum χ^2 value, best fit redshift "*z_p*", default derived redshift and its peak probability "*z_peak*" and "*peak_prob*". Another "z_s*pec*" column is added for sources that have a measured spectroscopic redshift. Then we also find the FAST extracted stellar population parameters catalog, among which we highlight the SFR[$M_\odot$/yr], specific SFR[1/yr] and stellar mass [$M_\odot$], all of them in logarithmic scale ($\log_{10}()$).

The last, and also most appealing characteristic of the ZFOURGE survey is that a great effort has already been invested into applying the *UVJ* quiescent selection criteria in search of quiescent galaxies. On top of that, they went on to confirm the quiescence of those galaxies with the calculated mean value of their sSFR=0.5±1.0 x 10^{-10}, and validating the *UVJ* classification up to z = 3.5 [Straatman et al., 2016].

Filter	λ_c (μm)	FWHM ($''$)	zeropoint (AB mag)	offset	galactic extinction
B	0.4318	0.73	22.097	-0.029	-0.032
I	0.7693	0.73	22.151	0.019	-0.014
R	0.6443	0.65	27.321	-0.148	-0.020
U	0.3749	0.81	25.932	-0.181	-0.037
V	0.5919	0.73	22.968	-0.010	-0.022
Z	0.9036	0.73	21.378	0.041	-0.011
H_s	1.5544	0.60	26.618	-0.031	-0.004
H_l	1.7020	0.50	26.588	-0.051	-0.004
J_1	1.0540	0.59	26.270	-0.041	-0.009
J_2	1.1448	0.62	26.558	-0.043	-0.006
J_3	1.2802	0.56	26.521	-0.067	-0.006
K_s	2.1538	0.46	26.851	-0.083	-0.003
$NB118$	1.1909	0.47	24.668	0.000	-0.006
$NB209$	2.0990	0.45	24.786	0.000	-0.003
$F098M$	0.9867	0.26	25.670	0.011	-0.008
$F105W$	1.0545	0.24	26.259	-0.002	-0.007
$F125W$	1.2471	0.26	26.229	0.004	-0.005
$F140W$	1.3924	0.27	26.421	-0.027	-0.004
$F160W$	1.5396	0.27	25.942	-0.000	-0.004
$F814W$	0.8057	0.22	25.931	-0.004	-0.011
$IA484$	0.4847	0.81	25.463	-0.013	-0.024
$IA527$	0.5259	0.87	25.639	-0.059	-0.022
$IA574$	0.5763	1.01	25.543	-0.148	-0.019
$IA598$	0.6007	0.69	25.962	-0.040	-0.018
$IA624$	0.6231	0.67	25.887	0.014	-0.017
$IA651$	0.6498	0.67	26.072	-0.062	-0.016
$IA679$	0.6782	0.86	26.105	-0.080	-0.015
$IA738$	0.7359	0.83	26.003	-0.003	-0.013
$IA767$	0.7680	0.77	26.000	-0.028	-0.012
$IA797$	0.7966	0.74	25.986	-0.022	-0.012
$IA856$	0.8565	0.74	25.713	-0.007	-0.010
WFI_V	0.5376	0.96	23.999	-0.076	-0.021
WFI_Rc	0.6494	0.84	24.597	-0.038	-0.016
WFI_U38	0.3686	0.98	21.587	-0.291	-0.032
$tenisK$	2.1574	0.86	24.130	0.233	-0.002
$KsHI$	2.1748	0.45	31.419	0.022	-0.003
$IRAC\_36$	3.5569	1.50	20.054	-0.016	0.000
$IRAC\_45$	4.5020	1.50	20.075	0.005	0.000
$IRAC\_58$	5.7450	1.90	20.626	0.023	0.000
$IRAC\_80$	7.9158	2.00	21.803	0.022	0.000

Table 2.1: List of passband filters in ZFOURGE-CDFS [Straatman et al., 2016].

Table 2.1 provides the central wavelength of the filters in μm and their FWHM in arcseconds. It also gives their effective zeropoints, which include the galactic extinction and offset corrections, such that the effective zeropoints is calculated as: $zp = zp_I$ + offset + galactic extinction. It is critical for the project that when the ZFOURGE catalog is mentioned, it refers to the part of the survey focused on CDFS, since that is the field where the GOODS-ALMA survey is located at.

2.2 GOODS-ALMA survey

The Atacama Large Millimeter/submillimeter Array (ALMA) together with the enormous efforts made in the obtaining and processing of deep sky data have opened the window to explore the dust emission of QGs at high redshift. ALMA is composed of fifty 12-m antennas in its main array with an additional twelve 7-m and four 12-m antennas in its Total Power Array. Its band coverage ranges from 35 to 950 GHz (approximately 315-8500 μm), making it able to study the ISM properties of galaxies from the Rayleigh-Jeans tail to the SED peak. Its most advantageous property is its outstanding angular resolution, which spreads from a few arcseconds to ~ 10 *mili*-arcseconds, which represents a capability to discern a distance of a couple hundred parsecs at a distance of z$\sim$2. Located on the

plateau in the Atacama dessert at 5,000 meters, it stands at an unbeatable location for astronomical observations.

GOODS-ALMA is a 1.1 mm galaxy survey that covers a total area of 72.42 arcmin^2 in the GOODS-South field centered at α= 3^h 32^{min} 30^s, δ= -27deg 48' 00". Removing the edges, which are the least sensitive regions of the map, reduce its total surveyed area to 69 arcmin^2. The second version of the map, known as GOODS-ALMA 2.0: is a combined version of two images taken with different antenna configurations. These two configurations produced a high resolution and low resolution map. The latter, due to lower observation time is shallower than the high resolution one. The latter, even if deeper, has a higher resolution that might dilute the signal. The combination of these two maps, presented by [Gómez-Guijarro et al., in prep] is built as a version that combines the strengths of both.

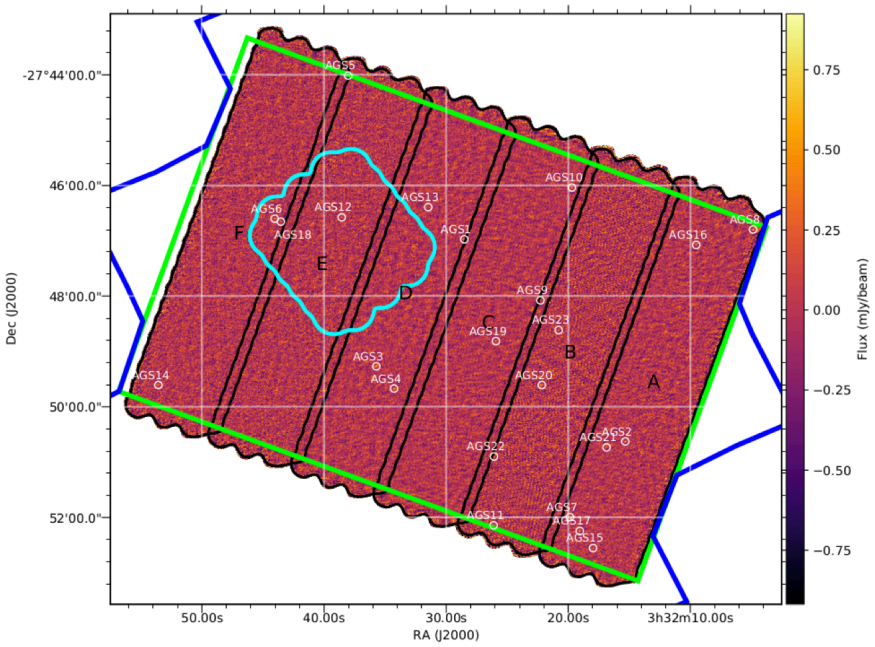

Figure 2.1: GOODS-ALMA 1.1 mm footprint. In blue the GOODS-S field, in green the deep HST-WFC3 region. The black regions delineate the different individual submosaics which compose the entire survey [Zhou et al., 2020].

First, a high resolution survey was produced with an extended antennae array configuration, able to discern smaller spatial scales. This version, presented by Franco et al., 2018, reached a sensitivity of σ = 89 μJy beam^{-1} with an angular resolution of 0.251"×0.232" calculated as beam FWHM . The map is composed of of 846 different pointings, divided in 6 different parallel mosaics, inclined 70deg (named A-F in Figure 2.1). Each mosaic consists of 141 pointings, each separated by 0.8 × HPBW, the primary half power beam width of the antenna; covering a total 6.8'×1.5' area, which is marginally overlapping with its neighbour mosaics. Each pointing required an observation time of *sim* 60 s, summing up to three execution blocks per mosaic. The highest frequencies of band 6 were selected to perform the observation, due to them being optimal for dust continuum observations. The correlator was then optimised at 264.9 GHz (λ=1.13 mm) using four different spectral windows centered at 255.9 GHz, 257.9 GHz, 271.9 GHz and 273.9 GHz, all of them with a bandwidth of 1875 MHz, accounting for a total width of 7.5 MHz. The antenna configuration used a maximum baseline distance of 1500 m, using 40 antennae. These observations were carried out on late summer 2016, under optimal water vapor conditions

(precipitable water vapor $\sim$ 1 mm).

The low resolution array, carried out mainly between January and and March 2019, was performed in a very similar way to the high resolution one. The map, presented by [Goméz-Guijarro et al.,in prep] was also composed of 6 mosaics, all of them in an identical disposition and with the same size as the other map. The only difference is the antennae configuration used , which was more compact, with a maximum baseline distance of 360.5 m. A total of 18 execution blocks were used for the six mosaics, which account for 14.39 hours of observation time in similar precipitable water vapor conditions (*approx* 1.16-2.9 mm). The achieved sensitivity of the map is of 95.2 μJy beam^{-1} with an angular resolution of 1.33"$\times$0.935".

The data was processed in an analogous manner for both maps in order to avoid systematic errors. Due to the lack of very bright sources and large flux ranges, the usage of the CLEAN algorithm was avoided, in order to avert possible biases. A comparison between the clean and dirty version of the maps showed that its noise levels were practically the same [Gómez-Guijarro et al.,in prep]. The imaging was then performed with a multifrequency synthesis algorithm, CASA. In both maps, and therefore the combination, the sensitivity and angular resolution changed slightly due to different observing conditions between pointings. Accordingly, their values are averaged to obtain the final data. Each mosaic of the high and low resolution maps was combined independently to then form the final GOODS-ALMA 2.0 map, which achieved a sensitivity σ=68.4 μJy beam^{-1} and a resolution of 0.447"$\times$0.418". All these parameters have been clearly portrayed in table 2.2, produced by [Goméz-Guijarro et al.,in prep].

2.2.1 Stacking procedure

A Python code was written in order to produce mean stacked images of a number of galaxies selected in the GOODS-ALMA map. Firstly it reads the catalog from which the galaxies will be selected, being mandatory that it contains information on the RA and DEC of the galaxies, so that they can be translated into pixel coordinates. Then a selection according to the catalog properties is defined, such as redshift, SFR, M_{star}, ΔMS, S/N of 24 μm filter etc. Such selection will retrieve N number of galaxies from the chosen catalog. Then the software proceeds to make a $M_0 \times M_0$ pixel cutout centered around the previously calculated pixel coordinates of each galaxy. To translate the astrometric data into pixel coordinates, the Astropy package [Astropy Collaboration et al., 2018] is used, which reads the RA and DEC center of the map as well as the angle value equivalent to a map pixel. For the GOODS-ALMA map file, which consists of an array of 18000$\times$18000 pixels, each pixel equals 0.05 arcseconds.

When making the cutout around each galaxy it must be taken into account that the true center of the galaxy might not be an integer and therefore making a cutout of $M_0 \times M_0$ pixels around it becomes impossible. An approach that can circumvent this problem is to interpolate the flux values between each pixel with a spline and recalculate the flux of each pixel as a function of the ones around it. Doing so, the cutout can then be centered around the true coordinates of each galaxy. To do so, the Scipy package [Virtanen et al., 2020] offered 2D interpolation method which fits a bivariate spline to the flux values of all pixels, thus allowing to calculate flux values between them. It is then made a second cutout of size $M \times M$ (such that $M_0 > M$), whose central pixel coincides with the astrometric coordinates of the galaxy.Next they are stacked in a matrix of size $N \times M \times M$ so that the stacked image

flux can be calculated. For mean stacking:

$$F_{ij} = \sum_{n=1}^{N} \frac{f_{ij,n}}{N} \tag{2.2}$$

Where F_{ij} is the stacked image flux for the i, j pixel and $f_{ij,n}$ is the flux for the i, j pixel of the nth galaxy in the selection. Finally, the image is normalized to a [0,1] scale and smoothed with a gaussian filter included in the Matplotlib library *imshow* function.

To assess the proper functioning of the code a test trial is attempted with the ZFOURGE catalog. The cutout sizes were of M_0 =151 and M=141, resulting in a final cutout of 7.05"×7.05". In order to obtain a clear detection, the most massive and brightest K band sources in the GOODS-ALMA map were chosen ($M_{star} > 10^{10.5} M_{\odot}$), summing up to a total 450 galaxies. After performing mean stacking, this was the resulting image:

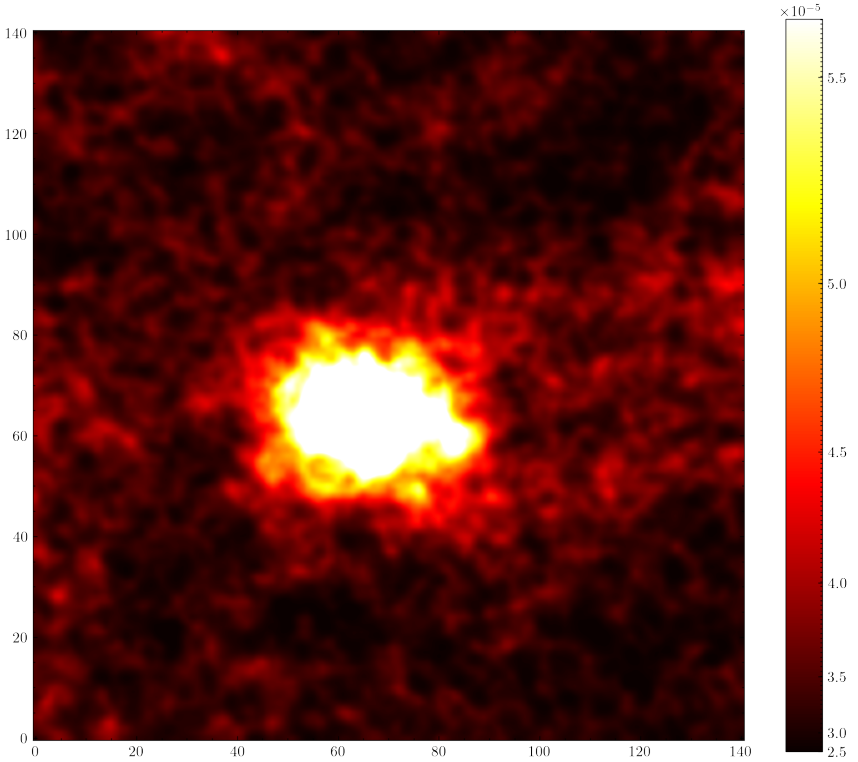

Figure 2.2: 7.05"×7.05" (141×141 pixels) stacked cutout using GOODS-ALMA images of 450 galaxies with $M_{star} > 10^{10.5} M_{\odot}$ in the ZFOURGE survey.

A clear detection can be distinguished, opposed to the empty background. However, it is observed that the flux is not evenly scattered around the central pixel (i=70,j=70) but it is shifted towards bottom left of the image. The fact that the mean flux of 450 galaxies is not properly centered leads to the possible conclusion that there might be an offset in the astrometric data. For that reason,the apertures used to calculate the photometric flux of the stacked images, are placed on an slightly shifted position from the center of the image, 5 pixels below and to the left. An image with no apparent flux (produced by stacking 10 randomly selected QGs) has no visible bulk of flux at its center, and it simply shows the noise fluctuations of the data (see Figure 2.3)

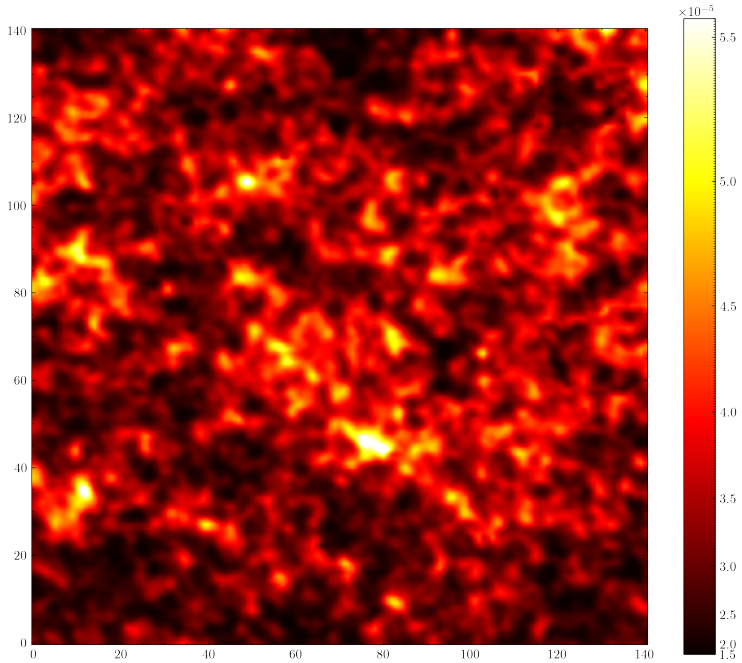

Figure 2.3: 7"×7" (141×141 pixels) stacked cutout using GOODS-ALMA images of 10 randomly selected quiescent galaxies using the UVJ selection method, which does not show any observable flux but scattered noise.

	High-res						Low-res						Combined	
Slice	Date	Ant.	t target (s)	t total (s)	Beam (arcsec × arcsec)	σ (μJy beam^{-1})	Date	Ant.	t target (s)	t total (s)	Beam (arcsec × arcsec)	σ (μJy beam^{-1})	Beam (arcsec × arcsec)	σ (μJy beam^{-1})
A	2016 August 17	42	46.52	72.12	0.″251 × 0.″199	89.6	2018 July 17	44	46.30	65.50	1.″38 × 1.″07	93.2	0.″268 × 0.″242	68.1
	2016 August 31	39	50.36	86.76			2019 January 19	47	48.03	68.18				
	2016 August 31	39	46.61	72.54			2019 January 19	46	48.03	67.45				
B	2016 September 01	38	46.87	72.08	0.″207 × 0.″185	88.8	2019 March 05	43	48.07	71.08	1.″22 × 1.″05	93.2	0.″366 × 0.″321	67.7
	2016 September 01	38	48.16	72.48			2019 March 05	43	48.05	68.15				
	2016 September 02	39	46.66	75.06			2019 March 12	42	48.08	70.10				
C	2016 August 16	37	46.54	73.94	0.″248 × 0.″234	89.1	2019 March 17	44	48.05	69.48	1.″48 × 0.″86	96.0	0.″419 × 0.″377	68.6
	2016 August 16	37	46.54	71.58			2019 March 17	47	48.05	70.25				
	2016 August 27	42	46.52	74.19			2019 March 19	47	48.03	67.05				
D	2016 August 16	37	46.54	71.69	0.″257 × 0.″233	88.8	2019 March 21	47	48.05	69.17	1.″29 × 0.″94	96.4	0.″460 × 0.″429	68.7
	2016 August 27	44	46.52	72.00			2019 March 21	45	48.07	69.98				
	2016 August 27	44	46.52	72.08			2019 March 22	44	48.03	69.28				
E	2016 August 01	39	46.54	71.84	0.″284 × 0.″260	88.7	2019 March 05	46	48.07	71.25	1.″41 × 0.″97	95.7	0.″452 × 0.″411	68.4
	2016 August 01	39	46.53	72.20			2019 March 07	46	48.03	69.62				
	2016 August 02	40	46.53	74.46			2019 March 14	42	48.03	70.95				
F	2016 August 02	40	46.53	72.04	0.″294 × 0.″256	88.8	2019 March 21	45	48.05	69.37	1.″28 × 0.″95	96.4	0.″510 × 0.″455	68.8
	2016 August 02	41	46.53	71.61			2019 March 22	44	48.02	69.57				
	2016 August 02	39	46.53	71.55			2019 March 22	47	48.07	67.62				
Mean					0.″251 × 0.″232	89.0					1.″33 × 0.″935	95.2	0.″447 × 0.″418	68.4

Table 2.2: Summary of GOODS-ALMA maps data

Chapter 3

Analysis

The following chapter describes the analysis performed on the data sets pertinent to the final results of the project.

3.1 ZFOURGE

The ZFOURGE CDFS field catalogue is divided into different files, each containing aperture fluxes information, photometric redshift data, stellar population parameters among other properties. In order to hasten the data analysis and preparation, it is more suitable to merge all the compelling information in one unique catalogue. This is done using the Topcat [Taylor, 2005] program, which allows to analyse a catalog's information and more importantly, to crossmatch data between different catalogs using a common identifier, such as the galaxy's 'ID'. In the ZFOURGE case, it is decided to merge information from the following files:

1. "*cdfs.v1.6.9.zout*", which contains information concerning the EAZY photometric fit.
2. "*cdfs.v1.6.9.fout*", which contains information about the SED fitting estimates: stellar mass, star forming rate, goodness of fit (χ^2 method).
3. "*cdfs.v1.6.9.rest.v0.9.cat*" which has information rest frame fluxes, in μJy units, of the following filters. From SDSS, *u, g, r , i, z*; from Johnson, *U, B, V*; from 2MASS, *J, H, K* and from tophat *uv13, uv15, uv19, uv22, uv28.*
4. "*cdfs.v1.6.9.sfr.v0.4.cat*" which contains MIPS 24 μm flux and error "$f24, e24$", rest frame 2800 Åluminosity "$L24$" and the UV +IR derived SFR "SFR_UVIR".
5. "*cdfs.v1.6.9.herschel.v0.4.cat*" contains the same information as the last file, however in addition to that it gives the fluxes values and errors for $Herschel/PACS$ 100 μm and 160 μm filters.

In addition to that, the RA and DEC information of each galaxy was added from another external file. All of this crossmatching was performed using the ID of the sources. In the final file, exactly 30911 sources can be found. Finally, the provided fluxes are converted to magnitude values through the following equation:

$$mag = -2.5 \times log_{10}(f) + m_0 \tag{3.1}$$

Where f represents the flux in each band and m_0 the magnitude zeropoint, which given that the ZFOURGE bands fluxes are in μJy, equals 23.9.

A number of properties are included in the final catalog for their importance in the analysis. Concerning redshifts we have 'z$_{phot}$' which represents the EAZY estimated photometric redshifts; 'z$_{spec}$', containing the spectroscopic redshifts included in the ZFOURGE catalog and 'z$_{spec,2}$' which is an additional spectroscopic redshift compilation in CDFS [N.Hathi, private communication]. As a rule, the photometric and spectroscopic redshifts coincide, with just a few disagreements. A new additional column is created, called 'z'. This takes the spectroscopic redshift value, if there is one (prioritizing z$_{spec}$ over z$_{spec2}$) or the photometric estimate otherwise. Finally, the signal to noise ratios of the Spitzer/MIPS and Herschel/PACS (24, 100 and 160 mum) filters are calculated, since they offer information about possible AGN activity or dust obscured star formation.

The stellar masses given in the file containing the stellar population parameters are estimated with the FAST performed SED fitting. Together with them we find the SFR associated to the fitted model for each galaxy, which in the catalog is found as SFR_{mod}. In addition to that, there is another SFR estimate obtained through the UV and IR luminosities: L_{UV} and L_{IR} [Kennicutt, 1998]. L$_{IR}$ is derived with the Spitzer/Herschel 24-160 μm photometry, to which a spectral template is fitted in order to calculate its total luminosity (integrated from 8 to 1000 μm). Then L$_{UV}$ is estimated by integrating the rest frame 1216-3000 ÅUV emission (L$_{UV}$=1.5νL$_{\nu,2800}$) [Straatman et al., 2016]. The star formation rate is then estimated with Bell et al., 2005 conversion:

$$SFR[M_{\odot}/yr] = 1.09{\times}10^{-10}(L_{IR} + 2.2L_{UV}) \tag{3.2}$$

accounting for the younger stellar population UV emission and the dust obscured star formation emission (in the IR), thus obtaining the total SFR for galaxies. In the analysis' first steps, only the SED fitted SFR is taken into account, however later insights its characteristics invite to use SFR$_{UV+IR}$ as a secondary estimate. However, until further notice, the following parts of the analysis take the SFR$_{mod}$ as the nominal SFR.

Once the data table is built, M_{star} vs SFR plots, RA vs DEC, colour-colour diagrams are built in order to have a preliminary analysis of the general properties of the catalogue. Firstly, though, a preliminary selection criteria is applied, to get rid of sources with undetermined photo-z and sources with negative fluxes values in any of the following bands: U, V, J. By doing so, the catalog is reduced to a total amount of 30800 galaxies.

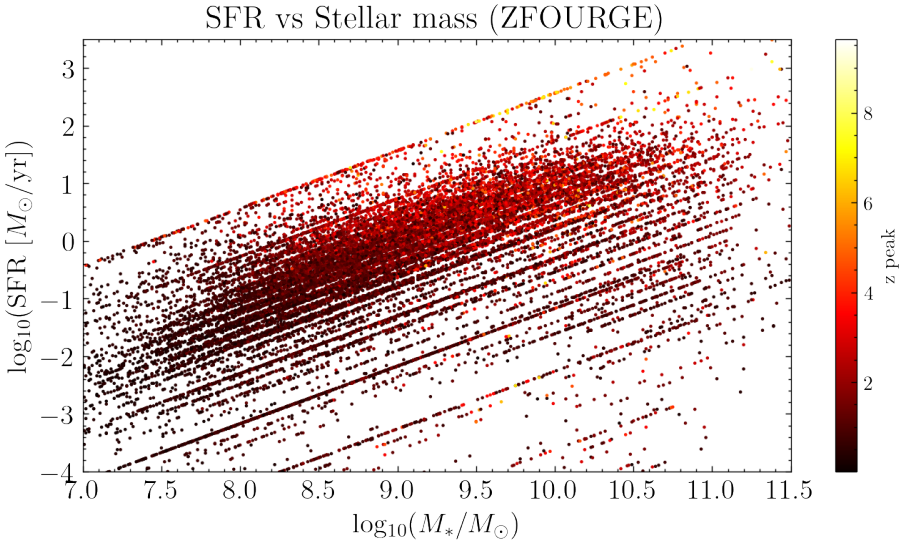

Figure 3.1: log$_{10}$(M_{star}) vs log$_{10}$(SFR) diagram color coded according to their photometric redshift estimates.

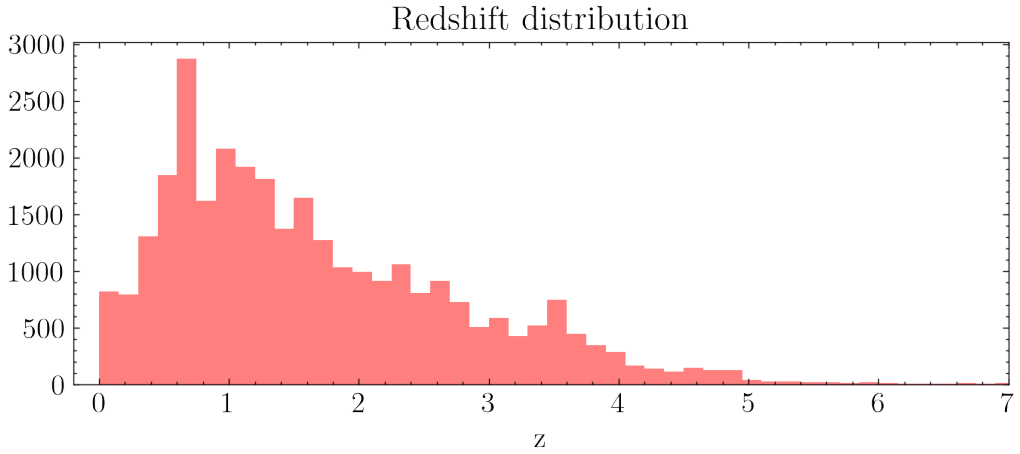

Figure 3.2: Redshift distribution of ZFOURGE catalog.

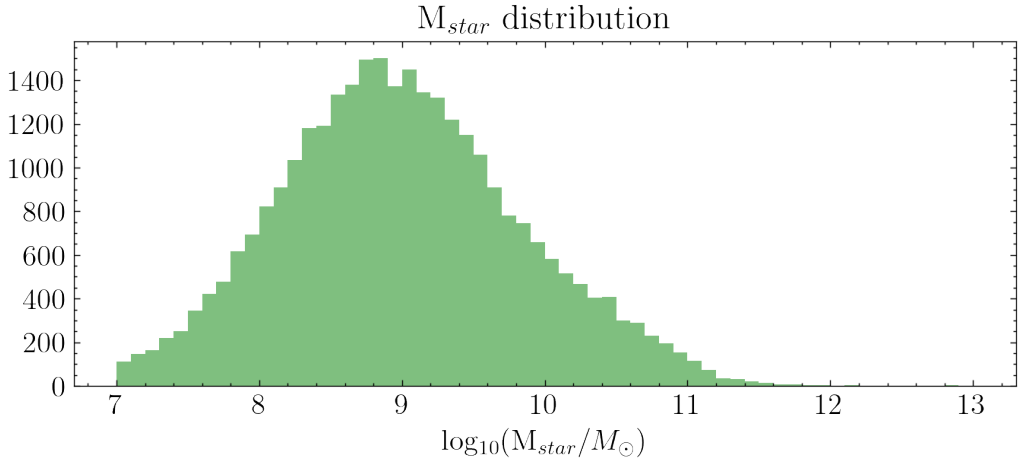

Figure 3.3: M_{star} distribution of ZFOURGE catalog.

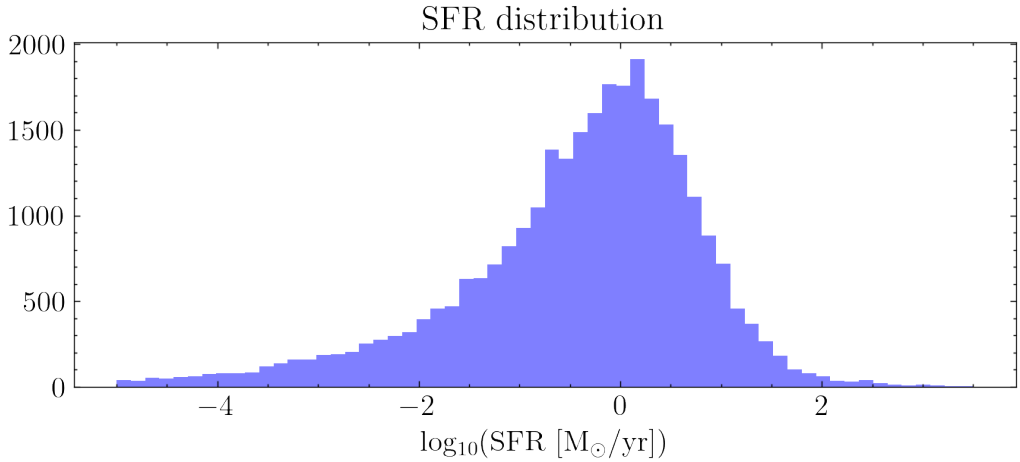

Figure 3.4: SFR distribution of ZFOURGE catalog.

Figure 3.1 shows the clear correlation between the stellar mass of galaxies and their SFR, i.e. the fact that the more massive are, the greater their SFR will be in general. This comes together with the increase in redshift that it is observed in the most star forming galaxies, resembling the fact that most of the star formation took place at high redshifts, during the cosmic noon. The only issue that arises is the potential stratification occurring in the diagram, which results in the upward diagonal lines where most of the sources concentrate, instead of an even spread. This is a possible product of the SED fitting

software, which is limited by the amount of available galxy templates. The maximum recorded photometric redshift is of 9.64, however in Figure 3.6, it becomes clear that most sources are located between 0 < z <1 in addition to the fact that it is nearly certain that the highest redshift sources are star forming galaxies. In Figure 3.3, it can be observed how the population of high M_{star} galaxies ($M_{star} > 10^{10.5} M_{\odot}$) is much less numerous. This poses a primary adversity, in that the higher the M_{star} of the stacked quiescent sources, the larger their M_{gas} is supposed to be, and therefore more easily detected. Not having a large enough number of massive galaxies might bring the mean gas mass of the population down, making its observation more difficult.

In order to select the quiescent population of galaxies, the UVJ colour-colour diagram selection devised by Williams et al., 2009 is used. Its constraints were applied in two different instances, firstly as they were originally proposed (see equation 1.3) and then with a more restrictive version which has an applied offset of 0.1 in magnitude from the original constraints (see blue limits in Figure 3.5). These tighter limits are used to get rid of galaxies that lay just on the limits established in eq. (1.3), which could be galaxies ongoing quenching, crossing to the quiescent region but still not fully quiescent. The criteria results in a total of 2854 QGs that comply with the nominal constraints, and are flagged in the catalog by assigning them a value of 1 in a '*QGwill*1' column (which is set to zero for the rest of the galaxies). The 2570 that comply with the more restrictive constraints are also flagged in an additional column named '*QGwill*2'.

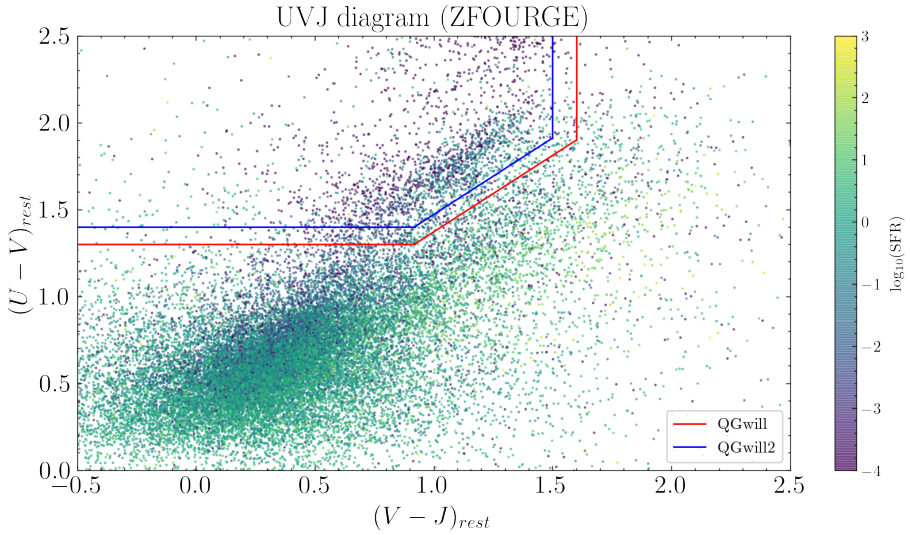

Figure 3.5: UVJ color-color diagram with sources color coded according to their $\log_{10}$(SFR). In red the original QG selection criterion by Williams et al., 2009 and in green the restricted version of the same.

In Figure 3.6, we can see both the M_{star} evolution of the entire ZFOURGE survey, which is an indirect representation of the catalog's detection limit. Since the total luminosity of a galaxy increases proportionally to its stellar mass, and the apparent magnitude also increases proportionally to redshift; the minimum detected M_{star} increases proportionally to redshift. It can also be recognized that most of the QG population has a z < 1 and that an unusually high number of those quiescent galaxies have very low stellar masses, lower than the estimated mass completeness limit (f.e. $M_{star} \approx 10^{7.6} M_{\odot}$ at z = 0.5 and $M_{star} \approx 10^{8} M_{\odot}$ at z = 1) [Tomczak et al., 2014].

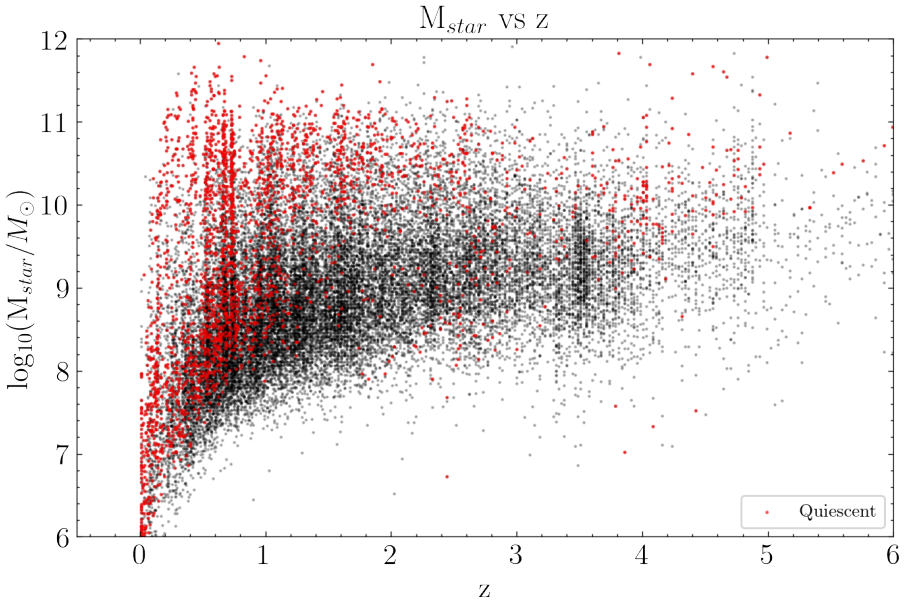

Figure 3.6: M_{star} vs redshift diagram of galaxies in the ZFOURGE catalog, with UVJ selected quiescent galaxies highlighted in red.

The QGs scatter all across the GOODS-s field. The next step is to select those QGs that fall within the GOODS-ALMA map footprint. A rectangular region is defined to exclude the edges of the map (see Figure 3.7) in order to avoid the lower sensitivity areas of the same. The region will also reject galaxies that reside in or close to the map's edges, whose cutouts could bias the final stacked image. The region is defined with the DS9 software [Joye and Mandel, 2003], and then exported to the Jupyter notebook in which all the catalog and map analyses are carried out. Once the map and the region are uploaded, sources that fall within the region are selected (highlighted in red in Figure 3.7). In order to ease the stacking procedure, it was decided that all ZFOURGE galaxies within the rectangle region in the GOODS-ALMA footprint would be selected to form the final catalog. That way, the properties of all galaxies inside the map can be studied, and stacked images of other sources apart from UVJ selected QGs can be obtained. A total of 10755 ZFOURGE galaxies reside in the GOODS-ALMA field, of which 781 are UVJ selected. For clarity reasons, Figure 3.7 only shows the QGs population , but it is representative of the implemented procedure over the entire ZFOURGE catalog.

In order to avoid dusty star forming galaxies to be mistaken for QGs and possible blending biases, a list of of ALMA detected sources was correlated with the catalog using the RA and DEC of both. Doing so, a '*separation*' column was created which measures for each galaxy, the distance to the closest ALMA detected source, in arcseconds. Galaxies that are luminous in the submillimiter-millimeter bands are the one of the most intense starbursts in the universe [Casey et al., 2014]. Their high M_{dust} absorbs the light emitted by the younger stellar populations and radiate it in the FIR. This *separation* column can later be able to reject galaxies that are too close to any of these kind of starbursts and could therefore either be mistakenly identified as quiescent, or alter the flux of the final stacked image.

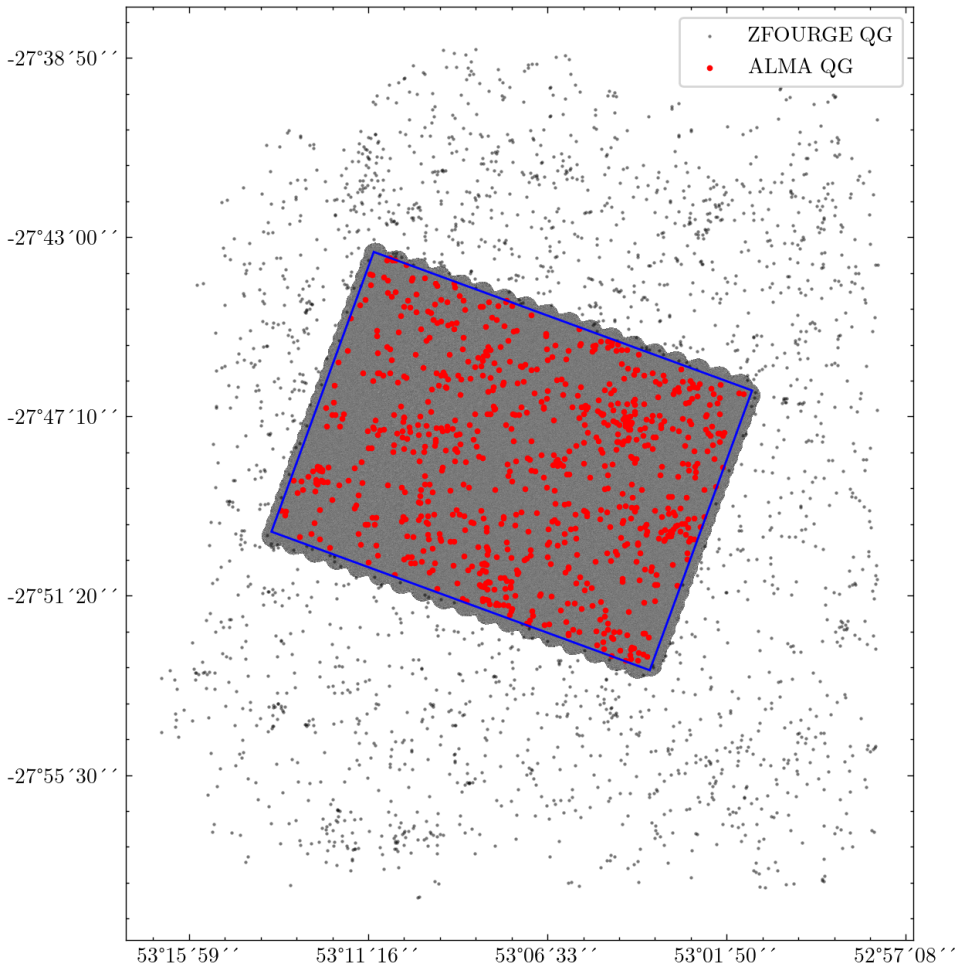

Figure 3.7: Sky map of ZFOURGE quiescent galaxies. In grey, the GOODS-ALMA surveyed area. The blue rectangle represents the defined region that excludes the less sensitive area of the GOODS-ALMA map. Highlighted in red there are the UVJ selected QGs of ZFOURGE survey that are within the limits of the defined region. The rest of QGs are represented by black dots.

During the first analysis of the ZFOURGE catalog, a quick collection of UVJ selected QGs was formed in order to perform a preliminary stacked image and observe the results. It was found that the content of massive quiescent galaxies was not as large as expected and that when stacking QGs with no detected flux at 24 μm ($S/N_{24\mu m}$) , which can be the signature of dust obscured star formation or AGN activity, the final obtained image did not show any apparent flux. This failed stacking attempt, paired up with the stratification of the M_{star}-SFR diagram and the large amount of QG galaxies found below the mass completeness limits led to doubting its reliability to offer a sound population of sources to proceed with the stacking software. Instead of switching to another data source, it was preferred to gain a deeper insight on the models through which the data in the ZFOURGE catalog was calculated.

The first step taken in that direction was to study the individual SED model fits performed by the FAST code. Inside the ZFOURGE catalog release, a file containing the flux of the model for all wavelengths was found. Together with the photometric fluxes data, a Jupyter notebook was created to plot the SED fitted model together with the photometric datapoints and assess the quality of the fit. Even though the majority of the SED fits did not show any quality issues, it was also found that some of the UVJ selected galaxies

showed signs of AGN activity through their near IR data points, being these the IRAC bands. If an AGNi is luminous enough when comparing it to its host galaxy, the dip in the galaxy SED will be filled by the blackbody emission of the AGN, producing a powerlaw in the IRAC bands [Donley et al., 2012],i.e that the SED will grow.

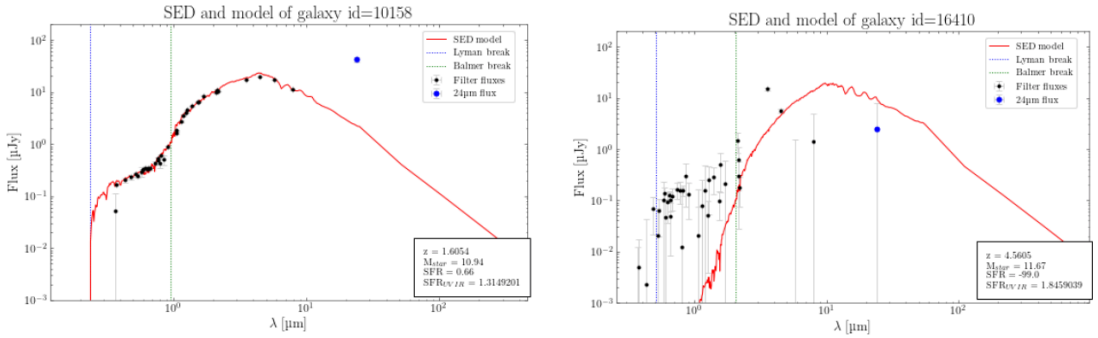

(a) Good quality SED

(b) Poor quality fit

Figure 3.8: Examples of SED fitting together with the recorded fluxes. In red, the FAST selected galaxy model. The black dots represent the measured fluxes in μJy, together with their associated errors. The dotted vertical lines represent the Lyman break (in blue) and the Balmer break (in green). Finally the blue dot represent the Spitzer/MIPS 24 μm flux. The axes are in logarithmic scale.

It was then decided to use the photometric fluxes given in ZFOURGE and re do the SED fitting process again, using EAZY [Brammer et al., 2008] instead of FAST, and compare both catalogs, this new created catalog is referred to as the EAZY catalog.

3.2 EAZY catalog

EAZY is mainly used as a redshift fitting software for galaxies. In addition to that, it can also be used to obtain stellar population parameters. The objective is to use EAZY with the same settings that were used in ZFOURGE, and obtain a catalog with the same information as the one provided by ZFOURGE, to then compare whether the newly created catalog satisfies the requirements to be used in the next attempt of stacking quiescent sources and obtaining a meaningful signal. It is hoped that the run will first obtain a much smoother distribution of sources in the M_{star} vs SFR plane, without having the characteristic layering observed in Figure 3.1, and that the population of quiescent galaxies does not show a large number of sources below M_{star} <8.

As an SED fitting code, EAZY requires to define a parameter file called *zphot.params*, in which the needed inputs (such as catalogs, filters) are described and also the parameters of the SED fitting are established. We set up the conditions in a similar way to those used by Straatman et al., 2016, by looking at their own parameter file. Firstly a file containing the filter responses curves and their errors are uploaded, which contain the responses curves to all filters used in the ZFOURGE survey, together with the filters from Spitzer and Herschel telescopes. Then the templates file is uploaded. In our case another set of templates was used, which were obtained from the template library included in the EAZY software, these being '$fsps_QSF_12_v3_narrow.param$', including a total of 20 different models at different ages. Then EAZY allows to set a condition named '*TEMPLATE_COMBOS*'. If the condition is set to 1, then EAZY will fit a unique model to the photometry, if 2 then a pair of templates will be fit with non negative coefficients. If the value is set to 99, like we did, then it allow EAZY to combine all the available models with non-negative coefficients.

In addition, the template errors are uploaded ($TEMPLATE\_ERROR.v2.0.zfourge$ file), together with the file that defines the wavelength grid. Finally, the file containing the K_s magnitude prior and the photometric zeropoint offsets is also included. Apart from the mentioned conditions and input files, all the other options were set to their default mode. The number of minimum detected colors to perform the fit is set to 3, the IGM absorption is applied according to [Madau, 1995] and the cosmological parameters are set identically to [Straatman et al., 2016], and the redshift grid is defined from 0 to 10 with a 0.05 step. The last two input files are the photometric catalog: '$cdfs.v1.6.11.cat$' and the translate file. Since the filter response files contains information not limited to ZFOURGE filters, the translate file indicates to EAZY which of them are wanted to be included in the SED fitting. In this EAZY run, all the ZFOURGE filters are used, with the addition of the Spitzer/MIPS 24 μm. (See more at appendix B)

The resulting catalog includes redshift and stellar population parameter estimates. The photo-z generally agree with the available spectroscopic redshifts, as it can be seen in Figure 3.9. It was also found that the majority of the SED fits were of great quality (Figure 3.10), and those which were not had a $K_{MAG} > 25$, which as a result became the magnitude limit for the project's studies.

For instance, the galaxy fitted in Figure 3.10 has a ZFOURGE catalog redshift of 0.64 whereas the photometric redshift estimated in this EAZY run is of 0.57. Even if the difference is not substantial, it shows that indeed the new catalog is different to the one provided by Straatman et al., 2016. The layering observed in the M_{star}-SFR plane of the ZFOURGE catalog (Figure 3.1) disappears and a more homogeneous distribution of sources can be observed. There is an abrupt diagonal setting a maximum SFR for each M_{star}, this is a simple limitation of the models used, which cannot assign higher SFR.

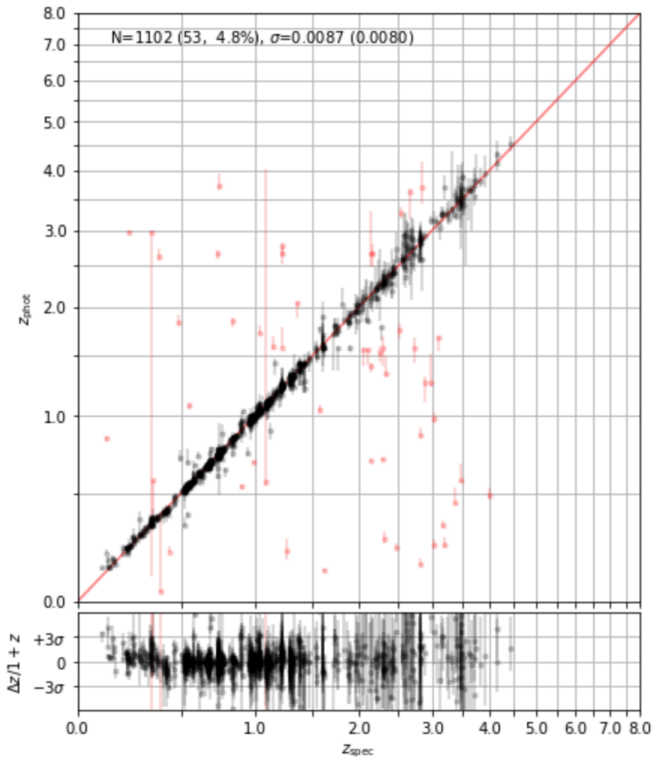

Figure 3.9: Comparison of photo-z obtained by EAZY and spectroscopically obtained redshifts.

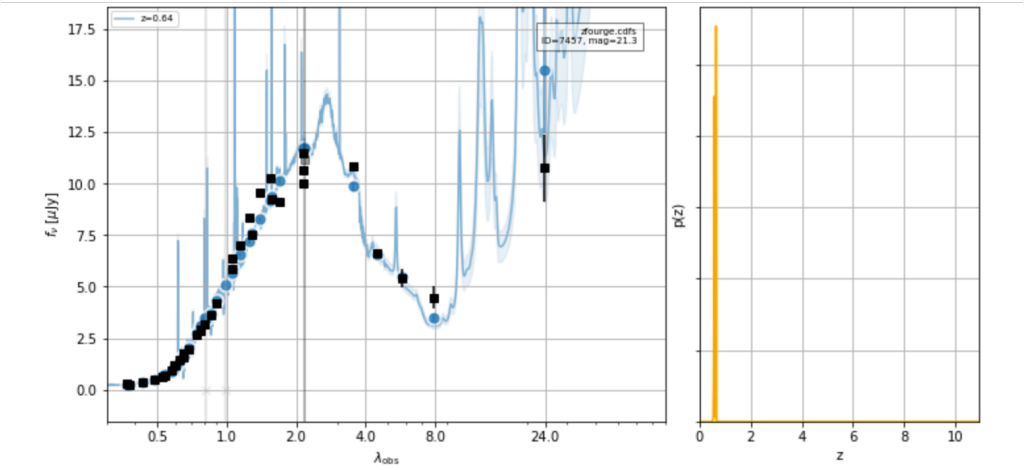

Figure 3.10: *Left:* Example of an EAZY fitted galaxy model. The galaxy model (in blue) is fitted to the photometric data points represented by black squares. The blue circles are the model's flux values at the different photometric filter's wavelengths. The fluxes are given in *mu*Jy and the wavelengths in μm. In the legend there is information about the fitted redshift, as well as the galaxy ID and its K band magnitude. *Right:* The redshift probability distribution function.

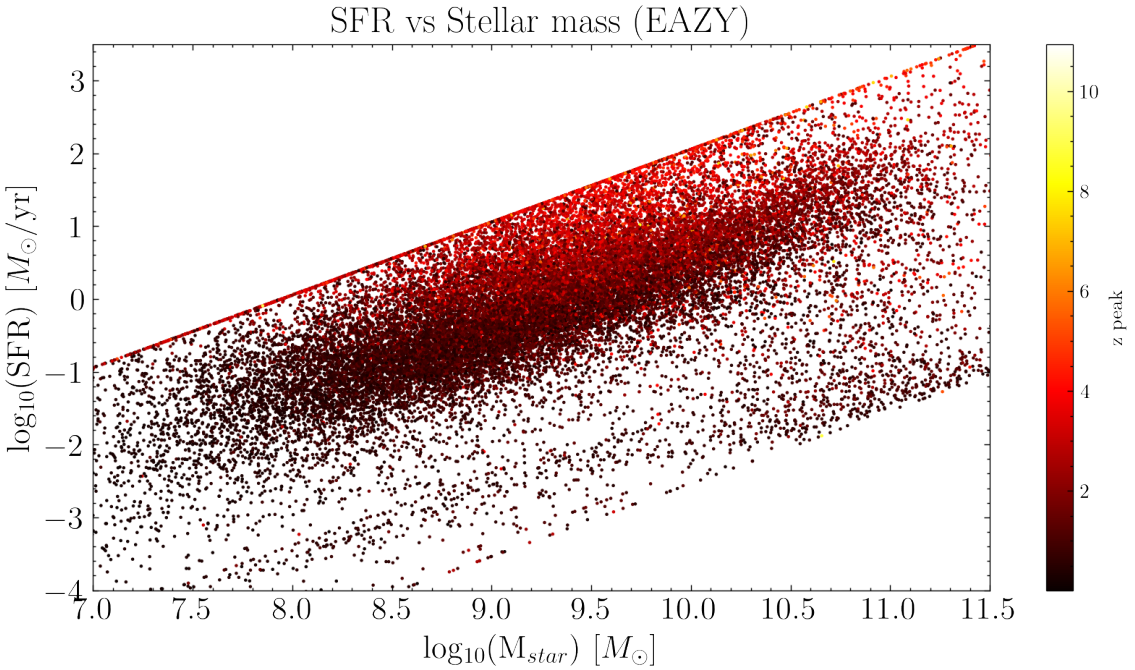

Figure 3.11: $\log_{10}(M_{star})$ vs $\log_{10}(SFR)$ diagram color coded according to their photometric redshift estimates, using the EAZY calculated M_{star} and SFR estimates.

3.3 ZFOURGE-EAZY comparison

First an analogous data processing and analysis process was performed on the EAZY catalog, which included a UVJ colour-colour diagram QG selection, selection of galaxies within the GOODS-ALMA footprint and the addition of FIR filters' fluxes and errors (100, 160 μm), the separation to ALMA detected star forming galaxies. It was also

decided, as a secondary method to detect quiescence, to compute for both catalogs the distance of a galaxy to the main sequence through their distance to the MS; ΔMS = $\log_{10}(\mathrm{SFR}/\mathrm{SFR}_{MS})$. In order to calculate the SFR of the main sequence, the M_{star} and redshift of a galaxy is used as inputs in equation 1.5 Schreiber et al., 2015. A correction is applied to the M_{star} and SFR values given in the catalog to transform their values which are obtained from a Chabrier IMF [Chabrier, 2003] to Salpeter IMF [Salpeter, 1955], by multiplying their values by a 1.7 factor.

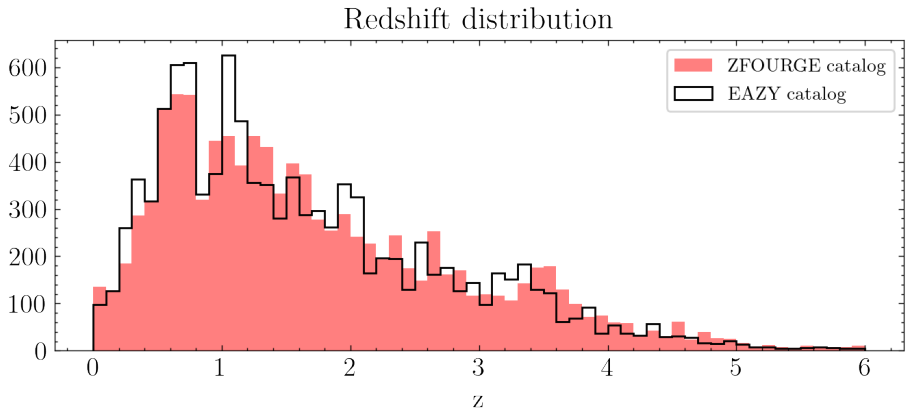

Figure 3.12: Redshift distributions of ZFOURGE (*red*) and EAZY (*black*) catalogs.

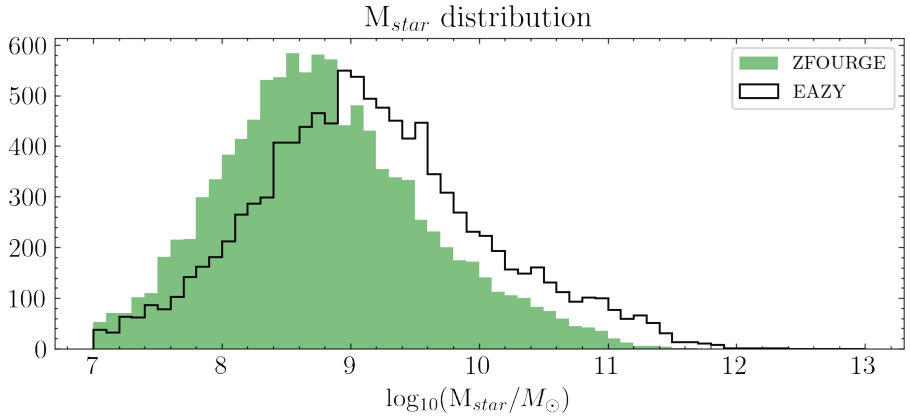

Figure 3.13: M_{star} distribution of ZFOURGE (*green*) and EAZY (*black*) catalogs.

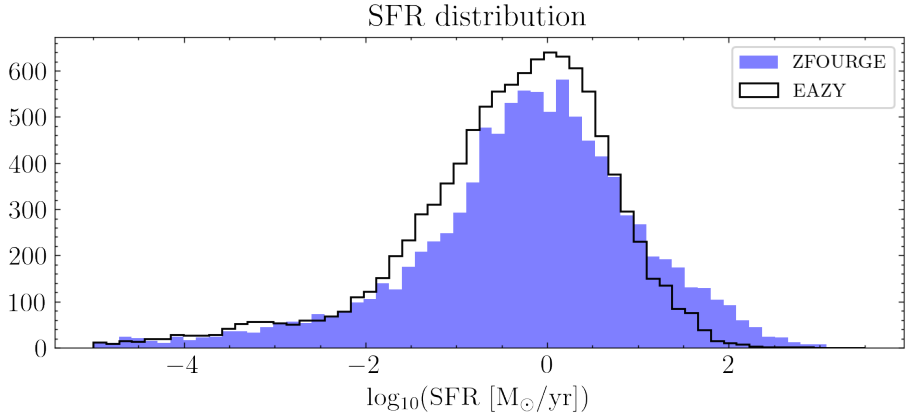

Figure 3.14: SFR distributions of ZFOURGE (*blue*) and EAZY (*black*) catalog.

Both catalogs agree in their SFR and redshift estimations, with the majority of sources being located below z=2 (see Figure 3.12) and the SFR distribution peaking at an SFR $\approx$

1 $M_{\odot}$/yr (see Figure 3.14). There is however a noticeable mismatch between the estimated stellar masses. It seems that there is an overestimation of M_{star} at the EAZY catalog, which is measured to be 50% greater than the ZFOURGE stellar masses. The fact that both distributions look practically equal in shape, but with a constant offset leads to the conclusion that the error must be systematic, however without further study it can not be told whether the error is found in the ZFOURGE or EAZY. The first proposed guess is that the IMF used by ZFOURGE and the one used by EAZY are different, but the measured offset does not match with the previously estimated difference factors of 1.4-1.8 [Chabrier, 2003].

Concerning the UVJ selection, 781 galaxies were identified as quiescent in the ZFOURGE survey, whereas 711 was the final count for the EAZY catalog. 613 of those galaxies are shared between both, which represents a 78% and 86% of their total selections, respectively. A representation of the estimated SFR of those sources is done through a ΔMS versus redshift, which allows to visualize whether the selected QGs are found below the main sequence region or not.

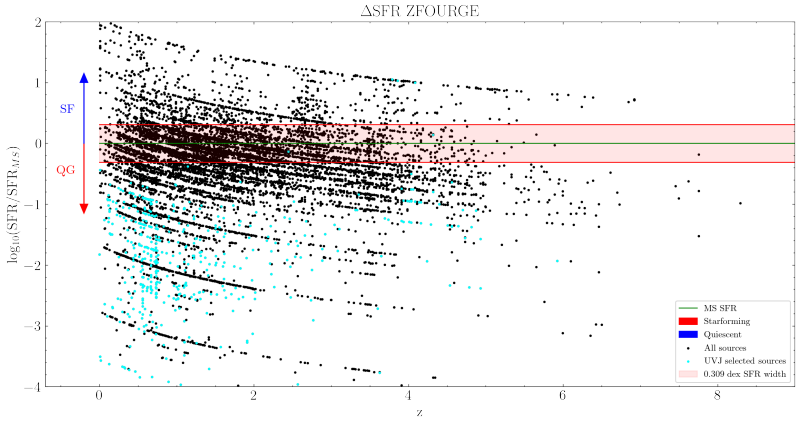

(a) ZFOURGE survey

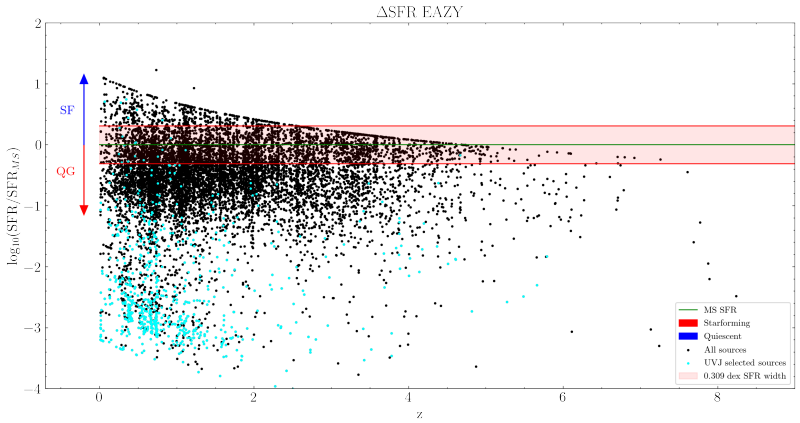

(b) EAZY catalog

Figure 3.15: ΔMS vs redshift plot of ZFOURGE galaxies within the GOODS-ALMA map. The green line represents SFR_{MS} calculated with equation 1.5. The red upper and lower boundaries represent the 0.3 *dex* dispersion of the MS below which sources can star to be considered quiescent or ongoing quenching. In cyan the galaxies identified as quiescent with the UVJ selection criterion.

The quiescent galaxies in both catalogs generally appear well below the main sequence.

The principal issue that arises here is that neither ZFOURGE nor EAZY, but especially EAZY, seem to have the main bulk of their sources within the MS dispersion boundaries, when they supposedly should. As it was observed, the SFR distribution of both catalogs were very similar. Therefore , the fact that the stellar mass has a significant offset might be the reason why EAZY fails to recover the main sequence. This failure, led to the discard of the EAZY catalog as a data set for the stacking attempts. The main reason for this choice is that the time constraints of the project did not allow to make an in depth analysis of how EAZY works, why its calculated stellar masses were different or how were the SFR calculated from the mixture of models that EAZY uses to fit the observed photometry. Finally the fact that it is apparent that the EAZY catalog does not comply with previously accepted galaxy evolution models such as [Schreiber et al., 2015] main sequence SFR estimation led to the same conclusion.

3.4 Final preparation

Due to the decision of using ΔMS as a quiescence selection tool, two different ΔMS where computed, in order to have a robustness check of the star formation rates extracted from the SED fitted models. The first SFR is computed with the latter; whereas the other is calculated with the SFR_{UVIR}, calculated with the L_{UV} and L_{IR} luminosities. However, a major issue with the nature of SFR_{UVIR} was detected. Only 15% of galaxies in both catalogs have a S/N > 3 in the Spitzer/Herschel bands, which brings great uncertainties to the subsequent infrared luminosity required to calculate the SFR with [Bell et al., 2005] relation. For that reason, it is convened that in the final version the ZFOURGE catalog a hybrid SFR version will be used, which will be composed of the SED fitted SFR for those galaxies with $\mathrm{S/N}_{24,100,160} < 3$, and the SFR_{UVIR} for those sources detected in the same bands.

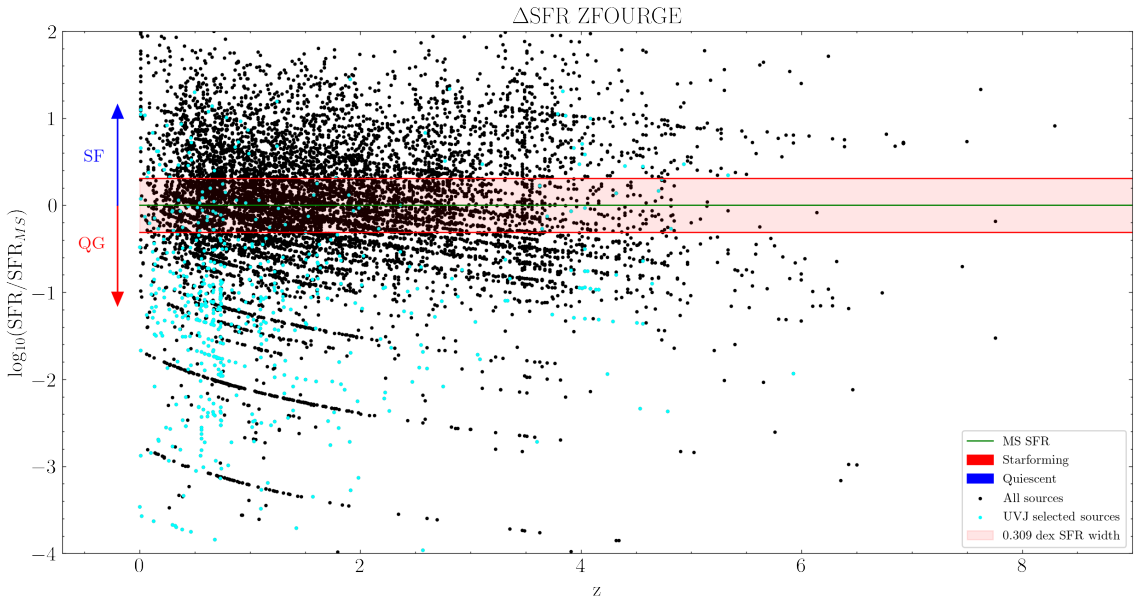

Figure 3.16: Scatter plot of ΔMS vs redshift. The green line represents the SFR of the main sequence calculated with equation 1.5. The red upper and lower boundaries represent the 0.3 dex dispersion of the main sequence below which sources can star to be considered quiescent or ongoing quenching. In cyan we can see the galaxies identified as quiescent with the UVJ selection criterion.

Figure 3.16 shows how the use of SFR_{UVIR} as an estimator makes the scatter more homogeneous, instead of the noticeable layering that occurred in Figure 3.15a, due to the

constraints of the used galaxy models. This stratification is also present with the new hybrid SFR, but to a lesser degree.

Having carried an extensive analysis on the properties of the ZFOURGE survey, having compared it with a personally made EAZY catalog and applied a series of robustness checks, the ultimate catalog contains a total of 10755 galaxies, of which 781 are considered quiescent according to the UVJ selection criterion. The redshifts are a mixture of spectroscopic measurements provided by ZFOURGE and additional external compilations as well as EAZY photometric estimates. A hybrid SFR is also used, which takes SFR_{UVIR} (eq. (3.2)) for sources with a S/N > 3 in the 24, 100 and 160 μm filters. We also account for the K band magnitude as well as the separation to the closest ALMA detected star forming source. This catalog will be the one used to make stacked images and obtain flux measurements.

Chapter 4

Results

As it is explained in subsection 2.2.1, the stacking software requires an input catalog, described in chapter 3 and a galaxy selection. Among the different selection criteria that are used, there is a common set of constraints. First is that the maximum K band magnitude is limited to 25, in order to ensure that the SED fits have been performed correctly and their stellar population parameters are more reliable. The other is a minimum separation from the closest ALMA detected SF galaxy of 1 arcsecond.

Optimally, the stacked image should be comprised of very massive quiescent galaxies and at the highest redshift possible. The higher the stellar mass is the higher its gas mass is assumed to be, and therefore easier to observe. The majority of gas fraction measurements across cosmic times have also been extracted from very massive galaxies or populations [Magdis et al., 2021; Gobat et al., 2020; Williams et al., 2021]. Concerning redshift, as it was explained in chapter 1, the higher it is the less time it offers to the observed quiescent galaxy to have evolved since it underwent quenching. At lower redshifts it becomes harder to descry whether the galaxy has recently been quenched or if it has been passively evolving. The drawback that prevents from making such a selection is the low amount of massive quiescent galaxies that are found at z > 2, which by themselves are not enough to give a compelling and reliable stacked image and therefore, a gas detection. The task then becomes making a fine representative selection with the sufficient number of quiescent galaxies that can result in a detection.

Two different minimum stellar masses are used $10^{10} M_{\odot}$ and $10^{10.5} M_{\odot}$ as well as two different redshift ranges: $1 < z < 2$ and $1 < z < 3$. Finally we will stack QGs selected by Williams et al., 2009 UVJ method and by defining ΔMS ranges. All the selection criteria can be observed on table 4.1 below. For the selection depending on distance to the MS, instead of using $\Delta\text{MS} = \log_{10}(\text{SFR}/\text{SFR}_{MS})$ the linear $\delta\text{MS} = \text{SFR}/\text{SFR}_{MS}$ will be used.

Selection		G	<z>	σ_z	$\log_{10}(< M_{star} >)$ [$M_\odot$]	σ_{Mstar}	flux [mJy]	rms [mJy]
$1 < z < 2$; $\log_{10}(M_*/M_\odot) > 10$	$1/2 < \delta\text{MS} < 2$	106	1.44	0.28	10.49	2.78×10^{10}	0.1850	0.0283
	$1/5 < \delta\text{MS} < 1/2$	30	1.44	0.25	10.57	2.48×10^{10}	0.0740	0.0223
	$\delta\text{MS} < 1/5$	86	1.38	0.28	10.68	4.47×10^{10}	0.0092	0.0153
	UVJ selection	95	1.41	0.29	10.57	4.32×10^{10}	0.0196	0.0154
$1 < z < 2$; $\log_{10}(M_*/M_\odot) > 10.5$	$1/5 < \delta\text{MS} < 1/2$	15	1.44	0.27	10.75	2.08×10^{10}	0.1245	0.0274
	$\delta\text{MS} < 1/5$	44	1.44	0.28	10.86	5.06×10^{10}	0.0280	0.0206
	UVJ selection	52	1.42	0.27	10.84	4.81×10^{10}	0.0379	0.0179
$1 < z < 3$; $\log_{10}(M_*/M_\odot) > 10$	$1/2 < \delta\text{MS} < 2$	189	1.87	0.55	10.47	2.49×10^{10}	0.1932	0.0096
	$1/5 < \delta$MS $< 1/2$	**41**	**1.74**	**0.56**	**10.50**	**2.36×10^{10}**	**0.0893**	**0.0166**
	δMS $< 1/3$	**125**	**1.61**	**0.51**	**10.65**	**4.01×10^{10}**	**0.0382**	**0.0141**
	UVJ selection	**117**	**1.60**	**0.50**	**10.68**	**4.26×10^{10}**	**0.0302**	**0.0128**
$1 < z < 3$; $\log_{10}(M_*/M_\odot) > 10.5$	$1/5 < \delta\text{MS} < 2$	15	1.44	0.27	10.74	2.08×10^{10}	0.1245	0.0279
	$\delta\text{MS} < 1/3$	66	1.63	0.47	10.77	4.39×10^{10}	0.0473	0.0179
	UVJ selection	67	1.65	0.51	10.77	4.65×10^{10}	0.0464	0.0206

Table 4.1: Compilation of measurements extracted from the different stacked images.

G indicates the number of galaxies present in the selection. The fluxes shown in table 4.1 are calculated by placing a 1.6 arcsec diameter circular aperture on the center of the stacked image. The flux within the aperture is corrected by multiplying it by an aperture correction factor of 1.54050907. Most of the measurements shown above do not show any visible flux in their stacked images. It was decided to use the data from the selections with $M_{star} > 10^{10} M_\odot$ for they have a larger number of selected galaxies and therefore their rms is lower. The selections that are most promising, at least visually are shown in Figure 4.1 and have bold fonts in table 4.1.

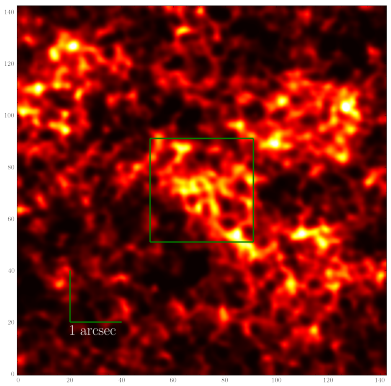

(a) 1<z<3, $\log_{10}(M_*/M_\odot)$>10, UVJ selection

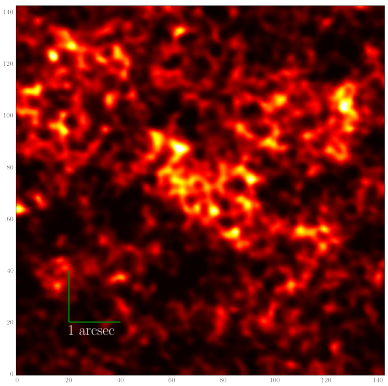

(b) 1<z<3, $\log_{10}(M_*/M_\odot)$>10, δMS $< 1/3$

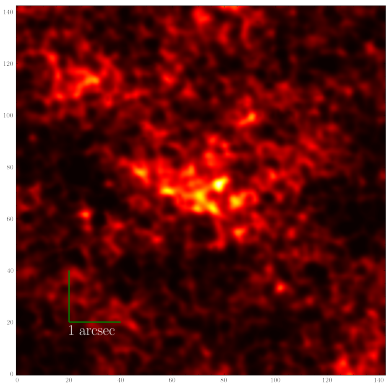

(c) 1<z<3, $\log_{10}(M_*/M_\odot)$>10, $1/5 < \delta\text{MS} < 1/2$

Figure 4.1: 7.05"×7.05" (141×141 pixel) stacked cutouts of the highlighted selections in table 4.1, using images from GOODS-ALMA survey of galaxies selected from the ZFOURGE catalog.

These three stacks are selected to be followed up by gas and dust mass calculations. One of them (Figure 4.1a and 4.1c) have a S/N > 3, whereas the other are calculated as 3σ upper limits. In the images' center a faint flux emission can be observed, especially in Figure 4.1c. Taking their flux measurements, or 3σ upper limits, the calculation of a gas/dust mass can be done. Two different approaches will be used. The first will be based on the QG FIR template described in Magdis et al., 2021. The template is created taking photometric measurements of 3 stacked ensembles, which are mostly located around the peak of the SED and near the R-J tail. The template has a native dust mass (M^0_{dust}) of 1.11×10^8 $M_\odot$ and a native $L^0_{IR} = 10^{10}$ $L_\odot$. This two are related by the inherent luminosity to dust ratio of the model $L^0_{IR}/M^0_{dust} = 90$ $L_\odot/M_\odot$. The dust temperature associated with the template is of 28deg K. The aim is to adjust the FIR template to the flux measured from the GOODS-ALMA stack and scale it, therefore obtaining a new M_{dust} that can be converted to M_{gas} with the δ_{GDR} coefficient. Given that N = L_{IR}/L^0_{IR}, then we can use Magdis et al., 2021 to calculate f_{gas}:

$$f_{gas} = \frac{N \times GDR(Z) \times M^0_{dust}}{M_{star}} \tag{4.1}$$

Where GDR(Z) is the gas to dust ratio coefficient, which adopting a universal solar metallicity corresponds to GDR($Z_\odot$)=92. M_dust and L_{IR} are calculated by multiplying the native values of the model by the scaling factor N. Considering that the FIR template has rest frame L_ν values $[ergs{\cdot}Hz^{-1}{\cdot}s^{-1}]$ and the fluxes extracted from the GOODS-ALMA map are in mJy, the scaling factor between the model and our measurements can be computed with the following calculations. Equation 4.2 is used to find the rest wavelength of each stack image flux, calculated with mean redshift of the stack selection.

$$\lambda_{rest} = \frac{1100[\mu\text{m}]}{1 + \langle z \rangle} \tag{4.2}$$

$$f_\nu \ [ergs{\cdot}Hz^{-1}{\cdot}s^{-1}{\cdot}cm^{-2}] = 10^{23} \times f \ [\text{Jy}] \tag{4.3}$$

$$L_{\nu,measured} = 4 f_\nu {\cdot} \pi {\cdot} d_L^2 \tag{4.4}$$

After converting the measured flux in mJy to f_{nu} (with eq. (4.3)), the latter can be converted to luminosity using equation 4.4, in which d_L represents the luminosity distance computed with the cosmological parameters described in chapter 2 since $d_L \propto \langle z \rangle$. Finally the scaling factor is calculated as:

$$N = \frac{L_{\nu,measured}}{L_{\nu,model}} \tag{4.5}$$

The uncertainty in the f_{gas} estimate is calculated by:

$$\sigma_{fgas} = \sqrt{\left(\frac{\sigma_f}{f}\right)^2 + \left(\frac{\sigma_{Mstar}}{\sqrt{G}\langle M_{star} \rangle}\right)^2} \tag{4.6}$$

Where f and σ_f are the GOODS-ALMA measured flux and rms respectively. For a given stack ensemble f_{gas} measurement, its value depends on N and the native dust mass of the template M^0_{dust}. Apart from the QG FIR template, another three FIR templates are taken to use as a comparison. The three of them are MS galaxy templates each with a higher dust temperature T_d, and therefore a higher L^0_{IR}/M^0_{dust} relation. All four templates are normalized to a native infrared luminosity of $10^{10} L_\odot$ and their luminosity to dust ratios are, in increasing order: 90, 384, 1530 and 3184 $L_\odot/M_\odot$. The higher the ratio is, or the

hotter the dust temperature of the template is, which is considered constant for each, template the lower f_{gas} it will compute for a given luminosity. The difference in measured f_{gas} can be seen in figure 4.2.

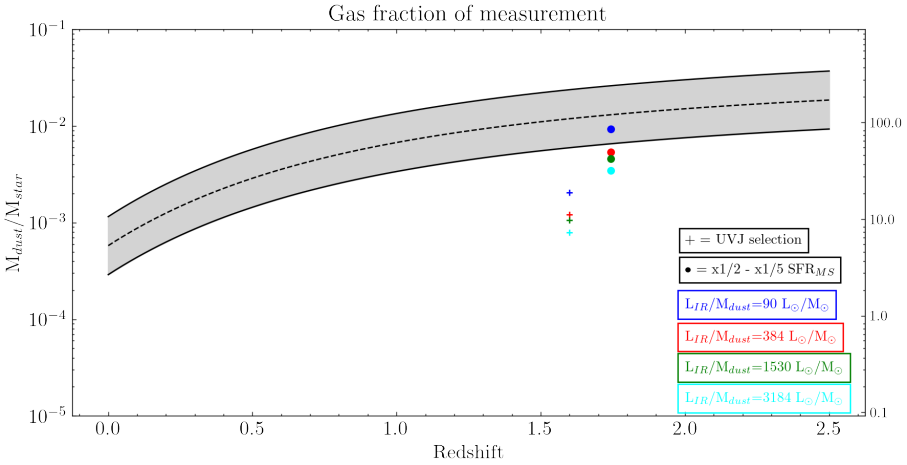

Figure 4.2: f_{gas} measurements calculated with different FIR templates for our two GOODS-ALMA 3σ detections. The grade shaded area represents the MS computed with [Liu et al., 2019] $f_{gas,MS}$ model.

It is seen, that as expected, the models with the warmest T_d, i.e larger L_{IR}/M_{dust}, have the smaller f_{gas} estimates. As a robustness check for these measurements, we compute the minimum measurable f_{gas} from the GOODS-ALMA map, and then the same is done for the stacked image, whose rms $\propto (\sqrt{G})^{-1}$ and thus is reduced, which allows to obtain 3σ detections with a smaller flux. The δMS $< 1/3$ selected stack (M_{star} >10 and 1<z<3) is used as a test. In Figure 4.3 first we see that the minimum measurable f_{gas} decreases with M_{star}. This is due to the fact that the measured M_{gas} is constant for a determined luminosity, but the gas fraction decreases proportionally as M_{star} increases. We take the GOODS-ALMA map rms value from [Goméz-Guijarro et al., in prep], which has a value of σ_{map}=68.4 μJy/beam. Using a $3sigma_{map}$ value as an upper limit, the correspondent f_{gas} is calculated, which evolves as a function of M_{star}. Then the analogous process is carried out with the rms of the stacked image which has a value of $\sigma_{stack}=\sigma_{map}/\sqrt{G}$. A lower rms value allows for lower gas measurements. Figure 4.3 reveals that the f_{gas} measurement complies with the minimum observable f_{gas}. The same robustness check is run with the other two chosen measurements and their results are equally satisfactory.

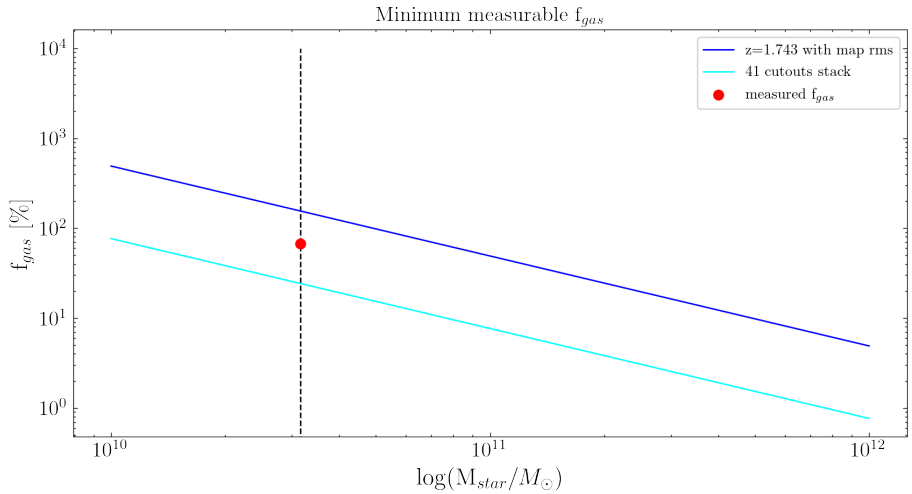

Figure 4.3: Plot showing the minimum measurable f_{gas} using the rms of the GOODS-ALMA map (in blue) and the stacked image (in cyan). The red circle represent the actual measured f_gas from the $1/5 < \delta\text{MS} < 1/2$ selected stack image and the black vertical dashed line marks the $\langle M_{star} \rangle$ of the stack subsample.

The second f_{gas} measure method is based on [Scoville et al., 2016], which uses a single flux measurement in the R-J tail to make an M_{gas} estimation. The reason for this is that warmer dust has a much higher emission than the colder one at shorter wavelengths, but correspond to less than 10% of the total M_{dust} [Liu et al., 2019]. Colder dust, which then amounts to most of the M_{dust} can be approximated with a single observation in the R-J tail. It is formulated as:

$$M_{mol} = 1.78\, S_{\nu,obs}\,[\text{mJy}]\,(1+z)^{-4.8} \times \left(\frac{\nu_{850\mu m}}{\nu_{obs}}\right)^{3.8} (d_L[\text{Gpc}])^2 \times \left\{\frac{6.7\times10^{19}}{\alpha_{850}}\right\} \frac{\Gamma_0}{\Gamma_{RJ}}\ 10^{10}\ M_\odot \tag{4.7}$$

The formula is requires the flux measurements to have a rest wavelength of λ_{rest} >250μm, which all our measurements fulfill. $S_{\nu,obs}$ is the observed flux density, $\nu_{850\mu m}$ is the correspondent frequency to λ=850μm and ν_{obs} is the correspondent frequency of the wavelength of the observation, in this case 1.1 mm. d_L is the luminosity distance, which is calculated as a function of redshift. Next, α_{850} is the luminosity to mass ratio of obtained from Planck data in Taurus [Scoville et al., 2016], such that α_{850}=6.2×10^{19} erg s^{-1} Hz^{-1} M$_\odot^{-1}$. Finally Γ_{RJ} represents the correction for departure in the rest frame of the Planck function from Rayleigh-Jeans:

$$\Gamma_{RJ}(T_d, \nu_{obs}, z) = \frac{h\nu_{obs}(1+z)/kT_d}{\exp h\nu_{obs}(1+z)/kT_d - 1} \tag{4.8}$$

Where h and k are the Planck and Boltzmann constants respectively. Γ_0 represents the value taken by equation 4.8 when z=0, T_d = 25 K and λ=850μm which is 0.71. Approximating M_{mol} to M_{gas} we have a set of f_{gas} estimations of our selected stack images through three different approaches:

1. Scaling of QG FIR template [Magdis et al., 2021]
2. Scalation of MS FIR template [Magdis, 2012]
3. Use of flux density in R-J tail with [Scoville et al., 2016] model.

Selection		$f_{gas,1}$ [%]	$\mathrm{SFR}_{UV+IR,1}$	$\tau_{dep,1}$	$f_{gas,2}$ [%]	$\mathrm{SFR}_{UV+IR,2}$	$\tau_{dep,2}$	$f_{gas,3}$ [%]
$1 < z < 3$; $M_*/M_\odot > 10$	$1/5 < \delta\mathrm{MS} < 1/2$	67.5 ± 14.8	5.2	4.1	39.3 ± 8.6	10.9	1.3	30.9 ± 5.7
	$\delta\mathrm{MS} < 1/3$ (3σ upper limit)	22.3	2.7	3.7	13.2	5.4	1.1	10.4
	UVJ selection (3σ upper limit)	18.8	2.3	3.8	13.4	4.9	1.1	10.6

Table 4.2: Collection of f_{gas} estimates for the selected stack ensembles.

The SFR_{UV+IR} values are in $M_\odot/yr$ and τ_{dep} are in Gyr and find that the values obtained with the QG FIR template comply with previously presented values in [Magdis et al., 2021]. In order to assess the obtained results they are compared to the f_{gas} evolution plot found in [Gobat et al., 2020], which collects a large number of f_{gas} measurements for quiescent galaxies across cosmic times. The $f_{gas,MS}$ is modelled with [Liu et al., 2019] characterization:

$$\begin{aligned} log_{10}(f_{gas}) = &(a + ak \times log_{10}(M_{star}/10^{10})) \times \Delta MS \\ &+ b \times log_{10}(M_{star}/10^{10}) \\ &+ (c + ck \times log_{10}(M_{star}/10^{10})) \times t_{cosmicage} \\ &+ d \end{aligned}$$

which takes the following values: a=0.4195,ak=0.1195,b=-0.6906,c=-0.1543,ck=0.0320, d=0.9339.

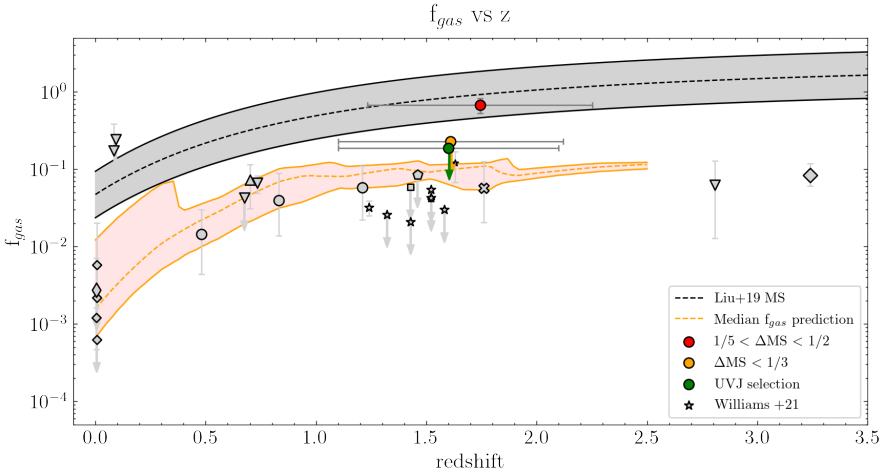

(a) f_{gas} estimations obtained with **quiescent FIR template**

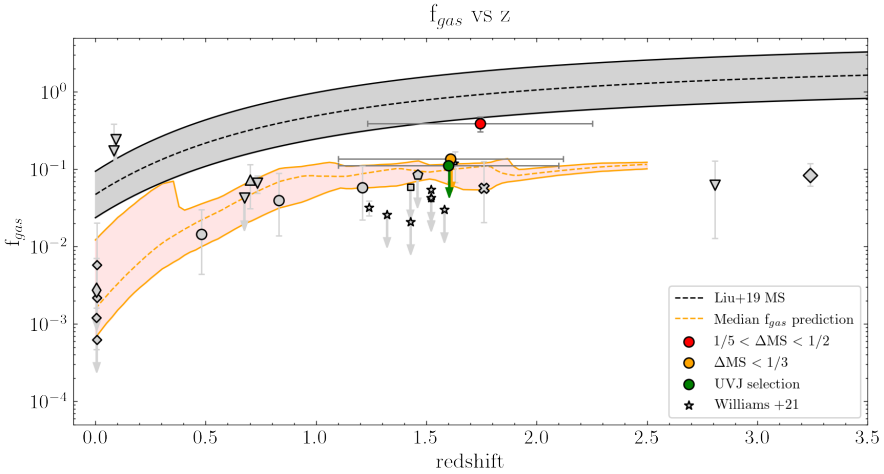

(b) f_{gas} estimations obtained with **main sequence FIR template**

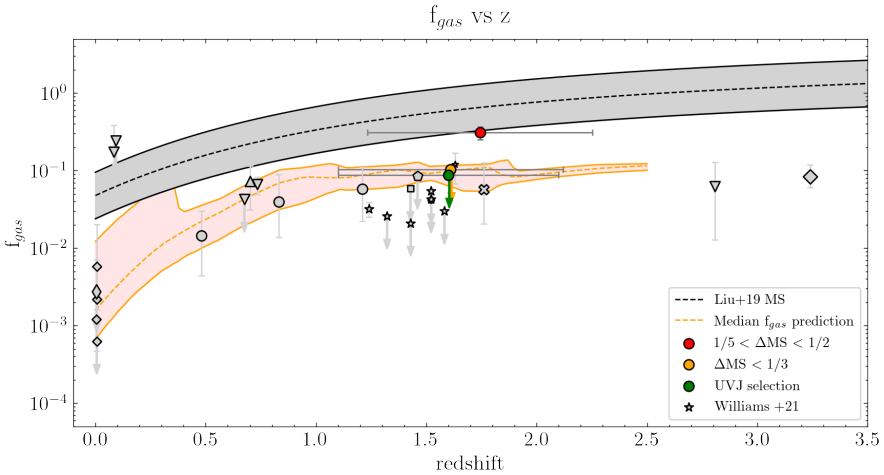

(c) f_{gas} estimations obtained with **R-J tail dust mass estimation [Scoville et al., 2016]**

Figure 4.4: f_{gas} vs z evolution plot. The measurements are shown in red, orange and green; representing the $1/5 < \delta\text{MS} < 1/2$ detection, $\delta\text{MS} < 1/3$ upper limits and UVJ selection upper limits respectively. The grey shaded area represents the f_{gas} of the MS [Liu et al., 2019] calculated with a $M_{star} = 5{\times}10^{10} M_{\odot}$ and the orange shaded area represents the f_{gas} evolution estimation for QGs from [Magdis, 2012]. The grey data points show the estimated f_{gas} of various studies, check 1.8.

We observe that the three measurements are located below or partially below the main sequence (see table 4.2). The highest gas fractions correspond to the estimates obtained from the quiescent FIR SED template, which corresponds to the model with the coldest dust temperature of the two. When calculating f_{gas} with the main sequence template, which has a warmer dust temperature, and a higher light to dust ratio, lower gas fractions are obtained. The final measurements, obtained with [Scoville et al., 2016] M_{gas} calculation method, are the lowest of the three scenarios. As a rule we observe that, independently of the f_{gas} calculation method or type of FIR template used, the estimated f_{gas} is below the main sequence for the three stacked ensembles. The three different estimations for each ensemble are combined in Figure 4.5, in which for each stack an error bar is plotted, covering an f_{gas} range that goes from the minimum to the maximum f_{gas} estimation depending on the method used.

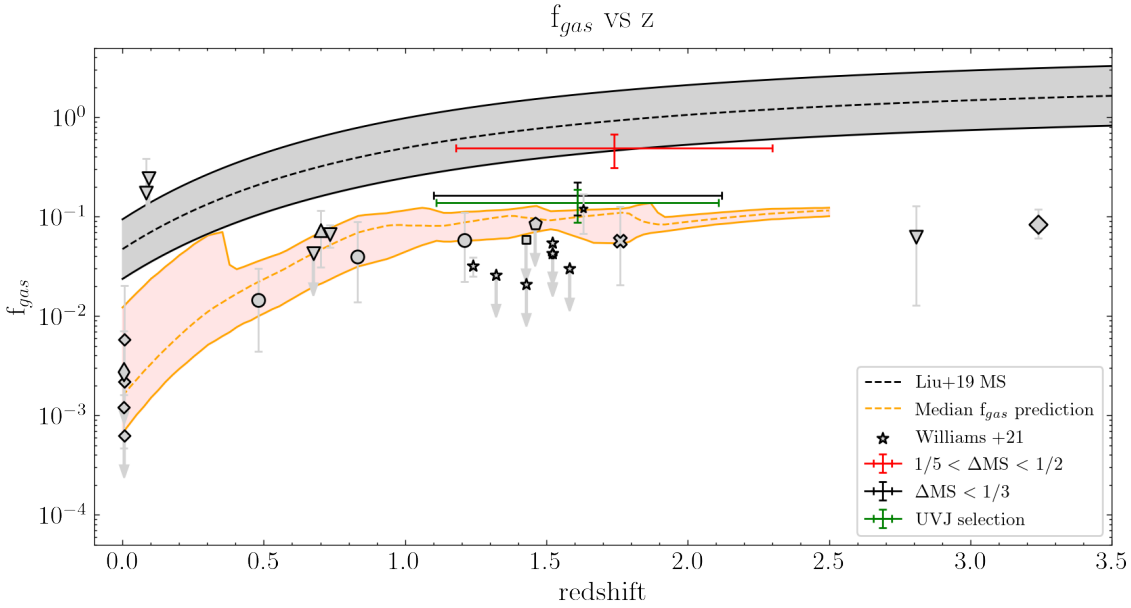

Figure 4.5: f_{gas} vs z plot with f_{gas} estimations of selected stack ensembles. The measurements are plotted as a vertical range, covering from the minimum to the maximum calculated gas fraction according to the calculation method used. The *green* and *black* ranges correspond to the upper limits of the (δMS<1/3 and UVJ selection stacks) and the *red* range corresponds to the 1/5< δMS<1/2 detection. The grey data points show the estimated f_{gas} of various studies (check 1.8) and the grey shaded area represents the predicted f_{gas} for the MS [Liu et al., 2019].

Chapter 5

Discussion

Out of the 13 stacked subsamples, only three showed promising fluxes in their images. In Figure 4.1c, we can see a clear detection, with the flux concentrated around the center of the image and no noise spikes nearby. The fact that we are able to see clumps of emission might be due to the GOODS-ALMA map high resolution, since when producing the analogous image with the low resolution version, a round, smoothed flux appears. The other two stacked subsamples, Figures 4.1a and 4.1b, have larger noise amounts polluting the fluxes that can be discerned at their centers. The S/N ratios of the measured fluxes, with a placed aperture of 1.6 arcsec diameter are of 2.7 for Figure 4.1b and 2.3 for Figure 4.1a. The high amount of noise that we observe might be due to a very bright galaxy near to a selected QG that biases the stack. However, the fact that we discard galaxies that have an ALMA detected SF galaxy closer than 1 arcsecond should act as a partial barrier for that issue. Taking all of this into account, their f_{gas} are calculated as 3σ upper limits. It must be considered that a selection concerning 24μm fluxes is not made, this is, discarding sources that are bright in the FIR since it might be a signature of AGN activity and thus could be biasing the stack. It is still unsure whether a bright 24μm detection comes from AGN activity or if it is a product of old stellar populations, which are characteristic of quiescent galaxies. As a robustness check, we compare the calculated τ_{dep} obtained through the SFR_{UVIR} estimates with the ones obtained through QG stacked ensembles at with solar metallicity (GDR=92). The values of our fully quiescent stacked ensembles which have a $\tau_{dep} \approx 3.7$ Gyr similar to the ≈ 3.4 Gyr obtained by Magdis et al., 2021 (Note that the SFR values have been transformed from their original Salpeter IMF value to Chabrier IMF by dividing τ_{dep} by a factor of 1.7, in order to be compared with our estimates).

Another property that arises concern is the large redshift range that is being used in the stack subsamples. However, the fact that the FIR part of the SED of quiescent galaxies does not evolve with redshift together with the shape of the R-J tail, allow for a "negative K correction". Due to the negative steep slope of the R-J tail, the higher the probed redshift is, the smaller its rest frame wavelength it will be, which will correspond to a higher FIR flux as a result of the shape of the SED. Therefore the cosmological dimming occurring by an increase in redshift (and therefore an increase in distance) is canceled out with the brightening of its rest frame flux. This negative K correction is the phenomenon allowing to stack sources with such different redshifts, since they all have similar fluxes in the GOODS-ALMA map.

From the three available MS models, it was decided to use the one with the coldest dust temperature and lowest luminosity to dust ratio ($L_{IR}/M_{dust} = 384\ L_{\odot}/M_{\odot}$) as

representative of the MS. The difference of estimated f_{gas} of the different main sequence models can be seen in Figure 4.2.Even though the δ_{GDR} method obtains a measurement of the mass of all the gas, this can be approximated to M_{H2} taking into account the M_{HI}/M_{H2} measured for local quiescent galaxies. This observation is extended to high redshift quiescent galaxies and therefore the measured f_{gas} can be interpreted as f_{H2}. It must be noted that the mean M_{star} of our stacked ensembles is lower than the M_{star} of individually observed galaxies or stack samples used for f_{gas} estimations in Figures 1.8,1.9, which range from 1010.8 to $10^{11.6} M_{\odot}$. Looking at Figure 4.5, from a broad viewpoint, we see that the obtained estimations follow the general trend, this being that QGs seemingly have lower gas fractions that main sequence galaxies. The $1/5 < \delta\text{MS} < 1/2$ subsample results in a higher f_{gas} estimate. The fact that the ensemble select sources that are much closer to the main sequence means that those galaxies are not necessarily quiescent yet, but might be undergoing quenching. The obtained f_{gas} measurement range from 67.54±14.84 % to 30.86±5.75, both of which are below the main sequence, but not as low as the QG subsample f_{gas}, i.e. the range of gas fractions that could be expected of galaxies that are becoming quenched. The quiescent subsamples (UVJ selection and $1/3\ \delta\text{MS} < 1/3$) upper limits, which range from 18.8 to 10.6 % and 22.3 to 10.4 % respectively, are not precise enough to give any conclusive information. A robust detection would be required in order to obtain a compelling and reliable f_{gas} estimate. The fact that the quiescent subsamples recover a 2.3 and 2.7 σ detections encourages to make an attempt on recovering a sound signal with the proper data treatment, such as uv stacking [Lindroos et al., 2014].

Our obtained results verify the previously drawn picture that local QGs have lower f_{gas} and therefore smaller gas reservoirs than high redshift QGs. However they can not place any further constraints on the evolution of f_{gas} with cosmic time and on the possible quenching mechanisms. The results shown by [Williams et al., 2021], if we consider them representative of the quiescent population, demonstrate that massive QGs at z > 1 have very low amounts of gas after being quenched, thus indicating the effectiveness of the processes that either dispel or consume cool gas. These results do not comply with previous f_{gas} estimates obtained through stacked images [Gobat et al., 2018; Magdis et al., 2017], which estimate an $f_{gas} \sim 16\%$. These contrasting results could be the consequence of a large heterogeneity in the population of quiescent galaxies, which would mirror the diversity of quenching processes. We will now see how different f_{gas} estimates result in different τ_{dep} and greater or lesser evolution of the gas reservoirs in QGs.

A scenario with very low f_{gas}, resembling [Williams et al., 2021], results is the result of a very fast consumption of the gas reservoir and the disruption of gas accretion on to the galaxy. The earlier the accretion is stopped, the more time the galaxy will have to consume its gas and reach the observed f_{gas}. Observations resemble a picture in which galaxies halt their accretion at z > 3.5 and then consume their remaining gas with $\tau_{dep} <$ 0.6 Gyr, common of star forming MS galaxies. On the other hand, an scenario with higher f_{gas} estimates (> 16%), result in a difference of two orders of magnitude between local and high redshift QGs. Hydrodynamical simulations on the evolution of quiescent galaxies propose that SFE drop by a factor of 5-10 once the gas fraction falls below a determined value $f_{gas} \sim 25\%$ [Magdis et al., 2017]. Therefore the halt of star formation activity does not necessarily imply the expulsion of consumption of all the entire gas reservoirs. The lower f_{gas} of local quiescent galaxies can then be explained by the passive evolution of these not star forming efficient galaxies. However in order to keep f_{gas} below its critical value, another mechanism must appear in order to account for the new gas that is accreted on to the galaxies through mergers and cosmic gas filaments. Three possible scenarios are then proposed: very massive halos ($>10^{13} M_{\odot}$) that hold hot atmospheres, preventing the

accretion of cold gas; AGNi feedback which can heat up and dispel the cold gas and finally, gas heating by gravitational interactions. The picture of f_{gas} evolution then remains yet unsolved, however the project has given promising results that with a more sophisticate analysis and data processing might clarify the diverse and complex phenomenology of galaxy quenching.

5.1 Caveats

The stacking method followed in this project, as well as the selected subsamples pose a number of limitations to the obtained results and the performed analysis. The first is the narrow constraints placed on the produced galaxy subsamples. The mean stellar mass of our selected stack ensembles range from $10^{10.50} M_{\odot}$ to $10^{10.68} M_{\odot}$, is lightly smaller than the average M_{star} of the stacked ensembles used to obtain f_{gas} estimations in 1.8 which were of $\approx 10^{10.8} M_{\odot}$. A higher limit on the minimum M_{star} of the subsample would be desirable. However, the number of galaxies in the stack necessary to obtain a robust image is also affected by imposing a higher minimum M_{star}. We also acknowledge that the constructed ΔMS relies on SFR obtained through template SED fitting, which can not be taken as a true measure of the SFR but as an estimation and on SFR_{UVIR}. The latter is approximated from L_{IR} and L_{UV} which are themselves calculated from fitted templates to the IR and UV photometric data, which we found not to be very sound in most of the cases, with 85 % of the galaxies not having a S/N > 3 in the Spitzer/Herschel bands. Further, the fact that we are not applying any cuts according to the 24 μm emission of galaxies might mean that flux coming from AGN activity and star forming galaxies is biasing the stacked images flux.

There is also a need to have a closer investigation of the templates used by EAZY since their SFR derivation is still in a exploratory phase. Finally two of the three selected catalog subsamples have doubtful stacked images, showing strange morphology and large amounts of noise outside the center of the image. A more thoughtful analysis on the emission of each of the galaxies belonging to the stacks would be helpful to see whether a small amount of wrongly classified quiescent galaxies is biasing the obtained image flux. Finally the fact that we are stacking the images and not the uv-plane observations might be decreasing the S/N of the stack ensembles.

Chapter 6

Summary

This project first starts with a review of the nature of galaxies, their classes, and their evolution. From how do they start in the first place to how they evolve, and their components with them. It is acknowledged that galaxies can be classified according to the amount of stars they form, and can either be star forming or quiescent. The fact that we observe that the SFR density of the universe peaked at z$\sim$2, and has decreased ever since and the observation of quiescent galaxies to such early times (z$\sim$4 or $t_{lookback} \sim 11.5$ Gyr) has shifted the attention of some part of the scientific community to understand why do galaxies quench and through what physical processes do they become quiescent. How can it be that quiescent galaxies exist at such early times in the universe?

A large number of mechanisms have been proposed and the common feature among all of the is cooled gas, i.e. the fuel for star formation. It is found that all the possible physical processes involve, in many different ways, the incapability of a galaxy to accrete mass, to cool it down and allow the formation of stars or to eject it from the galaxy. Another possible scenario is the one in which a galaxy, due to a sudden burst of star formation, which could be triggered by a major merger followed by a compaction event, in which the remaining gas can be rapidly consumed. Studying the remaining gas in quiescent galaxies can shine some light on whether is the lack of gas the phenomenon triggering quiescence, or whether if it is due to another mechanism. Making an analysis on the evolution of the gas mass can also show whether the gas fraction in QGs has changed with cosmic time, or if galaxies in the past are getting quenched for the same reason they are getting quenched now. The study of gas in quiescent galaxies across cosmic time is a relatively new field. The measurements carried out until now show that QGs apparently have smaller f_{gas} than the main sequence of galaxies at their correspondent redshift and that quiescent galaxies had higher gas masses in the past than they do today. However, some these values have been obtained by studying individual sources, whose results suffer from selection biases, this is, the fact that an individual source can not be representative of the average population. Other measurements have been carried out by stacking of FIR images, which allow to reach depths not attainable by usual telescope images. These subsamples of galaxies, when stacked, lower the rms of the individual image and can statistically obtain compelling data. The issue is the fact that this stacked images have been obtained with surveys of low angular resolution, and thus suffer from blending caveats. The scope of the project then was to select an average population of quiescent galaxies at high redshift and stack their emission from the recently produced GOODS-ALMA 2.0 1.1 mm survey [Gómez-Guijarro et al.,in prep], which reaches a very high angular resolution of 0.447"$\times$0.418" and a sensitivity of 68.4μJy/beam. The fact that

this GOODS-ALMA survey is located at GOODS-South, the most studied field in the sky brings an opportunity to select a large enough number of high redshift quiescent galaxies to obtain a compelling observation of their FIR continuum properties, and analyse their ISM.

To do so the ZFOURGE catalog built by [Straatman et al., 2016] was selected, containing 30911 galaxies. An analysis of its main properties was carried out, stellar mass, SFR, redshift distribution, sSFR estimates etc. A quiescent galaxy selection was done through the UVJ color-color diagram [Williams et al., 2009]. An unexpectedly large number of low mass quiescent galaxies, well below the $10^8 M_\odot$ mass completeness limit, were detected. This finding led us to revisit the SED fittings that the FAST software had performed, and from which stellar population parameters are extracted. It was then observed that even if most of the fits were properly performed, a not negligible amount of them were catastrophic. The fact that some of this catastrophic SED fits were identified as quiescent galaxies led to the creation of a secondary catalog, using EAZY to fit galaxy templates to the photometric data provided by ZFOURGE and observe whether there were any major changes. The Spitzer/MIPS 24μm filter was introduced in the SED fitting process to assess its effect on the obtained stellar population parameters, even though no major changes were detected. A UVJ selection criteria was also applied to this EAZY catalog to identify and flag quiescent sources.

The comparison between the EAZY built and ZFOURGE catalogs was restricted to those galaxies that were within the GOODS-ALMA 2.0 survey footprint, at a small distance from the less sensitive edges of the map, which accounted to ≈10000 galaxies out of the original 30911 sources included in the CDFS part of the ZFOURGE catalog. There is an agreement between the redshift and SFR distributions. It is not the case for the stellar masses, where an appreciable offset could be observed. This difference was even more visible when comparing the $\Delta\text{MS} = \log_{10}(\text{SFR}/\text{SFR}_{MS})$ vs z plots of the two catalogs. For both of them, the main population of UVJ selected sources were found below the main sequence values. The issue arose in the EAZY catalog plot, where the bulk of the sources was not within the main sequence region (represented by a 0.309 *dex* dispersion). Where, by definition, is the place were the majority of galaxies is expected to be. This finding, led to the discard of the EAZY built catalog due to the time constraints imposed on the project, which would not allow a deeper analysis on the intricacies of the software. Then using the ZFOURGE catalog the stack ensembles were defined and their GOODS-ALMA cutouts stacked. All galaxy subsamples shared the following criteria: $K_{MAG} < 25$, which got rid of all catastrophic SED fits and a minimum distance from the closest ALMA detected SFG of 1 arcsecond. Together with that criterion, different redshift ranges were defined and minimum M_{star} were established. The most promising ensembles were all extracted from a $1 < \text{z} < 3$ redshift range and a minimum stellar mass of $10^{10} M_\odot$. The quiescence of the stacked ensembles was defined either by UVJ selection or $\delta\text{MS} < 1/3$ (where $\delta\text{MS} = \text{SFR}/\text{SFR}_{MS}$). The most clear detection came from the $1/5 < \delta\text{MS} < 1/2$ stacked ensemble, whereas the other two showed considerable amounts of noise and didn't record a 3σ detection, and were thus treated as upper limits.

The calculation of their gas masses or gas fractions was carried out by using the obtained fluxes as rest frame measurements of the R-J tail which were in turn used to scale previously built FIR templates (with a native dust mass and infrared luminosity). Then using a δ_{GDR} conversion factor assuming solar metallicity, the dust mass measurements obtained from the templates was converted to a gas mass. Two different FIR templates were used, one representing a quiescent galaxy and another representative of a main sequence galaxy, with a higher light to dust mass ratio. As a third estimation method, the obtained fluxes

were used to calculate M_{gas} following the calculation described in Scoville et al., 2016. This latter method resulted in the lowest f_{gas} estimations of the two and the QG FIR template gave the highest f_{gas} measurements. However all three estimations coincide and comply with previous gas studies in that quiescent galaxies seem to have a lower gas fraction that main sequence sources at their correspondent redshifts. The two most quiescent selections, obtained an upper limit f_{gas} estimations that ranged from 22% to 9%, depending on the method used to derive f_{gas}. Both upper limits though, obtained very similar f_{gas} measurements. The $1/5< \delta\text{MS} < 1/2$ ensemble derived gas fractions from 67.5±14.8 % to 30.9±5.7%. These latter estimations, comply with the fact that the galaxies selected in this subsample might be undergoing quenching, but are not fully quenched yet, and thus have higher gas fractions than the quiescent stack ensembles, but below the estimated values for main sequence galaxies. The two upper limits, offer non conclusive results but promising S/N, leading to the conclusion that under the proper data processing, a detection might be obtained which allows to place further constraints on the f_{gas} and M_{dust} of high z QGs and understand the nature of the mechanisms that quenched them.

6.1 Future work

This project lays a number of paths to follow in order to extend and improve the current analysis, obtain more precise results and therefore place more robust constraints on the evolution of gas and its implications.

1. Stacking in the uv-plane to improve the robustness of the obtained images, and improve the S/N of some of the ensembles with hope of obtaining a 3σ detection
2. Use the IRAM/GISMO 2mm survey in the COSMOS field, to carry out a similar analysis and complement the obtained results.
3. Use different subsamples to obtain stack images or analyse the used ones in search of a possible flux bias, coming, for instance from 24μm bright galaxies. Use different quiescent identification methods ($NUVrK$ color color diagram [Ilbert, O. et al., 2013]).
4. Make a deep analysis on the functioning of EAZY and understand the reason for the non satisfactory obtained results.

Bibliography

Ryden, Barbara (2006). *Introduction to Cosmology*.

Abraham, R.G. (1998). "Perspectives in Physical Morphology". In: DOI: astro-ph/9809131.

Mo et al., H. (2010). *Galaxy formation and evolution*. ISBN: 978-0-511-72962-1.

Helmi et al., A. (1999). "Building up the stellar halo of the Galaxy". In:

Tully et al., R. (1992). "Luminosity–Line Width Relations and the Extragalactic Distance Scale. I. Absolute Calibration". In: *The Astrophysical Journal* 387, p. 47. DOI: 10.1086/171059.

Peletier et al., R.F. (1990). "CCD Surface Photometry of Galaxies with Dynamical Data. II. UBR Photometry of 39 Elliptical Galaxies". In: *A&A* 100, p. 1091. DOI: 10.1086/115582.

Young, J. S. and N. Z. Scoville (1991). "Molecular Gas in Galaxies". In: *Annual Review of Astronomy and Astrophysics* 29.1, pp. 581–625. DOI: 10.1146/annurev.aa.29.090191.003053.

Mathis, J. S., W. Rumpl, and K. H. Nordsieck (1977). "The size distribution of interstellar grains." In: *The Astrophysical Journal* 217, pp. 425–433. DOI: 10.1086/155591.

Leger, A. and J. L. Puget (1984). "Identification of the "unidentified" IR emission features of interstellar dust ?" In: *The Astrophysical Journal* 500, pp. 279–282.

Cimatti, Andrea (2003). "Galaxy evolution in the K-band". In: *Memorie della Societa Astronomica Italiana Supplementi* 3, p. 167.

Toft, S. et al. (2005). "Distant Red Galaxies in the Hubble Ultra Deep Field". In: *The Astrophysical Journal* 624.1, pp. L9–L12. DOI: 10.1086/430346. URL: https://doi.org/10.1086/430346.

Gobat, R. et al. (2012). "The Early Early Type: Discovery of a Passive Galaxy at z spec $\sim$ 3". In: *The Astrophysical Journal* 759.2, p. L44. DOI: 10.1088/2041-8205/759/2/l44. URL: https://doi.org/10.1088/2041-8205/759/2/l44.

Whitaker, Katherine E. et al. (2013). "Quiescent Galaxies in the 3D-HST Survey: Spectroscopic confirmation of a Large Number of Galaxies with Relatively Old Stellar Populations at z $\sim$ 2". In: *The Astrophysical Journal* 770.2, p. L39. DOI: 10.1088/2041-8205/770/2/l39. URL: https://doi.org/10.1088/2041-8205/770/2/l39.

Valentino, Francesco et al. (2020). "Quiescent Galaxies 1.5 Billion Years after the Big Bang and Their Progenitors". In: *The Astrophysical Journal* 889.2, p. 93. DOI: 10.3847/1538-4357/ab64dc. URL: https://doi.org/10.3847/1538-4357/ab64dc.

Cattaneo, A. et al. (2017). "The new semi-analytic code GalICS 2.0 – reproducing the galaxy stellar mass function and the Tully–Fisher relation simultaneously". In: *Monthly Notices of the Royal Astronomical Society* 471.2, pp. 1401–1427. ISSN: 0035-8711. DOI: 10.1093/mnras/stx1597. URL: https://doi.org/10.1093/mnras/stx1597.

Liu, Daizhong et al. (2019). "Automated Mining of the ALMA Archive in the COSMOS Field (A^{3}COSMOS). II. Cold Molecular Gas Evolution out to Redshift 6". In: *APJ* 887.2, 235, p. 235. DOI: 10.3847/1538-4357/ab578d. arXiv: 1910.12883 [astro-ph.GA].

D.M., Alexander et al. (Apr. 2005). "Rapid growth of black holes in massive star-forming galaxies". In: *Nature* 434, pp. 738–40. DOI: 10.1038/nature03473.

Fukugita, Masataka and P. J. E. Peebles (2004). "The Cosmic Energy Inventory". In: *The Astrophysical Journal* 616.2, pp. 643–668. ISSN: 1538-4357. DOI: 10.1086/425155. URL: http://dx.doi.org/10.1086/425155.

Elbaz, D. et al. (2007). "The reversal of the star formation-density relation in the distant universe". In: *AAP* 468.1, pp. 33–48. DOI: 10.1051/0004-6361:20077525. arXiv: astro-ph/0703653 [astro-ph].

Schreiber, C. et al. (2015). "The Herschel view of the dominant mode of galaxy growth from z= 4 to the present day". In: *Astronomy & Astrophysics* 575, A74. ISSN: 1432-0746. DOI: 10.1051/0004-6361/201425017. URL: http://dx.doi.org/10.1051/0004-6361/201425017.

Genzel, R. et al. (2010). "A study of the gas-star formation relation over cosmic time". In: *MNRAS* 407.4, pp. 2091–2108. DOI: 10.1111/j.1365-2966.2010.16969.x.

Man, Allison and Sirio Belli (2018). "Star formation quenching in massive galaxies". In: *Nature Astronomy* 2.9, pp. 695–697. ISSN: 2397-3366. DOI: 10.1038/s41550-018-0558-1. URL: http://dx.doi.org/10.1038/s41550-018-0558-1.

Feldmann, Robert and Lucio Mayer (2014). "The Argo simulation – I. Quenching of massive galaxies at high redshift as a result of cosmological starvation". In: *Monthly Notices of the Royal Astronomical Society* 446.2, pp. 1939–1956. ISSN: 0035-8711. DOI: 10.1093/mnras/stu2207. eprint: https://academic.oup.com/mnras/article-pdf/446/2/1939/9387050/stu2207.pdf. URL: https://doi.org/10.1093/mnras/stu2207.

Rees, M. J. and J. P. Ostriker (1977). "Cooling, dynamics and fragmentation of massive gas clouds: clues to the masses and radii of galaxies and clusters." In: *MNRAS* 179, pp. 541–559. DOI: 10.1093/mnras/179.4.541.

Cornuault, Nicolas et al. (2018). "Are cosmological gas accretion streams multiphase and turbulent?" In: *AAP* 610, A75, A75. DOI: 10.1051/0004-6361/201629229.

Tabatabaei, F. S. et al. (Nov. 2018). "Discovery of massive star formation quenching by non-thermal effects in the centre of NGC 1097". In: *Nature Astronomy* 2, pp. 83–89. DOI: 10.1038/s41550-017-0298-7. arXiv: 1710.05695 [astro-ph.GA].

Zolotov, Adi et al. (July 2015). "Compaction and quenching of high-z galaxies in cosmological simulations: blue and red nuggets". In: *MNRAS* 450.3, pp. 2327–2353. DOI: 10.1093/mnras/stv740. arXiv: 1412.4783 [astro-ph.GA].

Di Matteo, Tiziana, Volker Springel, and Lars Hernquist (Feb. 2005). "Energy input from quasars regulates the growth and activity of black holes and their host galaxies". In: *Nat* 433.7026, pp. 604–607. DOI: 10.1038/nature03335. arXiv: astro-ph/0502199 [astro-ph].

Labbé, Ivo et al. (May 2005). "IRAC Mid-Infrared Imaging of the Hubble Deep Field-South: Star Formation Histories and Stellar Masses of Red Galaxies at z>2". In: *APLJ* 624.2, pp. L81–L84. DOI: 10.1086/430700. arXiv: astro-ph/0504219 [astro-ph].

Williams, Rik J. et al. (2009). "Detection of Quiescent Galaxies in a Bicolor Sequence from Z = 0-2". In: *The Astrophysical Journal* 691.2, pp. 1879–1895. ISSN: 1538-4357. DOI: 10.1088/0004-637x/691/2/1879. URL: http://dx.doi.org/10.1088/0004-637X/691/2/1879.

Ilbert, O. et al. (2013). "Mass assembly in quiescent and star-forming galaxies since z from UltraVISTA". In: *A&A* 556, A55. DOI: 10.1051/0004-6361/201321100. URL: https://doi.org/10.1051/0004-6361/201321100.

Straatman, Caroline M. S. et al. (2016). "The FOURSTAR Galaxy Evolution Survey (ZFOURGE): Ultraviolet to Far-Infrared Catalogs, Medium-Bandwidth Photometric Redshifts with Improved Accuracy, Stellar Masses, and confirmation of Quiescent Galaxies to z 3.5". In: *The Astrophysical Journal* 830.1, p. 51. ISSN: 1538-4357. DOI: 10.3847/0004-637x/830/1/51. URL: http://dx.doi.org/10.3847/0004-637X/830/1/51.

Skelton, Rosalind E. et al. (2014). "3D-HST WFC3-Selected Photometric Catalogs in the Five CANDELS/3D-HST Fields: Photometry, Photometric Redshifts and Stellar Masses". In: *The Astrophysical Journal Supplement Series* 214.2, p. 24. ISSN: 1538-4365. DOI: 10.1088/0067-0049/214/2/24. URL: http://dx.doi.org/10.1088/0067-0049/214/2/24.

Belli, Sirio, Andrew B. Newman, and Richard S. Ellis (2019). "MOSFIRE Spectroscopy of Quiescent Galaxies at $1.5 < z < 2.5$. II. Star Formation Histories and Galaxy Quenching". In: *APJ* 874.1, 17, p. 17. DOI: 10.3847/1538-4357/ab07af. arXiv: 1810.00008 [astro-ph.GA].

Tomczak, Adam R. et al. (2016). "The SFR–M*Relation and Empirical Star Formation Histories from ZFOURGE at 0.5 <z< 4". In: *The Astrophysical Journal* 817.2, p. 118. ISSN: 1538-4357. DOI: 10.3847/0004-637x/817/2/118. URL: http://dx.doi.org/10.3847/0004-637X/817/2/118.

Gobat, R. et al. (2018). "The unexpectedly large dust and gas content of quiescent galaxies at $z > 1.4$". In: *Nature Astronomy* 2, pp. 239–246. DOI: 10.1038/s41550-017-0352-5. arXiv: 1703.02207 [astro-ph.GA].

Magdis, G. et al. (2021). "The interstellar medium of quiescent galaxies and its evolution with time". In: *AAP* 647, A33, A33. DOI: 10.1051/0004-6361/202039280. arXiv: 2101.04700 [astro-ph.GA].

Carilli, C. L. and F. Walter (2013). "Cool Gas in High-Redshift Galaxies". In: *ARAA* 51.1, pp. 105–161. DOI: 10.1146/annurev-astro-082812-140953. arXiv: 1301.0371 [astro-ph.CO].

Puglisi, A. et al. (2019). "The Main Sequence at $z \sim 1.3$ Contains a Sizable Fraction of Galaxies with Compact Star Formation Sizes: A New Population of Early Post-starbursts?" In: *APJL* 877.2, L23, p. L23. DOI: 10.3847/2041-8213/ab1f92. arXiv: 1905.02958 [astro-ph.GA].

Bourne, N. et al. (2019). "The relationship between dust and [C I] at $z = 1$ and beyond". In: *MNRAS* 482.3, pp. 3135–3161. DOI: 10.1093/mnras/sty2773. arXiv: 1810.01640 [astro-ph.GA].

Magdis, Georgios E. et al. (2012). "The Evolving Interstellar Medium of Star-forming Galaxies since $z = 2$ as Probed by Their Infrared Spectral Energy Distributions". In: *APJ* 760.1, 6, p. 6. DOI: 10.1088/0004-637X/760/1/6. arXiv: 1210.1035 [astro-ph.CO].

Jiao, Qian et al. (2017). "Neutral Carbon Emission in Luminous Infrared Galaxies: The [C I] Lines as Total Molecular Gas Tracers". In: *APJL* 840.2, L18, p. L18. DOI: 10.3847/2041-8213/aa6f0f. arXiv: 1704.07780 [astro-ph.GA].

Magdis, G. E. et al. (2017). "Dust and gas in star-forming galaxies at z 3. Extending galaxy uniformity to 11.5 billion years". In: *AAP* 603, A93, A93. DOI: 10.1051/0004-6361/201731037. arXiv: 1705.06296 [astro-ph.GA].

Dekel, A. et al. (2009). "Cold streams in early massive hot haloes as the main mode of galaxy formation". In: *Nature* 457.7228, pp. 451–454. DOI: 10.1038/nature07648. arXiv: 0808.0553 [astro-ph].

Popping, Gergö, Rachel S. Somerville, and Scott C. Trager (2014). "Evolution of the atomic and molecular gas content of galaxies". In: *Monthly Notices of the Royal Astronomical Society* 442.3, pp. 2398–2418. ISSN: 0035-8711. DOI: 10.1093/mnras/stu991. eprint: https://academic.oup.com/mnras/article-pdf/442/3/2398/3590273/stu991.pdf. URL: https://doi.org/10.1093/mnras/stu991.

Narayanan, Desika et al. (2015). "The formation of submillimetre-bright galaxies from gas infall over a billion years". In: *Nature* 525.7570, pp. 496–499. DOI: 10.1038/nature15383. arXiv: 1509.06377 [astro-ph.GA].

Tomczak, Adam R. et al. (2014). "Galaxy Stellar Mass Functions from ZFOURGE/CANDELS: An Excess of Low-mass Galaxies since z = 2 and the Rapid Buildup of Quiescent Galaxies". In: *APJ* 783.2, 85, p. 85. DOI: 10.1088/0004-637X/783/2/85. arXiv: 1309.5972 [astro-ph.CO].

Gobat, R. et al. (2020). "The evolution of the gas fraction of quiescent galaxies modeled as a consequence of their creation rate". In: *AAP* 644, L7, p. L7. DOI: 10.1051/0004-6361/202039593. arXiv: 2011.10547 [astro-ph.GA].

Williams, Christina C. et al. (2021). "ALMA Measures Rapidly Depleted Molecular Gas Reservoirs in Massive Quiescent Galaxies at z 1.5". In: *The Astrophysical Journal* 908.1, p. 54. ISSN: 1538-4357. DOI: 10.3847/1538-4357/abcbf6. URL: http://dx.doi.org/10.3847/1538-4357/abcbf6.

Grogin, Norman A. et al. (2011). "CANDELS: The Cosmic Assembly Near-infrared Deep Extragalactic Legacy Survey". In: *APJS* 197.2, 35, p. 35. DOI: 10.1088/0067-0049/197/2/35. arXiv: 1105.3753 [astro-ph.CO].

Franco, M. et al. (2018). "GOODS-ALMA: 1.1 mm galaxy survey. I. Source catalog and optically dark galaxies". In: *AAP* 620, A152, A152. DOI: 10.1051/0004-6361/201832928. arXiv: 1803.00157 [astro-ph.GA].

Franco, M. et al. (2020a). "GOODS-ALMA: The slow downfall of star formation in z = 2-3 massive galaxies". In: *AAP* 643, A30, A30. DOI: 10.1051/0004-6361/202038312. arXiv: 2005.03043 [astro-ph.GA].

Franco, M. et al. (2020b). "GOODS-ALMA: Using IRAC and VLA to probe fainter millimeter galaxies". In: *AAP* 643, A53, A53. DOI: 10.1051/0004-6361/202038310. arXiv: 2005.03040 [astro-ph.GA].

Gavazzi, G., D. Pierini, and A. Boselli (1996). "The phenomenology of disk galaxies." In: *AAP* 312, pp. 397–408.

Brammer, Gabriel B., Pieter G. van Dokkum, and Paolo Coppi (2008). "EAZY: A Fast, Public Photometric Redshift Code". In: *APJ* 686.2, pp. 1503–1513. DOI: 10.1086/591786. arXiv: 0807.1533 [astro-ph].

Kriek, Mariska et al. (2009). "An Ultra-Deep Near-Infrared Spectrum of a Compact Quiescent Galaxy at z = 2.2". In: *APJ* 700.1, pp. 221–231. DOI: 10.1088/0004-637X/700/1/221. arXiv: 0905.1692 [astro-ph.CO].

Zhou, L. et al. (2020). "GOODS-ALMA: Optically dark ALMA galaxies shed light on a cluster in formation at z = 3.5". In: *Astronomy & Astrophysics* 642, A155. ISSN: 1432-0746. DOI: 10.1051/0004-6361/202038059. URL: http://dx.doi.org/10.1051/0004-6361/202038059.

Astropy Collaboration et al. (2018). "The Astropy Project: Building an Open-science Project and Status of the v2.0 Core Package". In: *AJ* 156.3, 123, p. 123. DOI: 10.3847/1538-3881/aabc4f. arXiv: 1801.02634 [astro-ph.IM].

Virtanen, Pauli et al. (2020). "SciPy 1.0: Fundamental Algorithms for Scientific Computing in Python". In: *Nature Methods* 17, pp. 261–272. DOI: 10.1038/s41592-019-0686-2.

Taylor, M. B. (2005). "TOPCAT & STIL: Starlink Table/VOTable Processing Software". In: *Astronomical Data Analysis Software and Systems XIV*. Ed. by P. Shopbell, M. Britton, and R. Ebert. Vol. 347. Astronomical Society of the Pacific Conference Series, p. 29.

Kennicutt Robert C., Jr. (1998). "Star Formation in Galaxies Along the Hubble Sequence". In: *ARAA* 36, pp. 189–232. DOI: 10.1146/annurev.astro.36.1.189. arXiv: astro-ph/9807187 [astro-ph].

Bell, Eric F. et al. (2005). "Toward an Understanding of the Rapid Decline of the Cosmic Star Formation Rate". In: *APJ* 625.1, pp. 23–36. DOI: 10.1086/429552. arXiv: astro-ph/0502246 [astro-ph].

Joye, W. A. and E. Mandel (2003). "New Features of SAOImage DS9". In: *Astronomical Data Analysis Software and Systems XII*. Ed. by H. E. Payne, R. I. Jedrzejewski, and R. N. Hook. Vol. 295. Astronomical Society of the Pacific Conference Series, p. 489.

Casey, Caitlin M., Desika Narayanan, and Asantha Cooray (2014). "Dusty star-forming galaxies at high redshift". In: *Physics Reports* 541.2, pp. 45–161. ISSN: 0370-1573. DOI: 10.1016/j.physrep.2014.02.009. URL: http://dx.doi.org/10.1016/j.physrep.2014.02.009.

Donley, J. L. et al. (2012). "Identifying Luminous Active Galactic Nuclei in Deep Surveys: Revised IRAC Selection Criteria". In: *APJ* 748.2, 142, p. 142. DOI: 10.1088/0004-637X/748/2/142. arXiv: 1201.3899 [astro-ph.CO].

Madau, Piero (1995). "Radiative Transfer in a Clumpy Universe: The Colors of High-Redshift Galaxies". In: *APJ* 441, p. 18. DOI: 10.1086/175332.

Chabrier, Gilles (2003). "Galactic Stellar and Substellar Initial Mass Function". In: *Publications of the Astronomical Society of the Pacific* 115.809, pp. 763–795. ISSN: 1538-3873. DOI: 10.1086/376392. URL: http://dx.doi.org/10.1086/376392.

Salpeter, Edwin E. (1955). "The Luminosity Function and Stellar Evolution." In: *APJ* 121, p. 161. DOI: 10.1086/145971.

Scoville, N. et al. (2016). "ISM MASSES AND THE STAR FORMATION LAW ATZ= 1 TO 6: ALMA OBSERVATIONS OF DUST CONTINUUM IN 145 GALAXIES IN THE COSMOS SURVEY FIELD". In: *The Astrophysical Journal* 820.2, p. 83. ISSN: 1538-4357. DOI: 10.3847/0004-637x/820/2/83. URL: http://dx.doi.org/10.3847/0004-637X/820/2/83.

Magdis, Georgios (2012). *Georgios E. Magdis, Software*. http://www.georgiosmagdis.com/software/. Accessed: 2021-05-10.

Lindroos, L. et al. (2014). "Stacking of large interferometric data sets in the image- and uv-domain – a comparative study". In: *Monthly Notices of the Royal Astronomical Society* 446.4, pp. 3502–3515. ISSN: 0035-8711. DOI: 10.1093/mnras/stu2344. URL: http://dx.doi.org/10.1093/mnras/stu2344.

Appendix A

ZFOURGE catalog additional properties

In this appendix additional analysis carried out on the ZFOURGE survey will be shown.

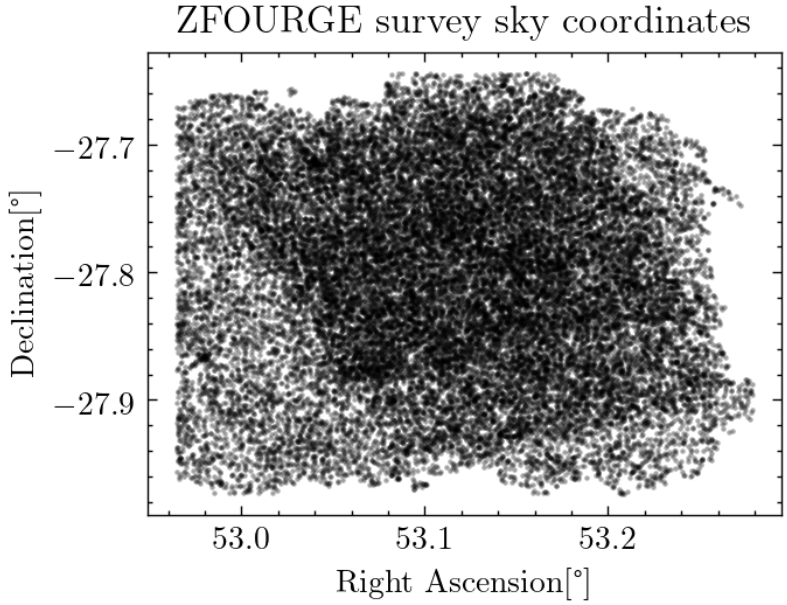

Figure A.1: RA & DEC coordinates of the sources in the ZFOURGE catalog

Here it is shown the differences in the ΔMS according to the different chosen star formation rates: SFR from the SED fitted models, SFR_{UVIR} obtained from L_{IR} and L_{UV} or a hybrid SFR which is a combination of both depending on whether a galaxy has robust detections in the 24,100 and 160μm IR filters.

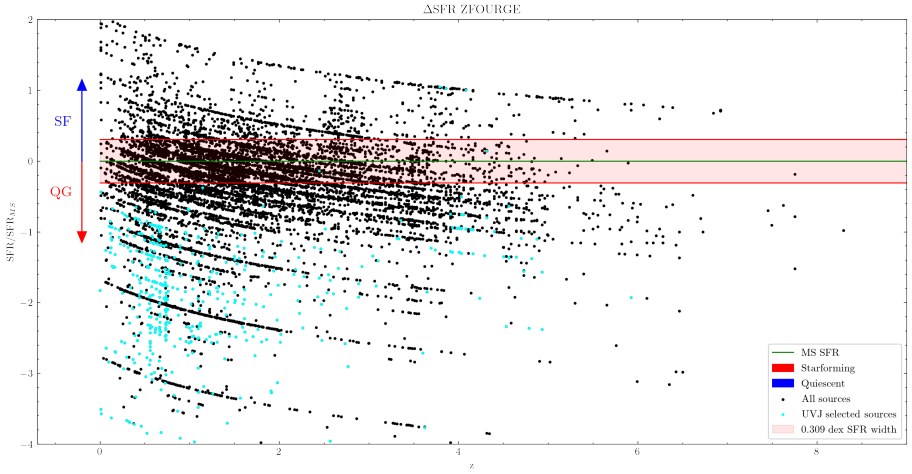

(a) SFR from SED fitted models

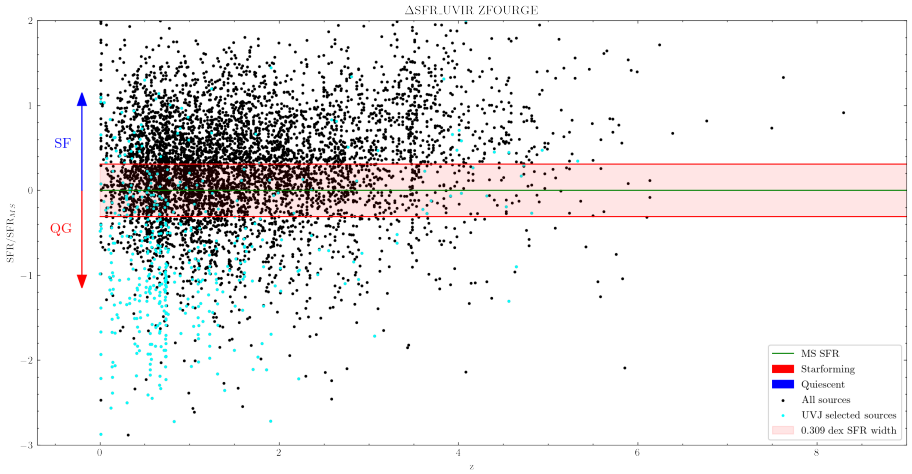

(b) SFR_{UVIR}

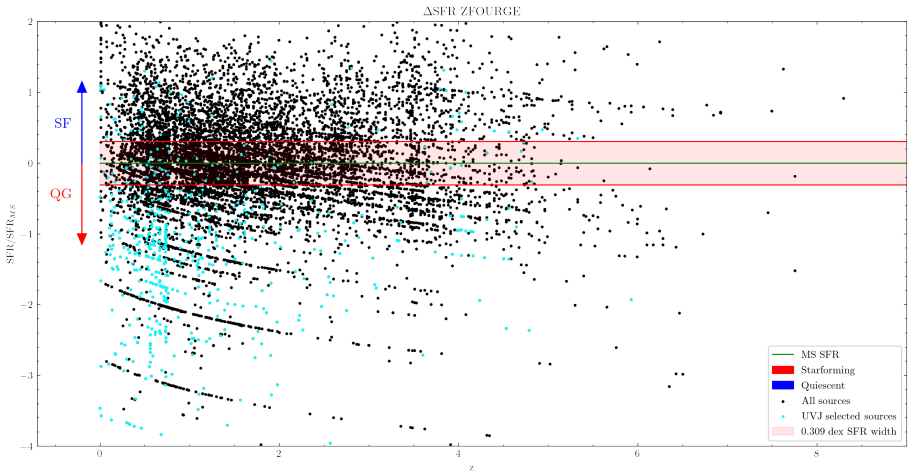

(c) Hybrid SFR

Figure A.2: Plots showing the scatter of ΔMS vs redshift of the ZFOURGE catalog. The green line represents the SFR of the main sequence calculated with equation 1.5. The red upper and lower boundaries represent the 0.3 dex dispersion of the main sequence below which sources can star to be considered quiescent or ongoing quenching. In cyan we can see the galaxies identified as quiescent with the UVJ selection criterion.

Another method for comparing the selected quiescent sources is to portray them in the M_{star} plane. Firstly, a plot with simulated data is built, to use as a reference. In order to build the synthetic data, for each defined redshift range, first a group of 10000 galaxies is built whose $\log_{10}(M_{star})$ are assigned from a random distribution ranging from 10^8 to $10^{12} M_{\odot}$. Then another 10000 sources are added to the data , whose $\log_{10}(M_{star})$ are assigned from a normal distribution with $\mu = 9.5$ and $\sigma = 0.5$. We then use [Schreiber et al., 2015] main sequence SFR calibration formula to define the SFR-M_{star} main sequence locus. The dispersion of the main sequence is obtained by adding synthetic noise to the data which is drawn from a normal distribution with zero mean and $\sigma = 0.3$ which is the current measured dispersion for the main sequence [Schreiber et al., 2015]. A population of starburst galaxies is simulated following the same procedure assign M_{star} but then the SFR is calculated as 4 times the SFR_{MS} plus a random uncertainty in order to simulate a scatter in the starburst population, which we restrict to a 1% of the total mains sequence population. Finally quiescent galaxies are simulated, firstly by estimating the quantity as a fraction of the main sequence population, which varies depending on the plotted redshift range. Then the SFR of the QG population is calculated by multiplying the SFR_{MS} by a random factor ranging from 1/1000 to 1/10. The results can be seen below in figure A.3. In it we observe the position in which quiescent galaxies are relative to the main sequence locus, so then a comparison with the actual data can be done.

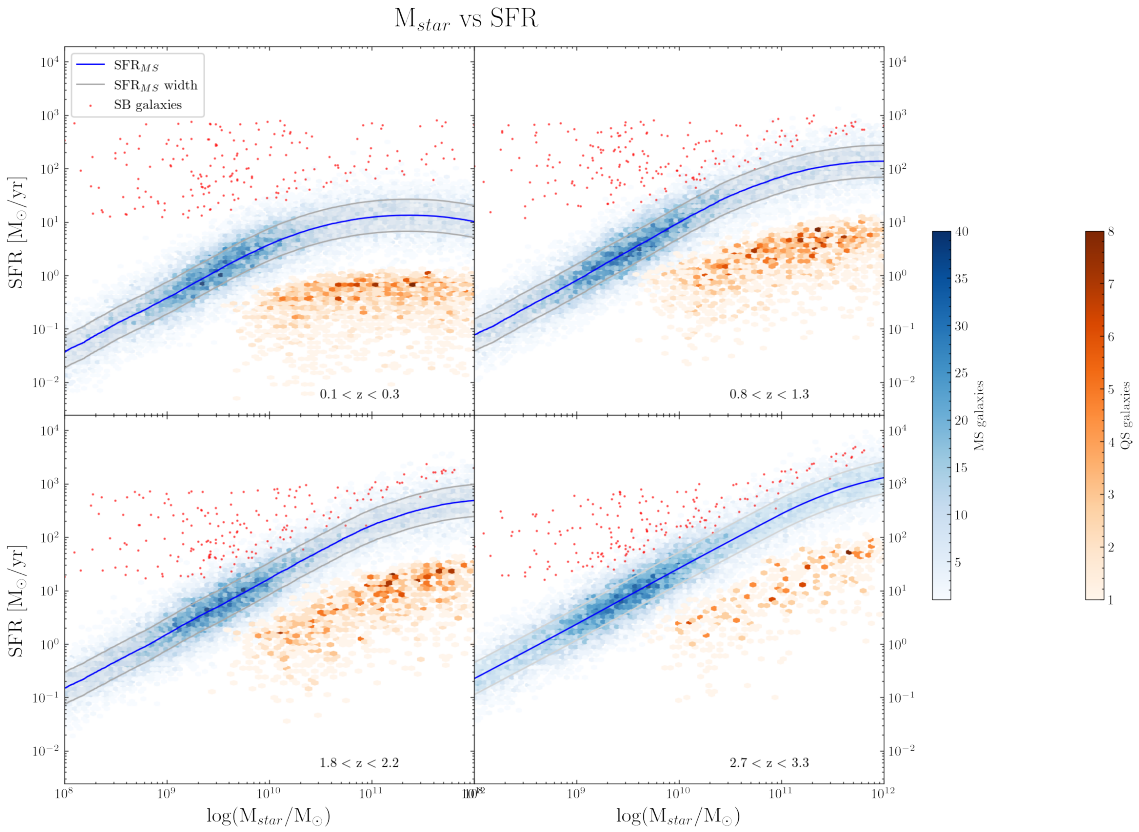

Figure A.3: M_{star} vs SFR diagram of simulated data. The blue curve and grey shaded area represent the Schreiber et al., 2015 predicted MS locus with a 0.3 dex dispersion. Then we the simulated data scattered in hexagonal bins color coded according to the number of galaxies within the bin. In blue the main sequence galaxies and in orange the quiescent galaxies. Finally the individual SB galaxies are plotted in red.

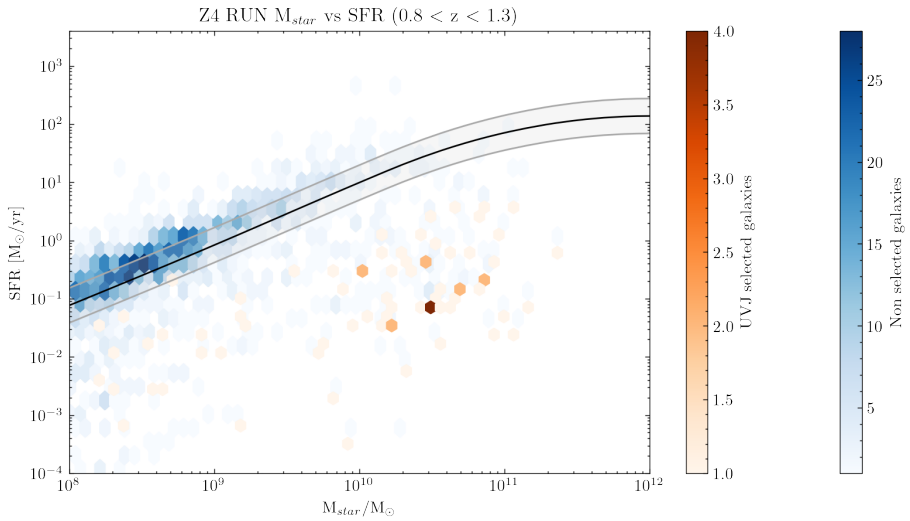

(a) 0.8 < z < 1.3

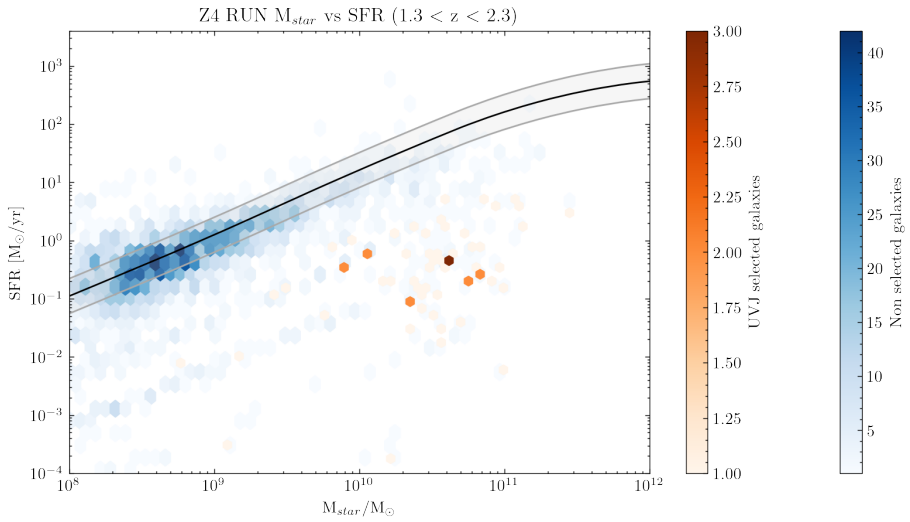

(b) 1.3 < z < 2.3

Figure A.4: M_{star} vs SFR diagram of the ZFOURGE data. The blue curve and grey shaded area represent the Schreiber et al., 2015 predicted MS locus with a 0.3 dex dispersion. The orange sources represent the UVJ selected sources. The rest of the galaxies are plotted in blue.

It is observed that the scarce amount of QG is located below the main sequence, similarly to what we see in figure A.3. There is, though a small offset between the bulk of the rest of galaxies and the defined main sequence area. However the issue that arises in these plots is the great amount of low M_{star} galaxies that have very low predicted star formation rates. Why do they have such low SFR and are not considered quiescent by the UVJ color-color criterion? This uncertainty in the SFR is then acknowledged for the performed analysis.

Appendix B

EAZY

Here we can see the settings that were utilized for the EAZY run.

In [ ]:

```
params = {}

###### Filters
params['Filter_RES'] = 'calibrations/FILTER.RES.latest'
params['FILTER_FORMAT'] = 1
params['SMOOTH_FILTERS'] = 0
params['SMOOTH_SIGMA'] = 100

###### Templates
# params['TEMPLATES_FILE'] = 'templates/spectra.param'
params['TEMPLATES_FILE'] = 'templates/fsps_full/tweak_fsps_QSF_12_v3.param'
params['TEMPLATES_FILE'] = 'templates/spline_templates_v2/tweak_spline.param'
params['TEMPLATE_COMBOS'] = 99
params['NMF_TOLERANCE'] = 1.00e-5
params['WAVELENGTH_FILE'] = 'templates/lambda_v1.1.def.txt'
params['TEMP_ERR_FILE'] = 'calibrations/TEMPLATE_ERROR.v2.0.zfourge'
params['TEMP_ERR_A2'] = 1
params['SYS_ERR'] = 0
params['APPLY_IGM'] = 1
params['SCALE_2175_BUMP'] = 0.000
params['N_MIN_COLORS'] = 3
params['MW_EBV'] = 0.00852

###### Cosmology
params['H0'] = 70.000
params['OMEGA_M'] = 0.300
params['OMEGA_L'] = 0.700

###### Input files
params['CATALOG_FILE'] = 'cdfs.v1.6.11.cat'
params['MAIN_OUTPUT_FILE'] = 'zfourge.cdfs'
params['PRINT_ERRORS']= 1
params['CHI2_SCALE']=1.000

###### Redshift / Mag prior
params['APPLY_PRIOR'] = 1
params['PRIOR_FILE'] = 'templates/prior_K_TAO.dat'
params['PRIOR_FILTER'] = 33 # K filter
params['PRIOR_ABZP'] = 25

###### Redshift grid
params['FIX_ZSPEC']=False
params['Z_MIN'] = 0.01
params['Z_MAX'] = 10.
params['Z_STEP'] = 0.005
params['Z_STEP_TYPE'] = 1


###### Zeropoint offsets
zpfile = f'zphot.zeropoint.{field}'
if not os.path.exists(zpfile):
    zpfile = None
print(f'\nzeropoint file: {zpfile}\n')



###### Translate file
translate_file = 'eazy/cdfs.v1.6.9.translate'

if 1:
    self = eazy.photoz.PhotoZ(param_file=None, translate_file=translate_file, zeropoint_file=zpfile, pa
rams=params, load_prior=True, load_products=False)
else:
    self = eazy.photoz.PhotoZ(param_file=None, translate_file=translate_file,
                              zeropoint_file=None, params=params, load_prior=True, load_products=True)
    zout = utils.read_catalog('{}.eazypy.zout.fits'.format(field))
```

Figure B.1: Settings used for the EAZY run

The other set of specifications that are not defined in the Jupyter cell above are set to the default state.

In a similar fashion to appendix A, the EAZY catalog data is plotted on the M_{star}-SFR plane and see its relative position to the main sequence predicted SFR and observe whether the main bulk of galaxies remains within the locus of the main sequence. Also the position of UVJ selected QG in the plot will help assessing the quality of the quiescent selection and whether it is contaminated by star forming galaxies.

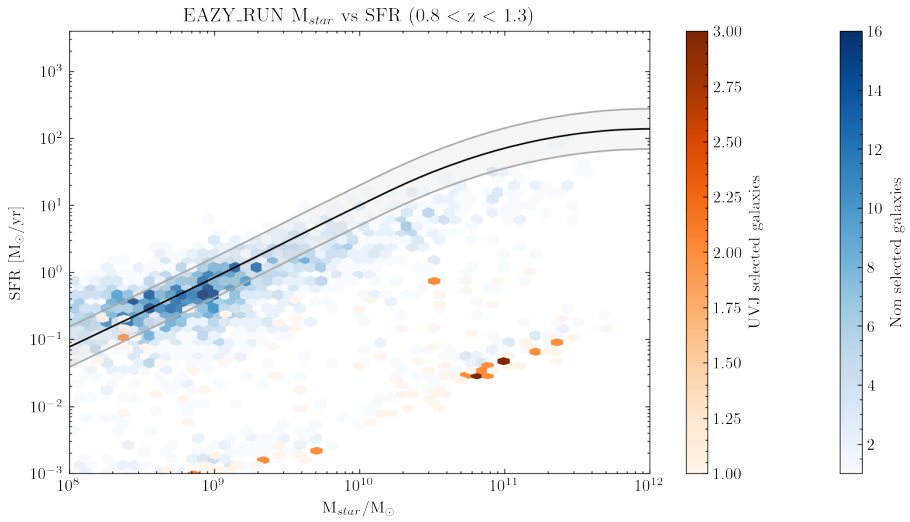

(a) 0.8 < z < 1.3

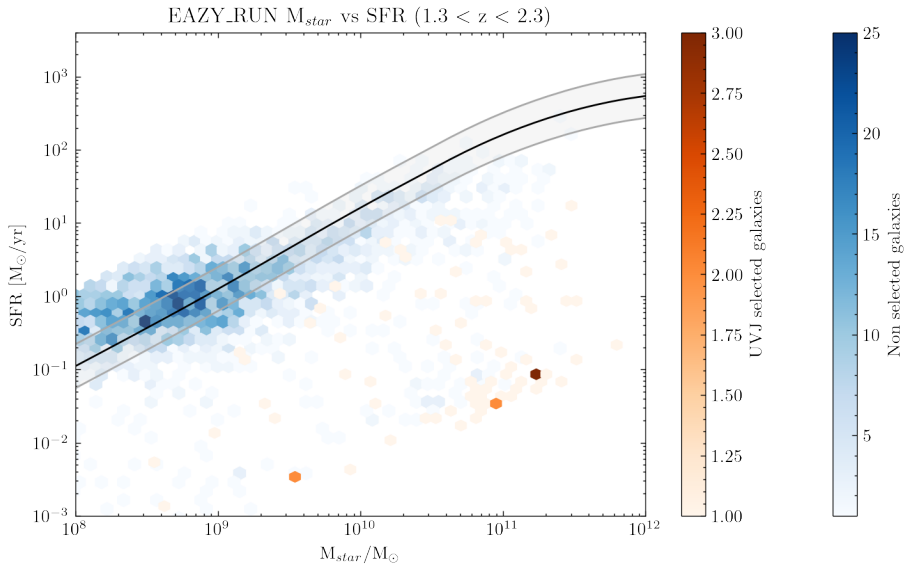

(b) 1.3 < z < 2.3

Figure B.2: M_{star} vs SFR diagram of the EAZY data. The blue curve and grey shaded area represent the Schreiber et al., 2015 predicted MS locus with a 0.3 dex dispersion. The orange sources represent the UVJ selected sources. The rest of the galaxies are plotted in blue.

The quiescent selection of galaxies seem to be well bellow the main sequence. However, the offset seen in figure 3.15b seems to be present in this plots too. It can be observed how

the defined main sequence locus fails to capture or encompass the bulk of non quiescent galaxies, with a considerable amount of them found above the main sequence region. The reason for this is still unclear, it might be due to the M_{star} offset found in figure 3.13, however, without a deeper analysis of EAZY's procedures, the question remains unclear.

DTU Space
Technical University of Denmark

Elektrovej, Building 328
2800 Kgs. Lyngby
Tlf. 4525 1700

https://www.space.dtu.dk/english